A New Class of Photoresponsive Surfactants

by

Tiangang Shang

Bachelor of Engineering in Chemical Engineering (1991)
Tianjin University, Tianjin, P. R. China

Master of Engineering in Chemical Engineering (1994)
Tsinghua University, Beijing, P. R. China

Submitted to the Department of Chemical Engineering in partial fulfillment of the requirements for the degree of

Doctor of Philosophy

at the
Massachusetts Institute of Technology
December 2004
[February 2005]

Signature of Author.....
Department of Chemical Engineering
January 6, 2005

Certified by.....
T. Alan Hatton
Ralph Landau Professor of Chemical Engineering Practice
Thesis Supervisor

Certified by.....
Kenneth A. Smith
Edwin R. Gilliland Professor of Chemical Engineering
Thesis Supervisor

Accepted by.....
Daniel Blankschtein
Professor of Chemical Engineering
Chairman, Committee for Graduate Students

A New Class of Photoresponsive Surfactants

by

Tiangang Shang

Submitted to the Department of Chemical Engineering on October 18, 2004,
in partial fulfillment of the requirements for the degree of
Doctor of Philosophy in Chemical Engineering

Abstract

In this thesis, a new class of nonionic, photoresponsive surfactants consisting of a polar di(ethylene oxide) head group attached to an alkyl spacer of between two and eight methylene groups, coupled through an ether linkage to an azobenzene moiety, were synthesized and developed. Structural changes associated with the interconversion of the azobenzene group between its cis and trans forms as mediated by the wavelength of an irradiating light source, cause changes in the surface tension, critical micellization concentrations (CMC), and self-assembly behavior. Differences in saturated surface tensions (at concentrations above their CMCs) were as high as 14.4 mN/m under radiation of different wavelengths. This large and reversible change in saturated surface tensions in response of different illumination conditions made these new surfactants have potential applications in the pumping and control of flow in microfluidic devices, and in the microchemical analysis of complex fluids, flow cytometry, rapid DNA screening.

The interfacial properties of these new surfactants have been investigated through surface tension measurements and neutron reflection experiments under both UV and visible light. From surface tension measurements, the surface excess and therefore average molecular areas can be obtained through Gibbs equation; while through measuring neutron reflectivities at different Q range, the interfacial conformations of these surfactants can be determined within the resolution of several angstroms. It was found that the interfacial conformations of these surfactants are very sensitive to the length of the spacer and conformation of azobenzene group. Depending on the different lengths of spacer and conformations of azobenzene groups (trans or cis), surfactants can take either regular conformation or loop conformation, in which the spacer between the polar head and the intermediate polar group forms a loop anchored at both ends in the interfacial plane. This explained the observed large change in saturated surface tensions under different wavelengths radiation.

The self-assembly behavior of these surfactants in bulk phase has been studied experimentally through the static and dynamic light scattering, small angle neutron scattering, and cryo-TEM techniques under both UV and visible light. At high enough concentrations, trans surfactants form the vesicles; while cis surfactants self-assemble into bicontinuous phase. This transition indicated the significance of the sign of Gaussian rigidity in surfactant self-assembly. Through varying the azobenzene conformation by

radiation of different wavelengths, the sign of the Gaussian rigidity can be controlled, and therefore, there self-assembly behavior can be controlled by light too.

Thesis Supervisor: T. Alan Hatton
Title: Ralph Landau Professor of Chemical Engineering Practice

Thesis Supervisor: Kenneth A. Smith
Title: Edwin R. Gilliland Professor of Chemical Engineering

Acknowledgements

I would like to express my sincerely thanks to my thesis advisors Professor Alan Hatton and Professor Kenneth A. Smith for their guidance on all aspects during my study at MIT. Alan is always surprised me with his insightful suggestions and incentive new ideas on my thesis project, and with his wonderful skill in scientific writing. Ken is impressed me with his deep insight on various scientific problems, his sheer skill in solving complex problem in a simply way, and his strict attitude towards research. I also like to thank them for their consideration and generosity. Finally, I am indebted to their financial support during my thesis so that I can focus my total mind on the research. I like to thank my thesis committee members Professor Patrick Doyle and Professor Paul Laibinis, for their valuable discussions and suggestions on my project, and easy access for discussion. I also like to thank Professor Daniel Blankschtein for the constructive discussion and his interest on my project.

I like to thank Elizabeth Wang, my UROP student, who actively involved in the experiments of this research during last two years. Her diligence and enthusiasm contribute so much to this work. In addition, the other people who assisted me during this research are also appreciated, including Steve Yang of MIT Biology who teaching me QFDE sample preparation; Nicki Watson of the Whitehead Institute for helping me in TEM samples examination; Paul Johnson of the University of Rhode island for helping me in cryo-TEM sample preparation and examination; Steve Kline, Sushil Satija, and Young-Soo Seo of NIST for SANS and neutron reflection. I like to thank previous and current members in Hatton group for providing a friendly and supporting research environment. In particular, I like to thank Isabella for teaching me vesicle preparation, Brad for exposing his DLS data to me, Huan for great assistance in neutron refection experiments, Shuwang for sharing his knowledge and experience of neutron reflection and surfactant adsorption with me, Harpreet for help in examining SEM sample, and Lino, Smeet, Sanjoy, Lev, Marco, Andre, Ed for active discussion on research. I must also thank Carol Philips, Arline Benford, Beth Tuths, and Linda Mousseau for their consistent help during my stay at MIT.

I like to thank my parents Chen Shang and Xueqin Zhou for their bringing me up, their awaking my interest on Science and Engineering, and for their incredible financial and mental support during my growing. Finally, I like thank my wife Xuemei Zhang for her incredible support, for her encouragement and accompanying during my difficult time, and for her understanding.

Table of Contents

List of Figures

List of Tables

Chapter 1

Control of Self-assembly and Interfacial Properties in Surfactant Solutions

The amphiphilic molecules, or surfactants, have many practical applications in detergent, water- proofing fibre fabrication, painting, and cosmetic, etc. [1]. More recently, they have been shown to have prospect applications in Hi technologies, such as in micro-analysis of complex fluids, rapid DNA screening, manipulation flow in microfluidic network, and cytometry [2]. These applications strongly depend on the availability of the flexible and efficient method to control the self-assembly and interfacial properties in aqueous solutions of surfactants. Amongst all existing control methods, photo-control is probably the most prospective one because of its high spatial and temporal resolutions. The photo-control of self-assembly and interfacial properties can be achieved by using photoresponsive surfactants. Photoresponsive surfactants contain the photoactive functional unit (usually azobenzene)[3], which can switch back and forth between the distinct molecular conformations in response to radiations of different wavelengths. As the result of the change in the molecular conformation, the interfacial and self-assembly properties in photoresponsive surfactant systems, thereafter, are expected to change. From the view point of practical applications, the photoresponosive surfactants, which exhibit the significant changes in surface tension and self-assembly behavior under different illumination conditions, are highly desirable.

This thesis presents a detailed investigation of a new class of photoresponsive surfactants that was developed for the purpose of the active control of surface tension and self-assembling behavior. In this chapter, the basic background about surfactants together with their surface tension and self-assembling properties are introduced.

1.1 Bulk and Interfacial Properties in Surfactant Solutions

The term "surfactant" describes a class of special molecules in which two or more moieties with distinct properties are covalently joined together. Usually, surfactant molecules consist of tail and head parts. The tail group is hydrophobic, which is difficult to dissolve in water but easily dissolved in oil (or any nonpolar organic solvent); the head group is hydrophilic and dissolves in water more easily than in oil[1]. This heterogeneous molecular structure gives the surfactant peculiar properties. In aqueous solution, for instance, surfactants can significantly lower the surface tension by adsorption at air-water interfaces; and similarly, lower the interfacial tension at oil-water interfaces. Such effects can be used, for instance, to control foam and emulsion stability, spreading of liquids on surfaces, and surface driven flows[Myers, 1999 #45]. At high enough concentrations, surfactants can self-assemble into a variety of aggregates, and these aggregates can further organize into liquid crystal phases. Although it is usually not possible to calculate these properties solely from molecular parameters, most surfactant properties can be well predicted by simple qualitative arguments and semi-empirical equations. It was found more than 30 years ago that the hydrophobic effect is the dominant factor responsible for the self-assembly and adsorption in surfactant systems[4]. Briefly, the hydrophobic effect merely states that the hydrophobic part of the molecule tends to escape from contact with water, which is entropically unfavorable, by organizing themselves into microheterogeneous phases, such as micelles and monolayers or double layers at the interface. This process is essentially driven by entropy, in which the entropy of the system increases as the result of the disruption of the hydrogen bond network surrounding each hydrophobic moiety when it is removed from the bulk aqueous phase[4].

1.1.1 Self-assembly Behavior of Surfactants

It has long been known that surfactant solutions often exhibit strange behavior above a certain concentration. At this concentration, the osmotic pressure, electrical conductivity and surface tension begin to show anomalous concentration dependencies, which deviate significantly from the predictions of colligative laws, although those concentrations are still low enough for the colligative laws to be a good approximation of

the behavior of molecular solution. The violation of the colligative laws can be reasonably resolved if small aggregates (micelles) are assumed to appear in the solution above this concentration[5]. As it was difficult to test experimentally, the idea of the micelle was not accepted until Debye's decisive light scattering experiment. In Debye's experiment, not only was the formation of micelles clearly demonstrated, but also the "molecular weight" of micelles was measured [6,7]. Moreover, the concentration at which micelles begin to appear was coincident with the one where deviation from the colligative law occurred. It was concluded that the appearance of micelles is responsible for the anomalous solution behavior in surfactant systems.

The equilibrium conditions necessary for the existence of micelles, i.e. surfactant self-assembly, can be formulated by simple thermodynamic considerations[8]. Consider a surfactant solution, in which there are N_s surfactant molecules and N_w water molecules. There are also aggregates of different sizes z (z is the number of surfactant molecules inside a given aggregate) in the solution, whose number is indicated by N_z. At equilibrium, the Gibbs free energy of the system, G_t, must be a minimum:

$$G_\tau = N_w \mu_w + N_1 \mu_1 + \sum_j N_j \mu_j \qquad (1\text{-}1)$$

where μ_w is the chemical potential of water; μ_1 is the chemical potential of the monomer; μ_j is the chemical potential of a micelle of size j;. N_1 is the number of monomers, and N_j is the number of micelles of size j. Usually, micelles appear at extremely low concentrations, so the solution is essentially ideal. The chemical potential of each species is therefore

$$\mu_j = \mu_j^0 + k_B T \ln X_j \qquad (1\text{-}2)$$

where μ_j^0 is the chemical potential at the standard state, and X_j is the mole fraction of species j.

The relation between different species can be found by minimizing the free energy G_t under the restriction of mass conservation:

$$N_s = N_1 + \sum_{j=2}^{s} jN_j \tag{1-3}$$

The object function becomes

$$G_T = N_w \mu_w + N_1 \mu_1 + \sum_{j=2}^{s} N_j \mu_j + \lambda(N_s - N_1 - \sum_{j=2}^{s} jN_j)$$

where λ is the Lagrange multiplier. By taking derivative of object function with respect to $N_1, N_2, \ldots\ldots, N_s$ and λ, it is found that at equilibrium,

$$\mu_1 = \frac{\mu_2}{2} = \frac{\mu_3}{3} = \ldots\ldots = \frac{\mu_s}{s} \tag{1-4}$$

which implies each micelle can freely exchange monomer with the surrounding solution. The same relation can be obtained too, if we assume chemical equilibrium between the micelle and its constituent monomers, $N_s \Leftrightarrow sN_1$, and thus that the mass action law is obeyed. From (1-2) and (1-4), the mole fraction of the s-micelle is equal to

$$X_s = X_1^s \exp(-\frac{\mu_s^0 - s\mu_1^0}{k_B T}) \tag{1-5}$$

Because X_1 is usually very small, X_s is usually negligible unless μ^0_s - $s\mu^0_1$ is negative. Thus, $\mu_s^0 - s\mu_1^0 < 0$ is a sufficient and necessary condition for micelle formation. This states that, at standard state, there is a free energy gain when s monomers assemble into 0an s-aggregate. All detailed molecular information of self-assembly is included in μ^0_s. However, from thermodynamics solely, we can not get any microscopic information about μ^0_s, and statistical mechanics is needed to correlate μ^0_s with molecular parameters. Indeed, it can be proved that μ^0_s is the partition function of an s-micelle. Because of the complexity of the system, the derivation of the partition function of an s-micelle from statistical mechanics is a rather formidable task. However, based on insights on the self-assembly process, a reasonably good estimate can be obtained as to how μ^0_s changes with s. For example, for a spherical micelle, it is believed that μ^0_s can be well described by,

$$\mu_s^0 = s\tilde{\mu}_s^0 = -s\mu,\ s = m$$

$$\mu^0{}_s = 0,\ all\ other\ sizes$$

The mole fraction of an *s-mer* is, therefore, found to be $X_m = X_1^m \exp(-\frac{\mu_m^0 - m\mu_1^0}{k_B T}) = X_1^m \exp(-m\frac{\tilde{\mu}_m^0 - \mu_1^0}{k_B T})$ where $\tilde{\mu}_m^0 - \mu_1^0$ is termed as transfer free energy g_{mic} ($\tilde{\mu}_m^0 = \frac{\mu_m^0}{m}$)[9].

For simplicity, assume the aggregation number m is far larger than 1 (The conclusion applies to other m values too). At equilibrium,

$$\frac{\mu_m^0}{m} + \frac{RT}{m}\ln X_m = \mu_1^0 + k_B T \ln X_1 \qquad (1\text{-}6)$$

The second term in the LHS can be dropped as a consequence of large m. The monomer concentration is therefore $X_1 = e^{\frac{(\tilde{\mu}_m^0 - \mu_1^0)}{k_B T}}$ (m is the average aggregation number of micelles) , which is actually the critical micelle concentration (CMC). It can be proved as follows. Let X denote the total mole fraction of surfactant in the solution, which is equal to $X_1 + mX_m$. It is straightforward to calculate

$$\frac{\partial X_1}{\partial X} = \frac{1}{1 + m^2 X_1^{m-1} e^{-m\frac{g_{mic}}{K_B T}}} \qquad (1\text{-}7)$$

When X_1 is much smaller than $e^{\frac{(\tilde{\mu}_m^0 - \mu_1^0)}{k_B T}}$, this derivative is close to 1, which implies all added surfactants are monomers in the solution. However, when X_1 approaches $e^{\frac{(\tilde{\mu}_m^0 - \mu_1^0)}{k_B T}}$, the derivative is almost zero, which indicates almost all added surfactants are incorporated into aggregates. Therefore, when the total concentration X approaches $e^{\frac{(\tilde{\mu}_m^0 - \mu_1^0)}{k_B T}}$, there is a sharp increase in the number of aggregates. Because m is usually

large, the width of the transition region is fairly narrow. It seems that micelles appear suddenly in what is akin to a kind of "phase transition".

The driving force in self-assembly is the hydrophobic effect. Its magnitude can be inferred from the experimental value of the transfer free energy g_{mic} that is of the order of tens of k_BT. It is much weaker than the covalent bond, whose bond energy is about several hundreds k_BT. This relatively small energy scale causes surfactant self-assembly be very sensitive to variations in external conditions, a slight variation in which may lead drastic changes in self-assembly behavior. For example, in a microemulsion system close to a phase boundary, a small amount of additional cosurfactant can bring about a significant structural transition in the aggregates.

The structure and shape of surfactant aggregates are sensitive to the molecular architecture, which is believed to exert important steric effects on the packing of surfactants into aggregates. It has been observed experimentally that surfactants can self-assemble into aggregates with various shapes, such spheres, cylinders, disks, etc[5]. The shape of surfactant aggregates can be predicted well from its molecular parameters, in particular, by its packing parameter[8]:

$$N_s = \frac{V_s}{l_c a_0} \tag{1-8}$$

where V_s is the volume of the surfactant tail; l_c is the critical length of the surfactant tail, whose value is close to the fully extended molecular length of the tail; and a_0 is the optimal surface area per molecule. If $N_s < 1/3$, spherical aggregates are preferred; while for $1/3 < N_s < 1/2$, cylindrical aggregates will be energetically stable; and if $1/2 < N_s < 1$, surfactants will self-assemble into disk-like aggregates.

At still higher concentrations, micelles can organize into liquid crystals, i.e., lyophilic liquid crystals[5]. The basic structural blocks of lyophilic liquid crystals are surfactant aggregates. It can be viewed as self-assembly at high level, in which the local ordered micelles arrange themselves in space with some long range orientational or positional order. The new long range order appears in the system in addition to the local

order in micelles. Under the certain condition, some surfactants can form bicontinuous phase, in which one single, continuous surfactant bilayer extends through the whole system and arrange its local curvatures in such a way that the area of surfactant-water interface is minimum. Unlike the ordered lyophilic liquid crystal phases, most bicontinuous phases possess the random structural features.

1.1.2 Interfacial Properties of Surfactant Solution

Driven by the hydrophobic effect, surfactants tend to be enriched at the air-liquid interface where they can decrease the free energy of the whole system through adopting special conformations. Usually, head groups are immersed into the water sub-phase, while tails are oriented away from the water interface.

Since surfactant molecules have two basic moieties, the hydrophilic head and hydrophobic tail, they have the ability to balance between two different bulk phases and lower the free energy of the whole system. Specifically, surfactants can reside on an interface with each structural element contacting a "similar" bulk phase. The "tension" originating from contact of two different bulk phases now applies to surfactants, and balance out by the covalent chemical bonds in surfactants. The direct evidence of free energy decreases in the system is the lowering of the surface tension, which is defined as the free energy per unit interfacial area. The surface tension of water is about 72 mN/m. If nonionic surfactant is added to the system, the surface tension can be lowered to 30 mN/m.

The surface tension can be defined in a more strict sense through thermodynamics[10]. Consider a one-component system with two phases under constant temperature T, volume V and particle number N. Because of the interface, the Helmholtz free energy of whole system F_t is different from the sum of F_A and F_B, which are the Helmholtz free energies of bulk phases A and B, respectively. The difference is defined as surface or interfacial free energy F_s, which is a specific example of a surface excess function. Surface excess functions are thermodynamic quantities characterizing the interface, whose thickness is idealized to zero. For the Helmholtz free energy, the surface excess function is defined as,

$$F_s = \frac{F_t - (F_A + F_B)}{A_0} \tag{1-9}$$

in which bulk phases A and B are separated and defined by the sharp dividing surface (Figure 1-1); A_0 is the surface area. It is straightforward to write a differential form of the surface excess Helmholtz free energy for unit surface area,

$$dF_s = -S_s dT + \mu d\Gamma \tag{1-10}$$

where Γ is the surface excess concentration, and S_s is the surface excess entropy. In a multi-component system, the surface excess Helmholtz free energy density is

$$dF_s = -S_s dT + \sum_i \mu_i d\Gamma_i \tag{1-11}$$

where Γ_i is the surface excess concentration of component i.

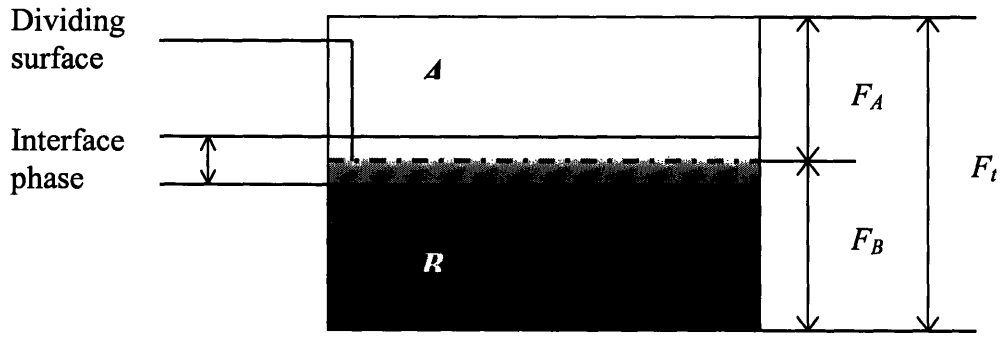

Figure 1-1 Definition of surface excess free energy. F_t is the total free energy of the system as a whole. F_A and F_B are the free energies of phase A and B, respectively. Phase A and B are defined by the dividing surface, which is an idealization of real interface phase.

Usually, F_s is called the surface tension of the interface, and represented by the symbol γ. In a more general method, surface tension can also be defined as the surface

excess grand potential per unit area[10]. However, after correlating surface tension to bulk properties through the Gibbs-Duhem equation, the two definitions give the same result, so which definition is adopted is a matter of personal preference and context in which the phenomenon of surface adsorption is discussed.

When applying the Gibbs – Duhem equation to the interface, we obtain

$$d\gamma + S_s dT + \sum_i \Gamma_i d\mu_i = 0 \tag{1-12}$$

which leads to well-known Gibbs equation,

$$\Gamma_i = -(\frac{\partial \gamma}{\partial \mu_i})_{T,P} \cong -\frac{c_i}{RT}(\frac{\partial \gamma}{\partial c_i})_{T,P} \tag{1-13}$$

in which c_i is the concentration of the *ith* component in the bulk phase. The second term on the RHS will hold only at low concentrations where the solution is ideal. The Gibbs equation is one of the most important thermodynamic relations governing the interface, as it clearly reveals the inherent connection between interfacial and bulk properties. This equation provides a way to measure surface excess concentration, which is just the slope of the surface tension versus log concentration curve. This is the usual way to obtain surface excess concentrations experimentally.

1.2 Control of Interfacial and Bulk Properties in Surfactant Solutions

The applications of surfactants are usually based on their two basic features: the formation of microheterogeneous phases through self-assembly; and their ability to change surface tensions by adsorption at surfaces. Both processes are driven by the hydrophobic effect. As mentioned earlier, the hydrophobic effect is fairly weak and of the order of tens of k_BT [4]. As a consequence, self-assembly and surface tension are very sensitive to the external conditions. It is this sensitivity that provides the possibility of active control of bulk and interfacial properties in surfactant solutions. However, although driving forces in these two processes are essentially the same, each process

possesses its own characteristics because of the subtle differences in molecular packing and packing environment in each case.

1.2.1 Control of Interfacial Properties in Surfactant Solutions

One of the unique characteristics of surfactants is their capability to decrease surface tension. With the advent of nanotechnology, human beings began to manipulate objects with smaller and smaller size, and the effect of the surface becomes more and more dominant, as the ratio of surface area to volume increases significantly with the length scale decreasing. As the major physical property of a surface, surface tension, and therefore its control, have been shown to be important in emerging high technologies, and can be exploited in the pumping and control of flow in microfluidic devices, and in the microchemical analysis of complex fluids, flow cytometry, rapid DNA screening, etc[2]. Advances in these new technologies will depend strongly on the availability of flexible methods for adjusting and controlling surface tension dynamically.

Photo-control using photosensitive surfactants is a potentially attractive route to accomplishing many of the tasks required in these processes. One class of such surfactants is based on the photo-responsive azobenzene group[11,12], which changes its conformation reversibly when illumination is switched between UV and visible light (Figure 1-2). Under UV light irradiation, azobenzene adopts the cis conformation, whereas, on illumination with visible light, its conformation reverts back to the trans form[3]. When these azobenzene groups are incorporated within the tail group of a surfactant, this reversible photo-isomerization often induces changes in interfacial properties, such as surface tension, and in related bulk solution properties, such as micelle formation and structure. In some applications, however, these systems will be useful only if the changes in surface tension with changing illumination conditions are large, and if the surfactants are used at concentrations well above their critical micelle concentrations (CMCs) so that loss of surfactant by adsorption to interfaces and surfaces does not appreciably affect the bulk properties or surface tensions.

Many azobenzene-bearing surfactants have been reported in the literature[11,12 13-43]. Most of them show significant surface tension changes in response to different radiation

conditions below the CMC. The largest change in surface tension is as large as 13.5 mN/m[22]. However, the changes in saturated surface tension (i.e. at concentrations well above CMC) are negligible when the fluid is subjected to changing illumination conditions. The largest value reported is only 3 mN/m[37]. These surfactants do not, therefore, fulfill the requirements for some potential applications, and there is scope for the development of new surfactants that will satisfy these needs.

In addition, surfactant adsorption is a dynamic process, in which the diffusion of surfactants from the bulk phase to the interface is usually the controlling step. Correspondingly, whenever a new surface is created, the surface tension gradually decreases until it reaches the equilibrium value and the time scale of this process is determined by the surfactant diffusion. This time-dependent surface tension is referred to as the "dynamic surface tension"[44]. A report on the change in dynamic surface tension in bola type azobenzene surfactants under different illumination conditions indicated that although static surface tension changed little when switching from visible light to UV light, changes in dynamic surface tensions were as large as 20 mN/m. This light-regulated dynamic surface tension has potential applications in some "one-way processes", such as timing the release of a liquid drop[37]. However, for reversible and repeated control of surface tensions, static surface tension is easier to exploit and is much more manageable than dynamic surface tension.

Based on the above analysis, it can be concluded that, for the purpose of predictable and manageable control of surface tensions, a large change in static saturated surface tension is highly desirable in practical applications. In addition, in the future, it is expected that the control of surface tension can be applied extensively in biological systems, so it is also important to develop surfactants exhibiting large surface tension changes at room temperature.

1.2.2 Control of Bulk Properties in Surfactant Solutions

The formation of a microheterogeneous phase through self-assembly in surfactant solutions has important practical implications [1]. The essential point is that, by means of the self-assembly process, an environment of different polarity can be created within

solutions with little energy input. For example, in aqueous surfactant solutions, micelles provide a non-polar environment, while in organic solutions, surfactants can self-assemble into reverse micelles with strong polar "water cores". These microenvironments can accommodate substances that have poor solubility in the bulk phase, and therefore facilitate dissolution of them at the molecular level. For instance, the organic solutes that are difficult to dissolve in aqueous solution can be solubilized into micelles to achieve some level of molecular mixing [45]. Mixing at the molecular level significantly increases

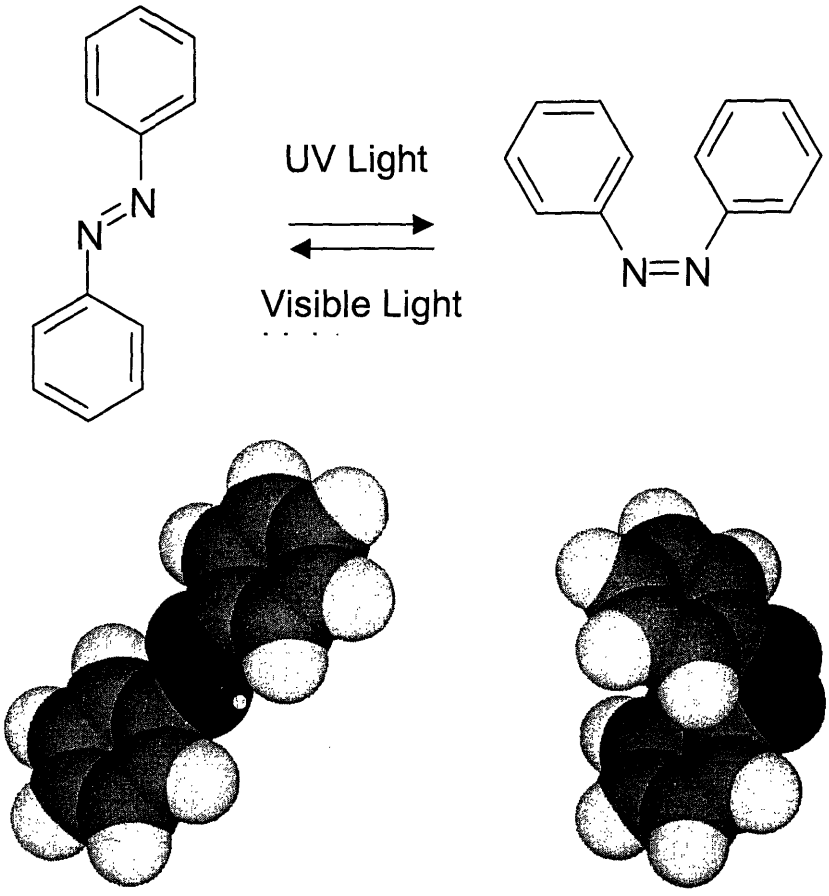

Figure 1-2 Photo-isomerization of azobenzene. The 3D structures show the planar trans and bent cis isomers.

the reaction and transport rates of these substances as a result of the large accessible area. Moreover, the microenvironment can stabilize target molecules and maintain the activity

of biological molecules. Proteins can be preserved in the "water core" of reversible micelles and still provide biological catalytic function in organic solutions, although a protein will lose its activity normally in an organic solvent. In addition, it was found experimentally that micelles can catalyze some reactions, which may be caused by stabilizing the transition state in micelles or at their surfaces.

In practical applications, it will be very useful if self-assembly can be tuned in a controllable and predictive way. Usually, self-assembly can be changed by varying the temperature, pressure or composition of the system. However, controlling self-assembly by this way is not very attractive, partly because other undesirable processes are inevitably introduced with the changes in these thermodynamic variables. The desirable control method should disturb the system as little as possible, so that the system properties will be transparent and manageable. Amongst all these methods, photo-control of self-assembly is perhaps the most promising. First, by means of photo-control, it is possible to change only the properties of the target surfactant, with little perturbation on other components of the system. The control can be highly specific and avoid other unnecessary complexities. Second, it is possible to achieve flexible control with high spatial and temporal resolution. The highest spatial resolution of light is $\lambda/2$, where λ is the wavelength of electromagnetic radiation. Therefore, even using visible light, surfactants can be selectively radiated at a resolution of about 200 nm. Similarly, with modern optical technology, it is not difficult to irradiate systems with different wavelengths alternately at intervals of several hundred milliseconds. As compared with the time scale for self-assembly, which is of the order of milliseconds, this temporal resolution is sufficient. Lastly, photo-control of self-assembly is easy to "interface" with computer technology. Therefore, it is possible to achieve "programmed" self-assembly.

Photoresponsive surfactants can be utilized to achieve photo-control of self-assembly process. Photoresponsive surfactants with azobenzene are very popular. Unlike other photo-responsive groups such as stilbene[46], azobenzene not only shows excellent reversibility and durability in photochemical reaction, but also is also very stable in solution and does not degrade over long periods[3]. The first azobenzene-based photoresponsive surfactant was reported in 1987[47]. When switching between different

illumination conditions, the CMC was found to change reversibly, which indicates photo-control of the formation of micelles. Since the mid 1990's, several studies have been conducted exploiting azobenzene to regulate self-assembly. In addition to micelles, it was found that the formation of vesicles can also be photo-controlled if one surfactant is functionalized with azobenzene[48]. Similarly, permeability of vesicles can be modulated by light, and allow controlled release of metal ions and dyes[24].

However, in these reported surfactants, the changes in CMCs are not very large. From the viewpoint of practical application, a large difference in CMCs under different illumination conditions is desirable. There is still sufficient scope for the development of new photo-responsive surfactants.

1.3 Motivation of this research

As discussed above, the photo-control of both bulk and interfacial properties has been shown to be important in emerging high technologies. The success of these processes strongly depends on the availability of photo-responsive surfactants that exhibit excellent reversibilities, and large changes in physical properties in the control of interfacial and bulk processes. A photoresponsive surfactant, incorporating azobenzene, and exhibiting large and reversible changes in CMC and the static saturated surface tension (surface tensions above the CMC) at room temperature, will satisfy many of the requirements for future applications. Therefore, the objective of this thesis was to design and develop new class photo-responsive surfactants with desirable properties, such as the large changes in saturated surface tension and CMC.

The synthesis and characterization of a new class of photoresponsive surfactants is given in Chapter 2, in which their trans-cis photokinetics are investigated through UV/vis spectrum too. The interfacial properties of these photoresponsive surfactants are examined in Chapter 3 (surface tension) and 4 (neutron reflectivity). Chapter 5 covers the bulk properties of these surfactants, as determined by static and dynamic light scattering, small angle neutron scattering and scanning electron and transmission electron microscopy.

1.4 Bibliography

1. Hiemenz, P. C. & Rajagopalan, R. *Principles of Colloid and Surface Chemistry* (Marcel Dekker, Inc., New York, 1997).

2. Grunze, M. *Science* **283**, 41-42 (1999).

3. Durr, H. in *Photochromism: Molecules and Systems* (eds. Durr, H. & Bousa-Laurrent, H.) 1-14 (Elservier, Amsterdam, 1990).

4. Tanford, C. *The Hydrophobic Effect : Formation of Micelles and Biological Membranes* (Wiley, New York, 1979).

5. Evans, D. F. & Wennerström, H. *The Colloidal Domain : Where Physics, Chemistry, Biology, and Technology Meet* (Wiley-VCH, New York, 1999).

6. Debye, P. *J. Phys. Colloid Chem.* **51**, 18 (1947).

7. Debye, P. *Ann. New York Acad. Sci.* **51**, 575 (1949).

8. Israelachvilli, J. N. *Intermocular and Surface Forces* (Academic Press, London, 1991).

9. Puvvada, S. & Blankschtein, D. Thermodynamics Description of Micellization, Phase-behavior, and Phase-Separation of Aqueous-Solution of Surfactant Mixtures. *J.Phys.Chem.* **96**, 5567-5579 (1992).

10. Rowlinson, J. S. & Widom, B. *Molecular Theory of Capillarity* (Clarendon Press, Oxford, 1982).

11. Hayashita, T., Kurosawa, T., Miyata, T., Tanaka, K. & Igawa, M. Effect of Structural Variation within Cationic Azo-Surfactant Upon Photoresponsive Function in Aqueous-Solution. *Colloid Polym. Sci.* **272**, 1611-1619 (1994).

12. Yang, L., Takisawa, N., Hayashita, T. & Shirahama, K. Colloid-Chemical Characterization of the Photosurfactant 4- Ethylazobenzene 4'-(Oxyethyl)Trimethylammonium Bromide. *J. Phys. Chem.* **99**, 8799-8803 (1995).

13. Abbott, N. L., Jong, L. I. & Shin, J. Y. Nonequilibrium, interfacial properties of aqueous solutions of bolaform surfactants containing disulfide and azobenzene groups. *Abstr. Pap. Am. Chem. Soc.* **218**, 16-COLL (1999).

14. Anastopoulos, A. & Moumtzis, I. A Contribution to the Study of the Inhibited Electroreduction of Organic-Compounds in Anhydrous Solvents at High Electrode Coverages by Neutral Surfactants - the Reduction of Azobenzene in Methanol as a Model Reaction. *J. Electroanal. Chem.* **294**, 143-150 (1990).

15. Buwalda, R. T., Jonker, J. M. & Engberts, J. Aggregation of azo dyes with cationic amphiphiles at low concentrations in aqueous solution. *Langmuir* **15**, 1083-1089 (1999).

16. Carrero, H., Gao, J. X., Rusling, J. F., Lee, C. W. & Fry, A. J. Direct and catalyzed electrochemical syntheses in microemulsions. *Electrochim. Acta* **45**, 503-512 (1999).

17. Cazaux, F. & Coqueret, X. Polydimethylsiloxanes with Vinyl Ether End-Groups .1. Synthesis and Properties as Polymerizable Wetting Agents. *Eur. Polym. J.* **31**, 521-525 (1995).

18. Esumi, K., Miyazaki, M., Arai, T. & Koide, Y. Mixed micellar properties of a cationic gemini surfactant and a nonionic surfactant. *Colloid Surf. A* **135**, 117-122 (1998).

19. Everaars, M. D. et al. Effects of Introduction of Mesogenic Units in Ammonium Amphiphiles on the Aggregation Behavior in Water. *Langmuir* **11**, 3705-3711 (1995).

20. Gehlen, M. H., Ferreira, M. & Neumann, M. G. Interaction of Methyl-Orange with Cationic Micelles and Its Effect on Dye Photochemistry. *J. Photochem. Photobiol. A* **87**, 55-60 (1995).

21. Higuchi, M. & Kinoshita, T. Photoresponsive behavior of self-assembling systems by amphiphilic alpha-helix with azobenzene unit. *J. Photochem. Photobiol. B* **42**, 143-150 (1998).

22. Kang, H. C., Lee, B. M., Yoon, J. & Yoon, M. Synthesis and surface-active properties of new photosensitive surfactants containing the azobenzene group. *J. Colloid Interface Sci.* **231**, 255-264 (2000).

23. Kozlecki, T., Sokolowski, A. & Wilk, K. A. Surface activity and micelle formation of anionic azobenzene- linked surfactants. *Langmuir* **13**, 6889-6895 (1997).

24. Lei, Y. B. & Hurst, J. K. Photoregulated potassium ion permeation through dihexadecyl phosphate bilayers containing azobenzene and stilbene surfactants. *Langmuir* **15**, 3424-3429 (1999).

25. Li, H. Y. & Liu, Z. F. *Synthetic Commun.* **28**, 3779-3785 (1998).

26. Liu, J., Kobayashi, K., Yang, L., Takisawa, N. & Shirahama, K. Binding of photosurfactant (4-butyl-azobenzene-4 ' oxyethyltrimethylammonium bromide) to polyelectrolyte. *J. Colloid Interface Sci.* **213**, 412-416 (1999).

27. Luo, H., Yang, B. X., Yang, L. & Cao, W. X. Interaction of a diazoresin with sodium dodecyl sulfate in aqueous solution. *Macromol. Rapid Commun.* **19**, 291-294 (1998).

28. Morishima, Y., Saegusa, K. & Kamachi, M. Anomalously Blue-Shifted Fluorescence and Phosphorescence of Zinc(Ii) Tetraphenylporphyrin in Highly Constraining Microenvironments in Hydrophobically-Modified Polysulfonates. *Macromolecules* **28**, 1203-1207 (1995).

29. Nakagawa, M., Watase, R. & Ichimura, K. Spatially controlled photoisomerizability of azobenzene moieties in Langmuir-Blodgett monolayers of ion-paired macrocyclic amphiphiles. *Mol. Cryst. Liq.Cryst.* **344**, 113-118 (2000).

30. Neff, G. A., Helfrich, M. R., Clifton, M. C. & Page, C. J. Layer-by-layer growth of acentric multilayers of Zr and azobenzene bis(phosphonate): Structure, composition, and second-order nonlinear optical properties. *Chem. Mat.* **12**, 2363-2371 (2000).

31. Nieuwkerk, A. C., van Kan, E. J. M., Koudijs, A., Marcelis, A. T. M. & Sudholter, E. J. R. Interactions between chromophore-labelled ammonium surfactants and hydrophobically modified polyelectrolytes. *Eur. J. Org. Chem.*, 305-312 (1999).

32. Rosslee, C. & Abbott, N. L. Active control of interfacial properties. *Curr. Opin. Colloid Interface Sci.* **5**, 81-87 (2000).

33. Saji, T. *Abstr. Pap. Am. Chem. Soc.* **211**, 10-COLL (1996).

34. Saji, T. *Abstr. Pap. Am. Chem. Soc.* **218**, 29-COLL (1999).

35. Saji, T., Ebata, K., Sugawara, K., Liu, S. L. & Kobayashi, K. *J.Am.Chem.Soc.* **116**, 6053 (1994).

36. Saji, T., Igusa, Y., Kobayashi, K. & Liu, S. L. *Chem.Lett.*, 401-402 (1995).

37. Shin, J. Y. & Abbott, N. L. Using light to control dynamic surface tensions of aqueous solutions of water soluble surfactants. *Langmuir* **15**, 4404-4410 (1999).

38. Shrestha, N. K., Miwa, I. & Saji, T. Composite plating of Ni/SiC using a cationic surfactant with an azobenzene group. *J. Electrochem. Soc.* **148**, C106-C109 (2001).

39. Yamanouchi, H. & Saji, T. Formation of organic pigment films by photochemical reduction of surfactants containing an azobenzene group. *Chem. Lett.*, 531-532 (1996).

40. Yang, L., Takisawa, N., Kaikawa, T. & Shirahama, K. Interaction of photosurfactants, [[[4'-[(4-alkylphenyl)azo]phenyl]oxy]ethyl]trimethylammomium bromides, with alpha- and beta-cyclodextrins as measured by induced circular dichroism and a surfactant-selective electrode. *Langmuir* **12**, 1154-1158 (1996).

41. Yoshioka, H., Nonaka, K., Fukuda, K. & Kazama, S. Chitosan-Derived Polymer-Surfactants and Their Micellar Properties. *Biosci. Biotechnol. Biochem.* **59**, 1901-1904 (1995).

42. Zhang, Y. J. & Cao, W. X. A novel photosensitive ternary complex consisting of phenol- formaldehyde resin, sodium dodecyl sulfate, and diazo resin. *J. Polym. Sci. A* **38**, 2566-2571 (2000).

43. Zhu, D. M., Wu, X. & Schelly, Z. A. Investigation of the Micropolarities in Reverse Micelles of Triton X-100 in Mixed-Solvents of Benzene and N-Hexane. *J. Phys. Chem.* **96**, 7121-7126 (1992).

44. Chang, C. H. & Franses, E. I. Adsorption Dynamics of Surfactants at the Air/Water Interface: A Critical Review of Mathematical Models,Data, and Mechanisms. *Colloid and Surface A.* **100**, 1-45 (1995).

45. Myers, D. *Surfaces, Interfaces, and Colloids* (Wiley - VCH, New York, 1999).

46. Turro, N. J. *Modern Molecular Chemistry* (University Press, Menlo Park, CA, 1991).

47. Tazuke, S., Kurihara, S., Yamaguchi, H., Amaguchi, H. & Ikeda, T. Photochemically Triggered physical Amplification of Photoresponsiveness. *J.Phys.Chem.* **91**, 249-251 (1987).

48. Sakai, H., Matsumura, A., Yokoyama, S., Saji, T. & Abe, M. Photochemical Switching of Vesicle Formation Using an Azobenzene-modified Surfactant. *J.Phys.Chem. B* **103**, 10737-10740 (1999).

Chapter 2

Synthesis and Characterization of Photoresponsive Surfactants

2.1 Introduction

Many photoresponsive surfactants have been developed and synthesized since the mid-1980s. Although some of them showed large CMC changes in response to different illumination conditions, very few exhibited large surface tensions change above their CMCs. The largest reported reversible change in the saturated surface tension is only 3 mN/m [1]. Almost all photoresponsive surfactants in the literature are ionic, and carry one charged head group [2]. The strong repulsive interaction between these head groups may lead to the formation of a loosely adsorbed layer, in which the molecular area is large. Under such circumstances, it is to be expected that any change in tail conformation would have little effect on surface tension, because the interaction between surfactants, and therefore the surface free energy, would not be strongly influenced by the conformations change — the effect of conformation would be overwhelmed by the large "free volume". The interaction between surfactants, and therefore the molecular area, can, in principle, be decreased when the charged surfactant head is replaced by a non-charged polar group. With this in mind, a new class of nonionic photoresponsive surfactants has been designed and synthesized.

2.2 Synthesis

An homologous series of four new, nonionic surfactants, in which the functional azobenzene group is located within the tail and separated from the ethylene oxide head group by an alkyl spacer of n methylenes, has been synthesized. These surfactants are termed $C_4AzoOC_nE_2$ (n = 2,4,6, and 8). Their structures are shown in Figure 2-1.

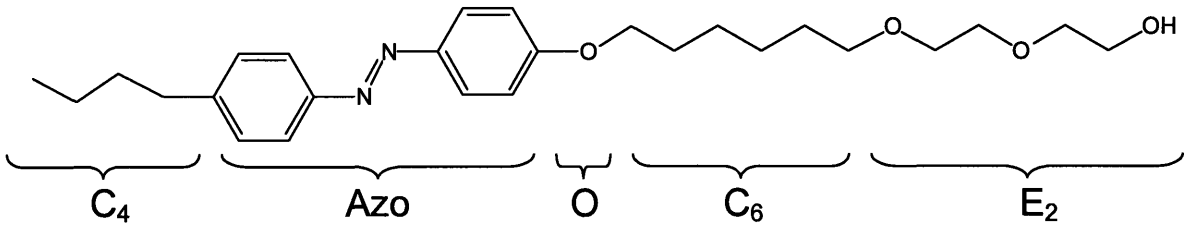

Figure 2-1 Molecular structure of the new class of surfactants $C_4AzoOC_nE_2$; the structure for n = 6 is shown. C_4 = butyl tail group; Azo = azobenzene group; O = ether oxygen middle polar group; C_6 = alkyl spacer with 6 methylene groups; E_2 = surfactant head group consisting of two ethylene oxide moieties.

2.2.1 Materials

4-butylaniline (97%), sodium carbonate (99.95%), phenol (99+ %), di(ethylene glycol) (99%), 1,2-dibromoethane (99+%), 1,4-dibromobutane (99%), 1,6-dibromohexane (96%), 1,8-dibromooctane (98%), bis(trimethylsiyl)trifluoro-acetamide (99+%), and sodium hydride (95%) were purchased from Aldrich (Milwaukee, WI). Sodium nitrite (AR grade), potassium hydroxide (AR grade), hydrochloric acid (37%), and sodium hydroxide (AR grade) were obtained from Mallinckrodt Baker (Paris, Kentucky)], and tetrahydrofuran and hexane from EM Science (Gibbstown, NJ). All chemicals were used as received without further purification.

2.2.2 Synthesis Procedure

The surfactants synthesized were triethylene glycol mono(4-butylazobenzne) ether ($C_4AzoOC_2E_2$), diethylene glycol mono(4',4-butyloxy,butyl-azobenzene) ($C_4AzoOC_4E_2$), diethylene glycol mono(4',4-hexyloxy, butyl-azobenzene) ($C_4AzoOC_6E_2$) and diethylene glycol mono(4',4-octyloxy, butyl-azobenzene) ($C_4AzoOC_8E_2$). The synthesis of $C_4AzoOC_2E_2$ is described here. Similar procedures were used to synthesize the other photoresponsive surfactants.

Preparation of 4-butyl-4'-hydroxyl azobenzene (II) and 4-butyl-4'-(2-brom) ethoxy azobenzene (III) (Figure 2-2) was achieved via a modification of a method available in the literature [3]. Triethylene glycol mono (4-butylazobenzne) ether ($C_4AzoOC_2E_2$) was synthesized through the Williamson reaction [4].

4-butyl-4'-hydroxyl azobenzene (II) was prepared by dissolving 14.9 g of 4-butylaniline in 64 ml of 5M hydrochloric acid and reacting it with 15 ml of aqueous sodium nitrite (6.67 M) at 0 °C for one hour. The resulting diazonium solution was then coupled with phenol in a slurry (9.4 g phenol + 26.5 g sodium carbonate + 50 ml MilliQ water) at 0 °C for one hour. The product was collected by filtration, dried in a vacuum oven over night, and purified by recrystallization in hexane. The yield was 18.0 g or 70%.

4-butyl-4'- (2-brom) ethoxy azobenzene (III) was prepared by first dissolving 10.08 g (II) in 40 ml THF, and adding this solution dropwise to a mixture of 18.787 g 1,2-dibromoethane, 4.49 g potassium hydroxide and 200 ml THF. The mixture was allowed to reflux for 19 hours, and was then extracted with dichloromethane. After the solvent was removed by rotary evaporation, the product was further purified by recrystallization from a hexane/THF mixture (80/20 volume ratio). Yield was 5.35 g or 37%.

Triethylene glycol mono (4-butylazobenzne) ether ($C_4AzoOC_2E_2$) To prepare $C_4AzoOC_2E_2$, 1.98 g of sodium hydride was first reacted with 21.22 g of di(ethylene glycol) in 80 ml THF under N_2 protection for 2 hours. A solution of 3.61g (III) with 40 ml THF was added dropwise into this reaction mixture, and the resulting solution was refluxed for 64 hours under N_2. The solvent was removed from the reaction mixture by rotary evaporation, and vacuum distillation was used to remove residual di(ethylene glycol). The product was separated by chromatography (60 Å silica; ethyl ether/ methanol as eluent), and further purified by recrystallization from hexane. Yield was 0.459 g or 12.0%.

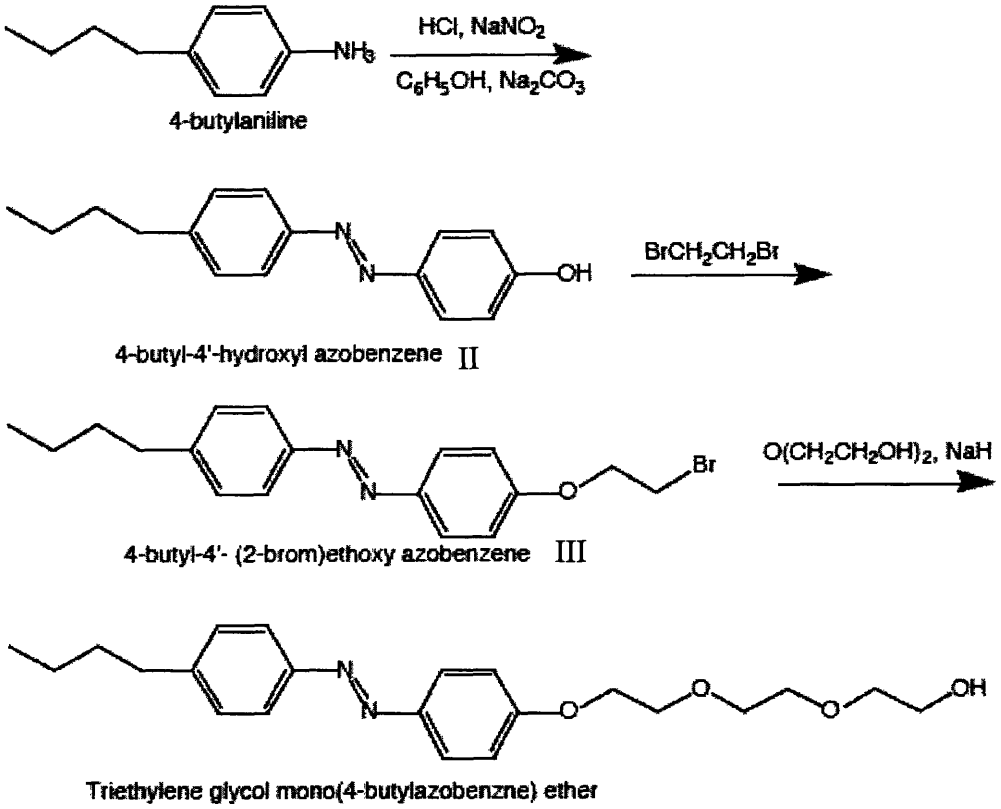

Figure 2-2 Schematic of the synthesis pathway for the surfactant $C_4AzoOC_2E_2$

2.3 Characterization and Analysis

The molecular structure and purity of all surfactants were verified and analyzed by multiple methods, such as ^{1}H-NMR (Bruker Avance DPX-400), mass spectrometry (Bruker DALTONICS APEX, 3 Tesla, FT-ICR-MS, with Electrospray Ion source), elemental analysis and gas chromatography (GC).

2.3.1 Structure Verification

The molecular structures of all surfactants were unambiguously determined through comprehensive analysis by multiple methods. The results are summarized as follows. In Figure 2-3, a typical NMR spectrum is shown for $C_4AzoOC_2E_2$.

$C_4AzoOC_2E_2$: ^1H NMR (400 MHz, $CDCl_3$) δ (ppm) 0.92 (t, 3H, CH_3), 1.35(q, 2H, CH_2), 1.62(q, 2H, CH_2), 1.78 (s, 1H, OH), 2.67 (t, 2H, CH_2), 3.59-3.89 (m, 10H, CH_2CH_2O), 4.20 (t, 2H,CH_2), 7.00 (d, 2H, $H_{aromatic}$), 7.28 (d, 2H, $H_{aromatic}$), 7.77 (d, 2H, $H_{aromatic}$), 7.86 (d, 2H, $H_{aromatic}$). Elemental analysis for $C_{22}H_{30}N_2O_4$. Calculated: C, 68.37%; H, 7.82%; N, 7.25%; O, 16.56%; C/N (molar ratio), 11.0; H/N (molar ratio), 15.0; O/N (molar ratio), 2.0. Found: C, 68.13%; H, 7.90%; N, 7.11%; O, 16.91%; C/N (molar ratio), 11.1; H/N. (molar ratio), 15.4; O/N (molar ratio), 2.1. Molecular weight calculated for $C_{22}H_{30}N_2O_4$: 386.5. Measured by mass spectrometry: 386.2.

$C_4AzoOC_4E_2$ ^1H NMR (400 MHz, $CDCl_3$) δ (ppm): 0.96 (t, 3H, CH_3), 1.40 (q, 2H, CH_2), 1.66 (q, 2H, CH_2), 1.81 (q, 2H, CH_2), 1.93 (q, 2H, CH_2), 2.19 (s, 1H, OH), 2.70 (t, 2H,CH_2), 3.59-3.75 (m, 10H, CH_2CH_2O), 4.10 (t, 2H, CH_2), 7.02 (q, 2H, $H_{aromatic}$), 7.32 (t, 2H,$H_{aromatic}$), 7.83 (d, 2H, $H_{aromatic}$), 7.95 (d, 2H, $H_{aromatic}$). Elemental analysis for $C_{24}H_{34}N_2O_4$.Calculated: C, 69.54%; H, 8.27%; N, 6.76%; O, 15.44%; C/N (molar ratio), 12.0; H/N (molar ratio), 17.0; O/N (molar ratio), 2.0. Found: C, 69.29%; H, 8.34%; N, 6.73%; O, 15.20%; C/N (molar ratio), 12.0; H/N (molar ratio), 17.0; O/N (molar ratio), 2.0. Molecular weight calculated for $C_{24}H_{34}N_2O_4$: 414.6. Measured by mass spectrometry: 414.3.

$C_4AzoOC_6E_2$: ^1H-NMR (400 MHz, $CDCl_3$) δ (ppm): 0.96 (t, 3H, CH_3), 1.39- 1.85 (m, 12H, -CH_2CH_2-), 2.52 (s, 1H, OH), 2.70 (t, 2H, CH_2), 3.50-3.77 (m, 10H, CH_2CH_2O), 4.05 (t, 2H, CH_2), 7.01 (q, 2H, $H_{aromatic}$), 7.31 (t, 2H, $H_{aromatic}$), 7.83 (d, 2H, $H_{aromatic}$), 7.92(d, 2H, $H_{aromatic}$). Elemental analysis for $C_{26}H_{38}N_2O_4$. Calculated: C, 70.56%; H, 8.65%; N, 6.33%; O, 14.46%; C/N (molar ratio), 13.0; H/N(molar ratio), 19.0; O/N(molar ratio),2.0. Found: C, 70.38%; H, 8.94%; N, 6.23%; O, 15.04%; C/N (molar ratio), 13.2; H/N (molar ratio), 20.0; O/N (molar ratio), 2.1. Molecular weight calculated for $C_{26}H_{38}N_2O_4$: 442.6. Measured by mass spectrometry: 442.3.

$C_4AzoOC_8E_2$: ^{1}H NMR (400 MHz $CDCl_3$) δ (ppm): 0.96 (t, 3H, CH_3), 1.37- 1.85 (m, 16H, -CH_2CH_2-), 2.52 (s, 1H, OH), 2.70 (t, 2H, CH_2), 3.47-3.75 (m, 10H, CH_2CH_2O), 4.05 (t, 2H, CH_2), 7.01 (q, 2H, $H_{aromatic}$), 7.31 (t, 2H, $H_{aromatic}$), 7.83 (d, 2H, $H_{aromatic}$), 7.93 (d, 2H, $H_{aromatic}$). Elemental analysis for $C_{28}H_{42}N_2O_4$. Calculated: C, 71.46%; H, 8.99%; N, 5.95%; O, 13.60%; C/N (molar ratio), 14.0; H/N (molar ratio), 21.0; O/N (molar ratio), 2.0. Found: C, 71.36%; H, 9.11%; N, 5.94%; O, 13.44%; C/N (molar ratio), 14.0; H/N (molar ratio), 21.3; O/N (molar ratio), 2.0. Molecular weight calculated for C28H42N2O4: 470.7. Measured by mass spectrometry: 470.3.

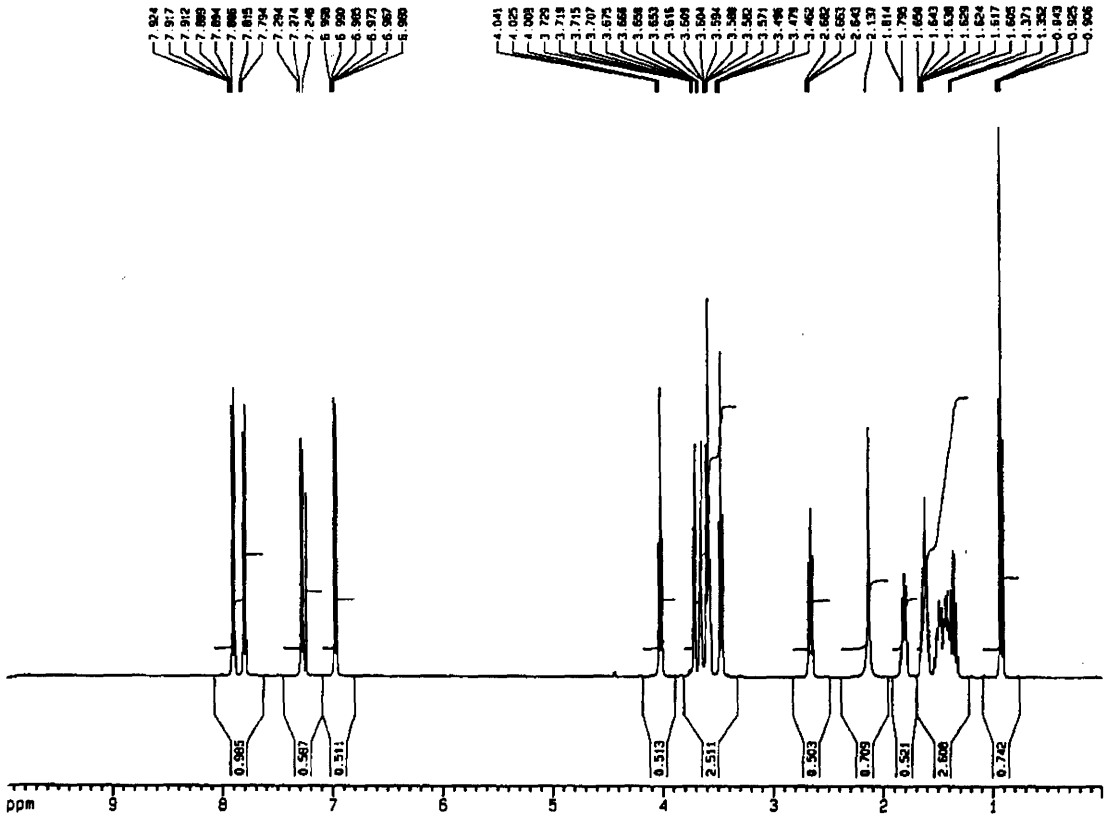

Figure 2-3 ^{1}H-NMR spectrum of $C_4AzoOC_2E_2$. Please refer to text for peak assignments.

2.3.2 Purity Analysis

The surface tension is very sensitive to impurities. Trace amounts of highly surface-active impurities can have significant effects on the surface tension of surfactant solutions, and the surface tension versus concentration curve does not behave as described by Gibbs equation for a single solute. A small dip usually occurs near the CMC. As a result, the surface excess concentration and CMC cannot be determined exactly. Because of the diversity of surfactants and impurities, it is hard to set a criterion for the purity above which the influence of impurities is negligible. However, it is well established from experiments that, whenever the purity of a surfactant is above 99 wt %, the effect of impurities is vanishingly small.

Gas chromatography (GC), one of the most popular methods for purity analysis, could not be used because of the high boiling points of our photoresponsive surfactants. These surfactants do not vaporize at temperatures even as high as 400°C. This high boiling point originates from the hydrogen bonds between surfactants, in which polar hydrogen and oxygen atoms in the ethylene oxide group orient themselves in such a manner that a hydrogen bond is formed between two adjacent molecules. These hydrogen bonds, whose bond energy is of order of fifty k_BT or even higher, considerably increase the intermolecular interactions and lead to high boiling points. In this research, the boiling point of the surfactants was lowered through a derivatization method, by which the polar hydrogen atom in the surfactant was reacted with bis (trimethylsiyl)-trifluoroacetamide to form a nonpolar group [5]. As a consequence, the boiling points of the surfactants were significantly lowered and the derivative could be tested by GC.

The procedure was as follows. A 50 mg sample was dissolved in a 1 ml bis (trimethylsiyl)-trifluoroacetamide in a vial, which was then sealed with a Teflon-lined cap. Then, the mixture was heated for 30 minutes at 70 °C with occasional shaking. The resulting derivative was diluted with THF and cooled down at room temperature before being injected into a GC (HP 5890 with capillary column) and analyzed. The result showed that purity for all products was above 99.0 wt %.

2.4 Reaction Mechanism

The synthetic process consisted of four successive steps. A clear understanding of the mechanism behind these reactions was important. These mechanisms provided the necessary basis for optimizing reaction conditions to avoid undesirable by- products and to maximize the reaction yield.

In this section, the detailed reaction mechanism in which the movement of the reactive electron is traced by arrows is presented for each step in the synthesis of $C_4AzoOC_6E_2$.

The first step (Figure 2-4) In this reaction, the diazonium cation was prepared from butyl-aniline. In acidic solution, sodium nitrite first dissociates to form nitrous acid, in which the lone pair electrons of the oxygen is attacked by a proton, resulting in the detachment of the hydroxyl group. The resulting nitrosyl cation, which is a very active electron receptor, is attacked by the lone pair electrons of the nitrogen in butylaniline. As a result, one nitrogen-nitrogen single bond is formed between butylaniline and the nitrosyl cation, and the positive charge is simultaneously transferred to the low electronegative nitrogen atom. The positively charged intermediate donates the proton to a water molecule, which behaves as the base here. This proton is then transferred back to the oxygen atom in the intermediate. The net result is the displacement of positive charge from nitrogen to oxygen. The resulting intermediate equilibrates with its alternative resonant form, in which the double bond is located between two nitrogen atoms. Then, this alternative resonant form transfers its proton to the water molecule by lone pair electrons attacking from the water oxygen. Finally, the diazonium cation is produced through a dehydration reaction, in which the positively charged oxygen atom is attacked by lone pair electrons from nitrogen. This leads to the detachment of a water molecule. In this step, a proton is needed to activate the sodium nitrite, so the reaction was performed in strong acidic solution. In addition, because of the appearance of the charge, the intermediates in this reaction were very unstable and easily degraded to by-products. Therefore, the reaction must be kept at a low temperature (0 °C) to avoid undesirable side reactions.

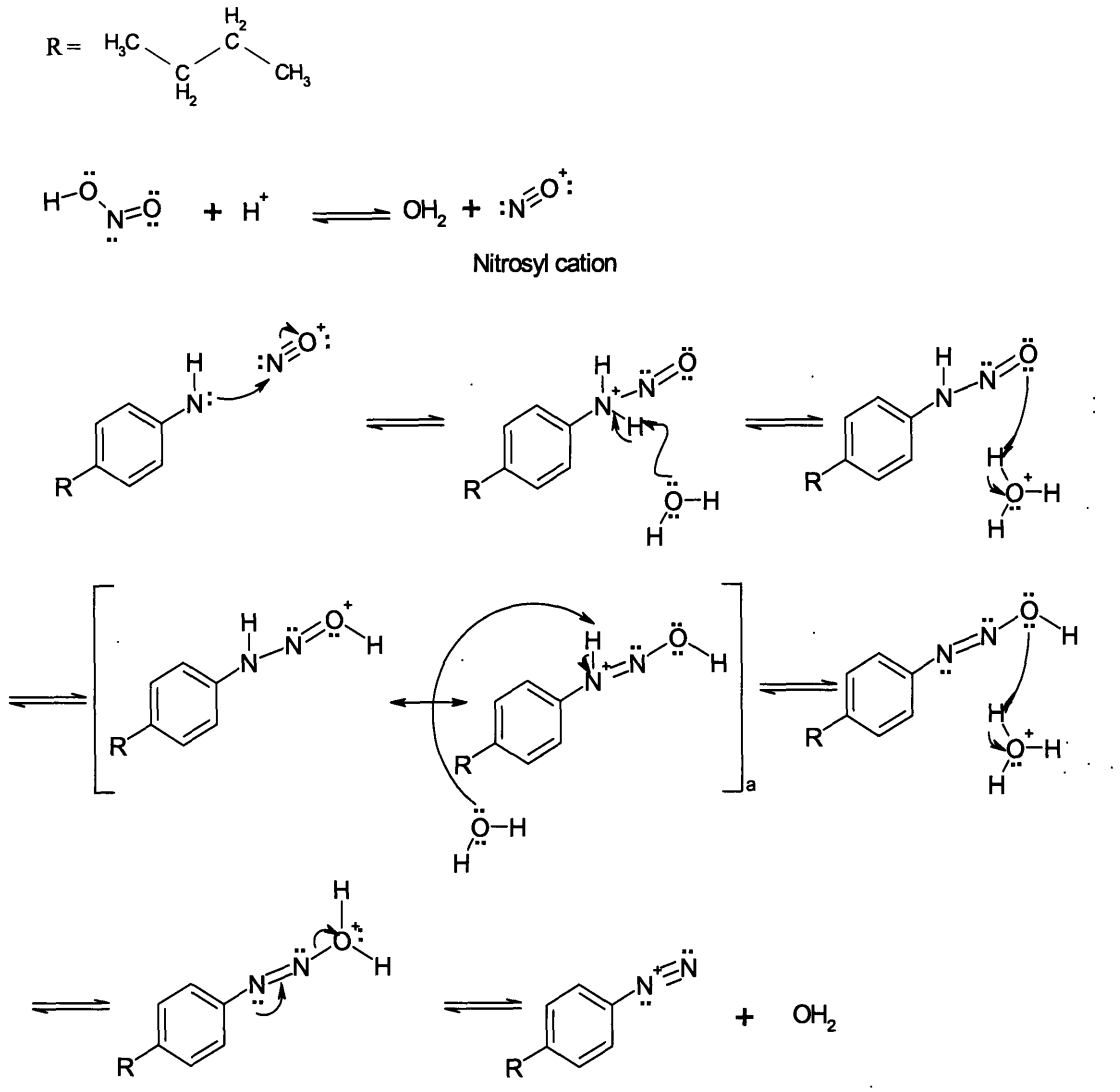

Figure 2-4 The reaction mechanism for the first step

The second step (Figure 2-5) In the second step, the 4,4'-hydroxy, butyl-azobenzene was produced from phenol and diazonium. First, the lone pair electrons from the phenol oxygen attack the positively charged nitrogen in diazonium. As a result, the phenol is

connected covalently to the diazonium and the positive charge is transferred to the phenol oxygen. This charged intermediate is very unstable, and can easily be attacked by the lone pair electron from negatively charged carbonate ion, which is produced by the dissociation of sodium carbonate. As a result, the 4,4'-hydroxy, butyl-azobenzene is generated from this intermediate after receiving one electron from the carbonate ion. In this step, a lone pair electrons donor is needed to facilitate nucleophilic attack, and thus the solution must be kept under basic conditions. Also, the charged intermediate appears in the course of the reaction, so the reaction must be kept at a low temperature, 0 °C in our case.

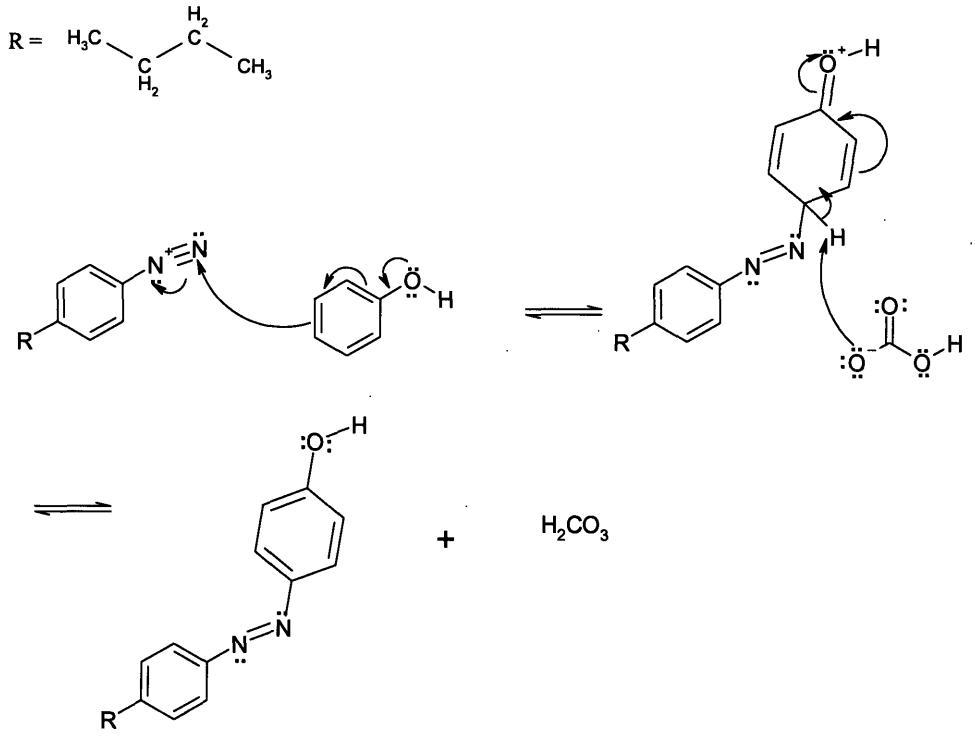

Figure 2-5 The reaction mechanism for the second step

The third step In this step, 4-butyl-4'- (2-brom) hexyloxy azobenzene was synthesized from 4,4'–hydroxyl, butyl-azobenzene and dibromohexane. The O atom of hydroxyl

group at 4,4'-hydroxyl,butyl-azobenzene is attacked by lone pair electrons from OH^-. In the resulting intermediate, the negatively charged oxygen is the nucleophile which attacks the electropositive α-carbon in dibromohexane. As a consequence, dibromohexane is added to the hydroxyl,butyl-azobenzene by detaching one bromide atom. This replacement is the controlling step in this reaction and follows the SN2 reaction mechanism [4], in which the nucleophile collides with a electropositive molecule with an attached leaving group, and replaces the leaving group in a single step. Here, dibromohexane is the electropositive species and bromide is the leaving group. In this step, the 4,4'-butyl,hydroxyl-azobenzene had to be activated by an hydroxyl ion. Therefore, the reaction should be carried out in a basic environment. Protic solvent should be avoided in this step because it slows down significantly the SN2 reaction rate.

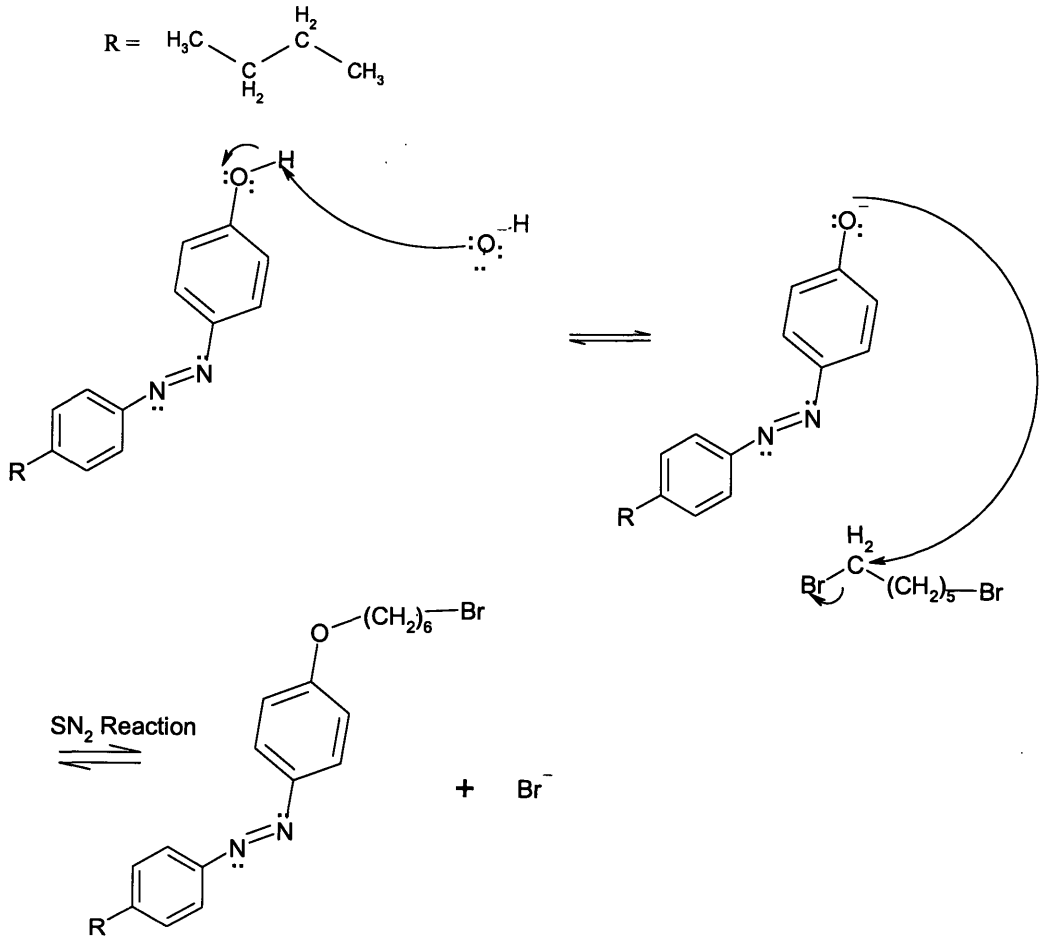

Figure 2-6 Reaction mechanism for the third step

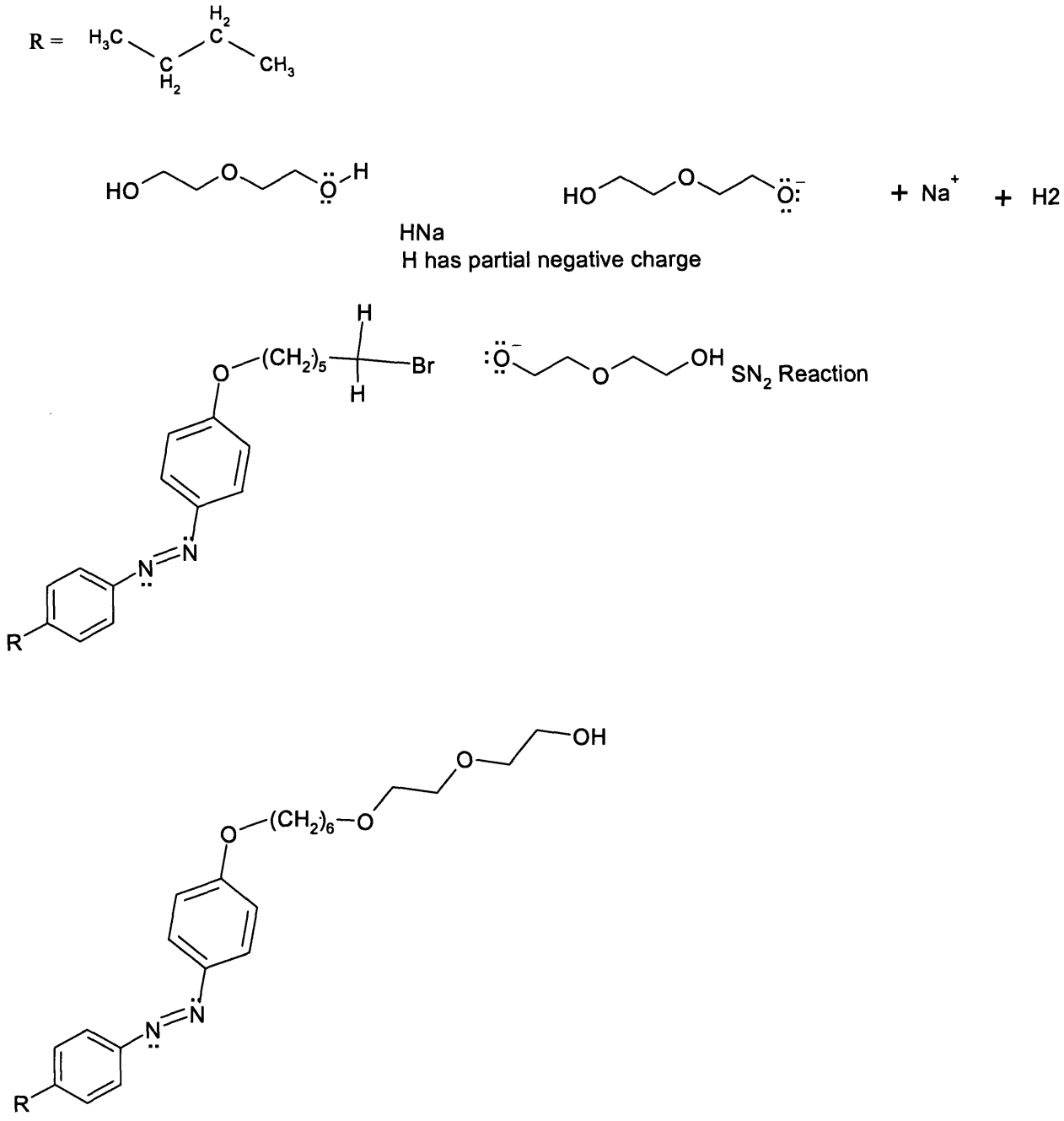

Figure 2-7 Reaction mechanism for the fourth step

The fourth step There are actually two reactions in this step. In the first reaction, the diethylene oxide molecule is activated by reaction with sodium hydride to cause the loss of one proton. This occurs through an attack on the lone pair electron of the O atom in diethylene oxide by the partially negatively charged H of NaH. The activated diethylene oxide is a nucleophile which attacks the electropositive α-carbon in 4-butyl-4'- (2-brom) hexyloxy azobenzene and replaces the bromide group through a SN2 reaction. Because of the SN2 reaction, protic solvents should be avoided. In this step, hydrogen is generated, and the reaction was performed in a nitrogen atmosphere.

2.5 Kinetics of Trans-Cis Photoisomerization

The photoisomerization of azobenzene-containing surfactants can be monitored through their UV-VIS absorption spectra. The trans azobenzene shows a significant absorption peak around 200~300 nm ($\pi \rightarrow \pi^*$ transition band), while the cis form exhibits an additional peak between 400 nm and 500 nm ($n \rightarrow \pi^*$ transition band) (Figure 2-8) [6]. Because of the restriction of molecular symmetry, electronic excitation in the $n \rightarrow \pi^*$ band is essentially prohibited in the trans isomer, so the absorbance of the trans form in the $n \rightarrow \pi^*$ transition band is almost zero [6]. Therefore, by tracking the absorbance change in the $n \rightarrow \pi^*$ band, the concentration of cis isomer can be determined during photoisomerization, and quantitative kinetic information can be acquired. In this section, we first introduce the photoisomerization mechanism of azobenzene from a fundamental perspective, and then present our kinetic study on the photoisomerization of the surfactant $C_4AzoOC_6E_2$.

2.5.1 Mechanism of Photoisomerization in Azobenzene

Since the discovery of photoisomerization in azobenzene, the mechanism has been studied for more than 50 years. Recently, with advances in computational quantum mechanics, there has been considerable progress in understanding the mechanism of photoisomerization by combining experimental studies with theoretical computation. Although there is still some debate, the basic mechanism has been established [6].

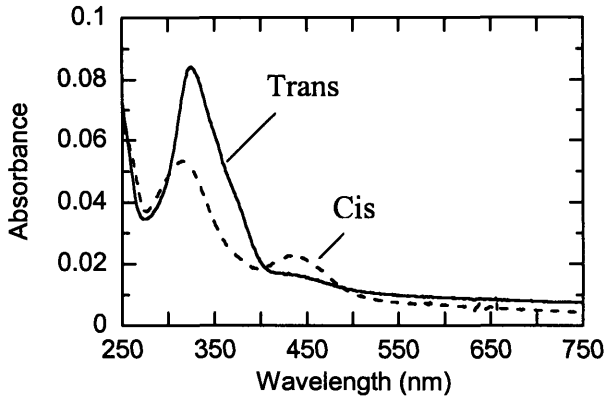

Figure 2-8 UV-vis absorption spectra for C4AzoOC6E2 solutions (0.01 mM) before UV illumination (solid line) and after UV illumination (broken line)

The photoisomerization mechanism is best described in terms of the potential energy surface (PES), in which the molecular energy is plotted against all possible atomic nuclear configurations[7]. The states of the reactant and the product are represented by the points of minimum energy on the PES. The time course of reaction can be approximated by the path connecting the reactant and product points on the PES, along which the saddle point corresponds to the transition state. In a reaction involving many atoms, the PES is very complicated. However, in the photoisomerization of azobenzene, the PES can be dramatically simplified by reducing all atomic coordinates to only one relevant variable, the relative distance between two benzene rings, which carries most of the information of molecular conformation during photoisomerization.

Currently, it is generally thought that trans and cis azobenzene follow different mechanisms in their photoisomerizations [6]. In trans-to-cis isomerization, trans is converted to the cis form via a "rotation mechanism", in which the bond order in the N, N double bond is substantially decreased and the azobenzene relaxes to the perpendicular transition state (Figure 2-9a). In this transition state, the two benzene groups are perpendicular to each other. However, in the cis-to-trans reaction, the photoisomerization occurs via an "inversion mechanism", in which the transition state is planar and the N atom has an sp-hybridized geometry (Figure 2-9b). The potential energy diagram for both trans-to-cis and cis-to-trans photoisomerization is shown in Figure 2-10. The trans isomer is easily excited to the (π,π^*) state by absorbing a photon with wavelength

between 200 ~ 300 nm (the $n \rightarrow \pi^*$ transition was forbidden because of the molecular symmetry). The excited species then leaks to the basin of $(n, \pi^*)^2 S$ — the second (n, π^*) excited state, in which the relative position between the two benzene rings has changed significantly. From there, the high energy intermediate jumps back to the ground state through a " funnel". The "funnel" is a special excited state conformation, for which the energy gap between the ground state and the excited state is a minimum. The funnel is usually located at the basin of the excited state, and there is a peak in the ground state

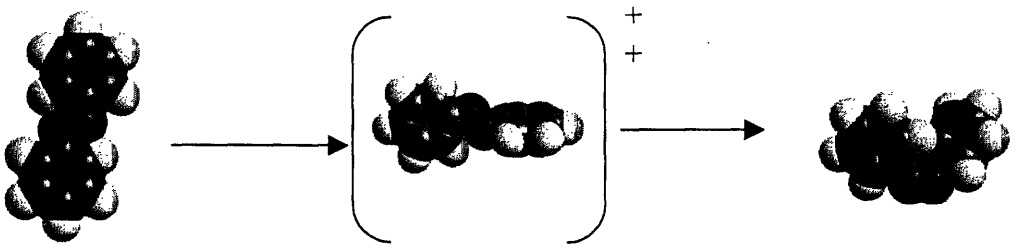

Trans Cis

(a)

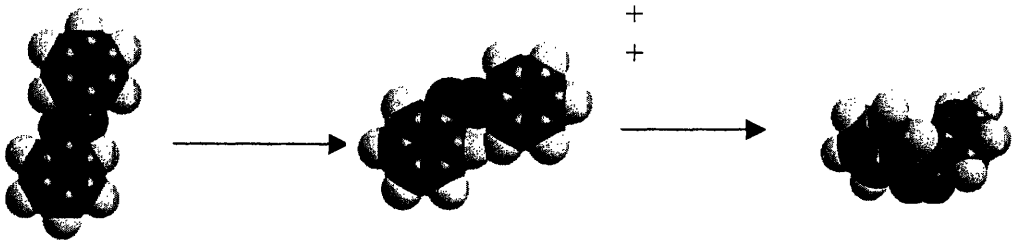

Trans Cis

(b)

Figure 2-9 Mechanism of photoisomerization in azobenzene. The transition state is bracketed and labeled with double "+". (a) Rotation mechanism (b) Inversion mechanism.

right beneath it, as shown schematically in Figure 2-10. In this jumping process, there is no significant change in nucleus configuration, only electronic events are involved. Then, the intermediate, which is on the top of the ground state, slides down to the cis state through a series of adjustments in nucleus configuration. Finally, the trans converts to cis. The above explanation requires that the internal conversion rate from (π,π^*) to (n,π^*) must be very low. It can be inferred from experimental data that there is an unusually large energy gap between these states. The energy distance of the Franck-Condon states (in these states, only electronic events are involved, with no significant nuclear movement) has been found to be around 6000 to 8000 cm^{-1}, so it is reasonable to expect that energy gap between these states may be near 10,000 cm^{-1}. This large energy gap effectively prevents the internal conversion from (π,π^*) to (n,π^*) [6].

The photoisomerization of cis-to-trans is relatively simple and straightforward. First, the cis isomer jumps to the (n,π^*) state through visible light excitation, and reaches the low energy locus after a series of variations in nucleus configuration. Then, the excited species returns to the ground state through the "funnel", and gradually comes to the trans state. The net result in both photoisomerization processes is that the azobenzene acquires enough energy from absorbing photons to cross an energy barrier located between the trans and cis states. As argued in the previous paragraph, the internal conversion between (π,π^*) to (n,π^*) is pretty low. Therefore, the cis forms in the (π,π^*) almost completely jump back to the ground state radiatively.

As shown in the energy diagram, there is one significant difference between the "rotation mechanism" and the "inversion mechanism". In the "rotation mechanism", there is small electronic coupling between (π,π^*) and $(n,\pi^*)^2S$. This coupling gives the species in the (π,π^*) state the possibility to go cross the rotational barrier to the "phantom" state, which was indicated by dashed line in Figure 2-10. In "inversion mechanism", there was no such electronic coupling and no "phantom" state appeared [6].

2.5.2 Photoisomerization Kinetics in Photoresponsive Surfactant Solutions

The dynamic properties of photoresponsive surfactant systems play an important role in many practical applications. Understanding them thoroughly is imperative to achieve flexible and exact surface tension control, and to design effective and reliable systems for any practical purposes.

In this section, we first describe the experimental method used in our kinetic study. Then, based on the photoisomerization mechanism that in the last section, a simplified kinetic model is proposed, and the kinetic data are analyzed in terms of this kinetic model. Finally, we report results on the photoreversibiity in $C_4AzoOC_6E_2$ aqueous solution.

2.5.2.1 Experimental method

The kinetics of both trans-to-cis and cis-to-trans conversions were investigated. To prepare the cis surfactant system, the aqueous surfactant solution was loaded into a quartz cuvette, and illuminated with narrow band UV light for 30 minutes. The trans surfactant system was prepared by a similar method, but illuminated with visible light for 30 minutes. The light source used in this study was a 200W mercury lamp (Oriel 6283) mounted in an arc lamp housing (Oriel 66902) and powered by an arc lamp power supply (Oriel 68910). Monochromatic UV light was obtained by using a 320 nm band pass filter (Oriel 59800). A 400 nm long pass filter (Oriel 59472) was utilized to obtain visible radiation.

The kinetic measurements were conducted as follows. The initially prepared trans (or cis) surfactant system was illuminated by UV (or visible) light in a well-controlled manner, in which the illumination time was exactly controlled by careful operation of the lamp shutter. After each illumination, the absorbances at both trans and cis bands were recorded by a Hewlett-Packard HP 8453 spectrophotometer. The process continued until the system reached its photo-stationary equilibrium. Each kinetic experiment was performed at least three times. The data were very reproducible.

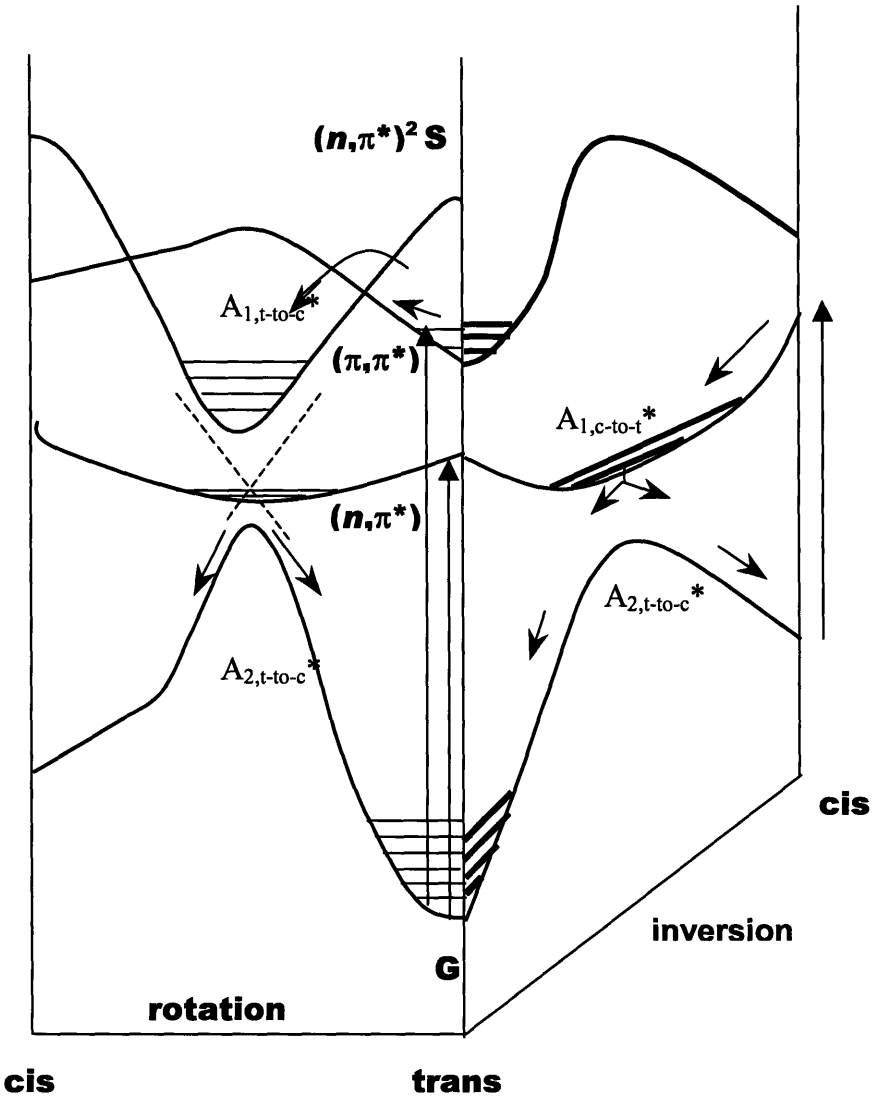

Figure 2-10 Energy diagram of trans-to-cis and cis-to-trans photoisomerization. G represents the ground state. The (π,π^*) and (n,π^*) indicate the $\pi \rightarrow \pi^*$ and $n \rightarrow \pi^*$ excited states, respectively. The $(n,\pi^*)^2S$ represents the second $n \rightarrow \pi^*$ excited state. At each stable state, vibrational energy levels are represented by parallel horizontal lines.

2.5.2.2 Kinetic model

As presented in section 2.5.1, the detailed photoisomerization mechanism is complicated, with many intermediates and many electronic events involved. In addition, the trans-to-cis and cis-to-trans transitions proceed along totally different pathways.

However, from a practical viewpoint, a simple and accurate kinetic model is desirable, by which the most important characteristic of the kinetics can be captured. It will be shown that the kinetic model can be significantly simplified by making rational approximations.

Because the absorption bands are well-separated and the wavelength range of the illumination was narrow, only the conversion from trans to cis (or cis to trans, depending on the wavelength of illumination) was significant. Accordingly, the trans to cis conversion (an analogous analysis holds for the cis to trans conversion) could be modeled as the simple irreversible reaction,

$trans \xrightarrow{UV} cis$ or, more generally, $A \xrightarrow{h\nu} B$

The absorption of photons leads to some high-energy excited species. As shown above, there are usually several such intermediates, with pathways and lifetimes that depend on what molecules were excited, and what excited states they are in. However, by applying Franck-Condon principle [7], it is possible to pick out one or two intermediates that are most relevant to the kinetics. These intermediates are termed the "control species", whose reaction rates are slow relative to that of other excited species. The Franck-Condon principle states that the typical time scale of electronic events is far smaller than that of nuclei movement. As a result, the rate constant in a reaction where only electronic transitions occur, is much larger than reactions that involve nuclear displacement. Following this guideline, it is obvious that intermediates at the bottom of first excited state A_1^*, and on the peak of ground state A_2^*, are control species, as both of them are involved in the processes with significant nuclear movement (Figure 2-10). The proposed kinetic model is,

$$A \xrightarrow{\varepsilon_A I_0} A_1^* \xrightarrow{k_1} A_2^* \xrightarrow{k_d} B \qquad (2\text{-}1)$$
$$\uparrow \quad k_r \quad \downarrow$$

where ε_A is the molar absorption coefficient and I_0 is the local illumination intensity. The rate constant of conversion from A_1^* to A_2^* is k_1. The rate constants of reversion to A_2^* and conversion to B are k_r and k_d, respectively. This model can be further simplified based on the experimental observation that neither fluorescence nor phosphorescence was detected in these photoresponsive surfactants solutions (QuantaMaster

Spectrophotometer, Photon Technology International Inc.), consistent with literature reports that most azobenzene groups are essentially nonemitting [6]. This experimental evidence indicates that the lifetimes of excited species A_1^* and other are short, and that, the excited species revert back to A non-radiatively. As a result, behavior of A_1^* can be approximated well by the quasi-steady state approximation,

$$\frac{d}{dt}[A_1^*] = \varepsilon_A I_0[A] - k_1[A_1^*] = 0 \tag{2-2}$$

from which $[A_1^*] = \frac{\varepsilon_A I_0}{k_1}[A]$. Substituting this into the kinetic equations for scheme (2-1), leads to

$$\frac{d}{dt}[A] = -\varepsilon_A I_0[A] + k_r[A_2^*] \tag{2-3}$$

$$\frac{d}{dt}[A_2^*] = \varepsilon_A I_0[A] - (k_r + k_d)[A_2^*] \tag{2-4}$$

$$\frac{d}{dt}[B] = k_d[A_2^*] \tag{2-5}$$

These kinetic equations corresponds exactly to the following kinetic model,

$$A \underset{k_r}{\overset{\varepsilon_A I_0}{\rightleftarrows}} A_2^* \xrightarrow{k_d} B \tag{2-6}$$

in which only the excited species A_2^* is relevant since A_1^* disappears as soon as it is formed as a result of its short lifetime (i.e. large k_1).

2.5.2.3 Data Analysis

Given the initial concentration of species A, $[A]_0$, kinetic equations (2-3) and (2-4) can be solved readily to give the concentrations of all species as a function of time. Mass conservation holds at every point in the solution such that

$$[A] + [A_2^*] + [B] = [A]_0 \tag{2-7}$$

In general, the intensity I will depend on the position within the vial owing to absorption by both A and B within the solution. Since the concentrations of these two species were low, however, and since the path length was short, the fraction of incident photons absorbed was small, and I ($\approx I_0$) can be assumed to be constant through the solution.

Because only two species are independent, the kinetic equations reduce to

$$\frac{d}{dt}[\tilde{A}] = -\varepsilon_A I_0[\tilde{A}] + k_r[\tilde{A}_2^*] \tag{2-8}$$

$$\frac{d}{dt}[\tilde{A}_2^*] = \varepsilon_A I_0[\tilde{A}] - (k_r + k_d)[\tilde{A}_2^*] \tag{2-9}$$

where $[\tilde{A}] = \frac{[A]}{[A]_0}$ and $[\tilde{A}_2^*] = \frac{[A_2^*]}{[A]_0}$ are dimensionless concentrations of species A and A_2^*, respectively. Experimental evidence indicates that [A*] is small, and we again make the quasi-steady-state approximation that $d[A_2^*]/dt \sim 0$, so that equations (2-8) and (2-9) combine to yield

$$\frac{d}{dt}[\tilde{A}] = -\varepsilon_A I_0(\frac{k_d}{k_d + k_r})[\tilde{A}] = -\varepsilon_A I_0 \phi[\tilde{A}] \tag{2-10}$$

Under initial conditions that at $t=0$, $[\tilde{A}] = 1$, the solution is given by

$$[\tilde{A}] = e^{-\varepsilon_A I_0 \phi t} \tag{2-11}$$

where $\phi = k_d/(k_d + k_r)$ is the quantum efficiency, reflecting the fraction of the excited species yields the final product.

The kinetic curves for $C_4AzoOC_6E_2$ undergoing trans-to-cis and cis-to-trans conversion are shown in Figure 2-11. The illumination intensities are 1.1×10^{-4} mol photons (330 nm)/m^{2}s for trans-to-cis, and 1.3×10^{-4} mol photons (440 nm)/m^{2}s for cis-to-

trans, respectively. Extinction coefficients determined in separate experiment are ε_A = 3360 m^2/mol for the trans and 920 m^2/mol for the cis isomer at 330 and 440 nm,

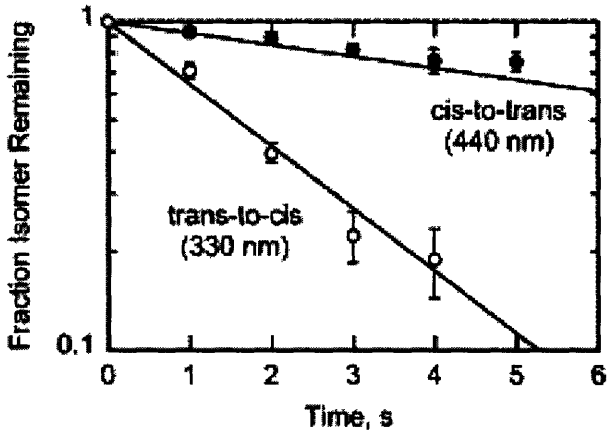

Figure 2-11 Kinetics of photoisomerization in $C_4AzoOC_6E_2$ solutions for the trans-to-cis and cis-to-trans processes under similar irradiation intensities. Solid lines represent least squares fits of the kinetic model to the data.

respectively. For the trans-to-cis conversion, the inverse time constant of $\varepsilon_A I_0 \phi$ = 0.43 ± 0.02 s^{-1} compares favorably with the irradiation rate of $\varepsilon_A I_0$ = 0.40 s^{-1}, from which it can be inferred that the quantum efficiency is close to unity, that is, $\phi \approx 1$. The inverse time constant $\varepsilon_A I_0 \phi$ of 0.083 ± 0.004 s^{-1} for the cis-to-trans isomerization, however, is lower than the actual radiation rate of $\varepsilon_A I_0$ = 0.12 s^{-1}, consistent with a quantum efficiency of approximately 0.69 for this process. The different quantum efficiencies determined here may reflect the different reaction mechanisms in these two photoisomerization processes. The similar values between inverse time constant and irradiation rate in both trans-to-cis and cis-to-trans conversions indicates that both photoisomerizations are mainly externally controlled, their reaction rate are determined primarily by the irradiation intensity and their extinction coefficients.

During above analysis, we assume that trans isomers almost completely convert to cis form under UV illumination, although cis forms have a significant (π,π^*) band. As

argued above, the large energy difference between (π,π^*) and (n,π^*) states made the internal conversion between these two states is very low, and most excited (π,π^*) cis forms are return to ground state radiatively. Therefore, even at the photostationary equilibrium, there are very little cis froms in the solution under UV illumination. This argument is actually proved by our experimental kinetic data. The analysis of kinetic data is a little complicated because of the absence of extinction coefficient of cis form at the (π,π^*) state. However, this problem can be solved by trial and error method. First, we assume an equilibrium concentration of trans form under UV illumination; then, we can obtain the concentration of cis form from mass balance, and therefore its extinction coefficient at (π,π^*) band. Because only cis form absorbs photons at the (n,π^*) band, therefore the concentrations of cis form can be obtained from (n,π^*) absorbance during photoisomerization. These concentrations are used to calculate the concentrations of trans isomer during illumination through $\frac{1}{l\varepsilon_{trans}^{320}}(A_{320}(t)-\frac{\varepsilon_{cis}^{320}}{\varepsilon_{cis}^{400}}A_{400}(t))$, $A_{320}(t)$ and $A_{400}(t)$ are the absorbances at (π,π^*) and (n,π^*) bands, respectively; ${\varepsilon^{320}}_{cis}$ and ${\varepsilon^{400}}_{cis}$ are the extinction coefficients of cis form at (π,π^*) and (n,π^*) bands, respectively; ${\varepsilon^{320}}_{trans}$ is the concentration of trans form at (π,π^*) band; and l is the length of light path. These trans concentrations are fitted by kinetic equation, and the equilibrium concentration is obtained through extrapolating the fitted curve to infinite time. Through comparing the calculated trans concentration with assumed one, we can validate our assumption. The calculation result verifies that trans equilibrium concentration is negligible (smaller than 2%) under UV illumination.

2.5.3 Reversibility of Photoisomerization

The reversibility of photoisomerization was tested by alternately illuminating aqueous surfactant solutions with UV and visible light. At the end of each illumination period, the change in the trans population for any given surfactant was assessed by the changes in its UV/Vis absorption spectrum. All surfactants showed good reversibility. A typical result is shown in **Figure 2-12**, in which the absorbance of $C_4AzoOC_6E_2$ at its

trans absorption band was recorded after 5 min and 2 min irradiation with UV and visible light, respectively, in each cycle. Over the number of cycles investigated, there was no apparent loss of photoreversibility as the absorbance maxima and minima were essentially independent of cycle number.

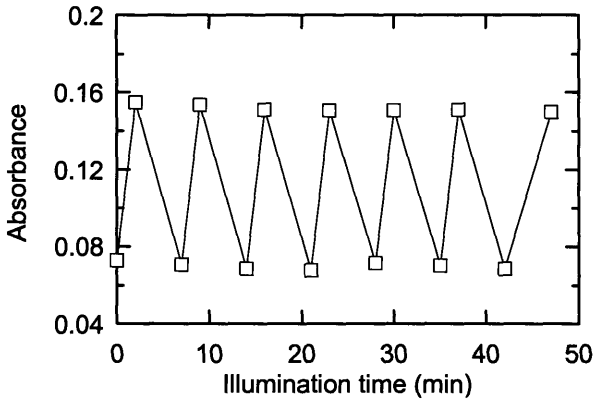

Figure 2-12 Reversibility of photo-isomerization in $C_4AzoOC_6E_2$ solutions (0.02 mM). The sample was alternatively illuminated with UV and visible light for 5 and 2 min, respectively. The absorbance at the trans band was recorded after each illumination.

2.6 Summary

We have designed and synthesized a new class of photoresponsive surfactants having two distinct features relative to those in the literature. First, these surfactants are nonionic, with two ethylene oxide units as the head group. The absence of strong electrostatic repulsions may allow them to form a dense adsorbed layer at the interface. We expect that the effect of photoisomerization on the surface tension in a dense adsorbed layer may be larger than in a loose layer. Second, these surfactants possess a middle polar group, the ether oxygen, which is located in the middle of the hydrophobic moiety. The middle polar group is connected to the surfactant head by an alkyl chain

(spacer), whose length (the number of methylene group) varies from 2 to 8 in this research.

The molecular structure of these surfactants has been verified by ^{1}H NMR, elemental analysis, and mass spectra. The purity of the final product was found to be above 99 wt % as analyzed by gas chromatography. The detailed reaction mechanisms for all major reaction steps were analyzed using "electron pushing" considerations. From this analysis, the optimal reaction conditions can be found to maximize reaction yield and avoid side-reactions.

A detailed mechanism for the photoisomerization process in azobenzene was presented in terms of energy diagram; this knowledge was important in constructing a simple and representative model for the photoisomerization kinetics. Trans-to-cis and cis-to-trans isomerizations may occur through different mechanisms. Trans is thought to convert to cis by a "rotation mechanism", while cis converts to trans through an "inversion mechanism". Based on this knowledge, a kinetic model was proposed, in which all intermediates can be modeled as a single excited species. The experimental kinetic data have been analyzed by this model with satisfactory results. It was found that the quantum effiency in tran-to-cis was close to 1, while it was about 0.69 in cis-to-trans. The different quantum efficiencies may reflect the different reaction mechanisms in these two photoisomerization processes.

2.7 Bibliography

1. Abbott, N. L., Jong, L. I. & Shin, J. Y. Nonequilibrium, interfacial properties of aqueous solutions of bolaform surfactants containing disulfide and azobenzene groups. *Abstr. Pap. Am. Chem. Soc.* **218**, 16-COLL (1999).

2. Rosslee, C. & Abbott, N. L. Active control of interfacial properties. *Curr. Opin. Colloid Interface Sci.* **5**, 81-87 (2000).

3. Li, H. Y. & Liu, Z. F. *Synthetic Commun.* **28**, 3779-3785 (1998).

4. Mcmurry, J. *Organic Chemistry* (Wadsworth, Inc, Belmont, California, 1992).

5. Szymanowski, J., Szewczyk, H. & Hetper, J. *Tenside Detergents* **18**, 333 (1981).

6. Durr, H. in *Photochromism: Molecules and Systems* (eds. Durr, H. & Bousa-Laurrent, H.) 1-14 (Elservier, Amsterdam, 1990).

7. Turro, N. J. *Modern Molecular Chemistry* (University Press, Menlo Park, CA, 1991).

Chapter 3

Interfacial Properties of Photoresponsive Surfactants

3.1 Introduction

An understanding of interfacial properties of photoresponisve surfactants under different illumination conditions is important for their application in a wide range of potential processes. From the Gibbs equation, important structural information about the adsorbed surfactant layer, such as the surface excess concentration, and the area occupied per molecule, can be acquired by analyzing surface tension data[1]. In this chapter, equilibrium surface tensions of aqueous surfactant solutions are reported at different surfactant concentrations before and after UV illumination. The changes in surface tension and the structures of the adsorbed layers under different irradiation conditions are elucidated based on these data.

3.2 Surface Tension Measurements

The equilibrium surface tension was measured at a temperature of 25 °C with a Krüss K10T tensiometer using the Wilhelmy plate method. A chart recorder was used to trace the surface tension variation with time. The surface tension of the trans form was measured under ambient light, while in the cis form, the surface tension was measured in the dark after radiating the sample with UV light for 30 minutes. The raw results are represented in Figure 3-1. An initial of these data at concentrations just below the CMC using the Gibbs equation indicated that the molecular areas in the trans $C_4AzoOC_4E_2$ and $C_4AzoOC_6E_2$ surfactants were abnormally small. The value for trans $C_4AzoOC_6E_2$ was about 14 $Å^2$, which was even smaller than the cross sectional area of the methyl group 18 $Å^2$. In the next section, we discuss the reasons for these physically-unrealistic parameters, and indicate how we must correct for the loss of surfactants from the bulk to the interface in the analysis to obtain physically-meaningful results.

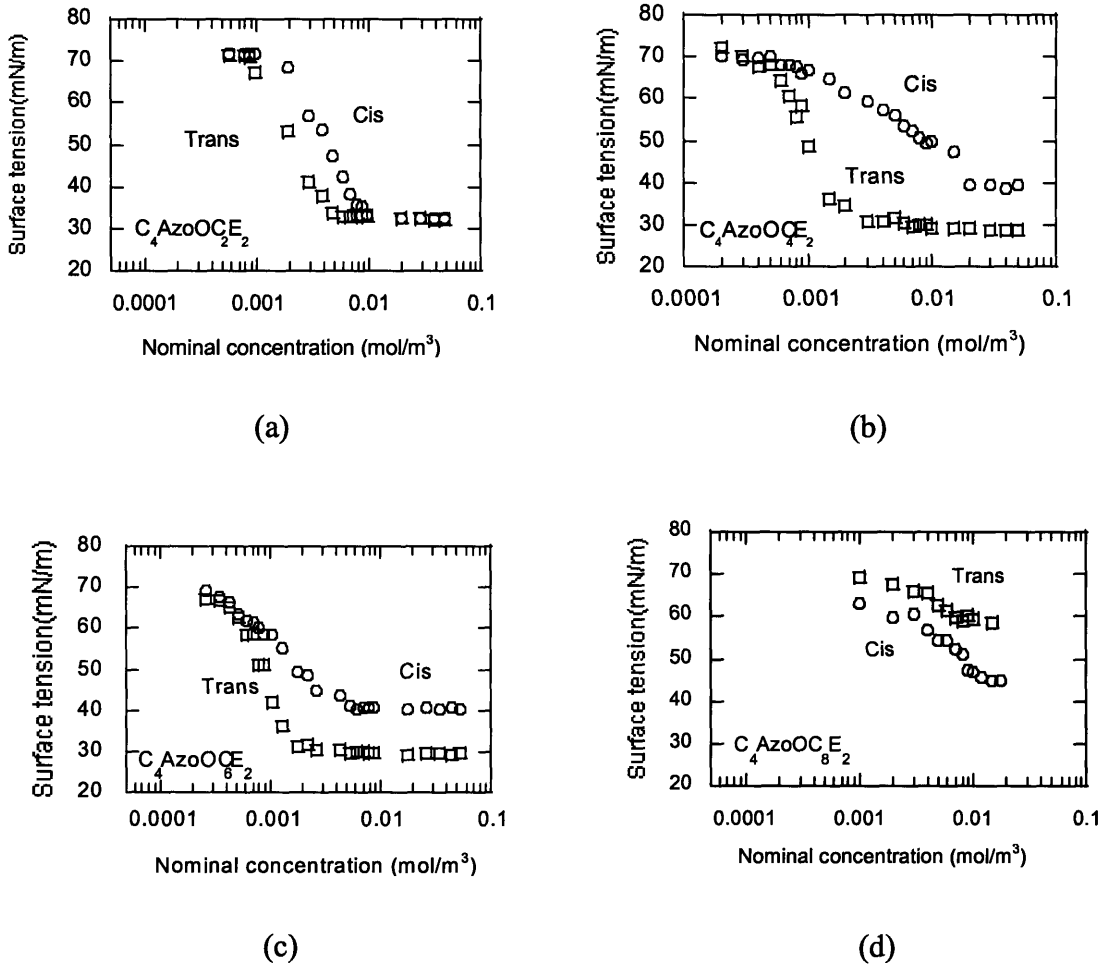

Figure 3-1 Concentration dependence of the equilibrium surface tension for photoresponsive surfactants at 25 °C under both visible (squares) and UV light (circles) illumination. (a) $C_4AzoOC_2E_2$ (b) $C_4AzoOC_4E_2$ (c) $C_4AzoOC_6E_2$ (d) $C_4AzoOC_8E_2$

3.2.1 Estimation of True Bulk Concentration and Surface Excess Properties

In many cases, the moles of surfactant adsorbed at the air-water interface constituted a significant proportion of the total number of moles introduced to the

measurement trough. Therefore the true bulk concentration C_b was less than the nominal concentration C_{nom} by an amount determined by the mass balance equation

$$C_b = C_{nom} - \frac{A}{V}\Gamma \tag{3-1}$$

where A/V is the ratio of the gas-liquid interfacial area to the sample volume in the surface tension measurement; and Γ is the surface excess concentration in moles per unit area.

The true bulk and surface excess concentrations were estimated by using a model to relate the surface tension, surface excess concentration and true bulk concentration to the nominal bulk concentration. The appropriate model parameters were extracted by least squares regression of this model to the experimental data. We relate the surface excess concentration to the true bulk solution concentration through the Frumkin isotherm, which extends the ideal Langmuir adsorption model by incorporating non-ideal surfactant interactions within the interface through the application of regular solution theory [2]. This isotherm can be written as

$$kC_b = \frac{\Gamma}{\Gamma_\infty - \Gamma}\exp\left[-2\left(\frac{h}{RT}\right)\frac{\Gamma}{\Gamma_\infty}\right]] \tag{3-2}$$

where $k\Gamma_\infty$ is the limiting surfactant partition coefficient between the interface and the bulk solution at low surface pressure, and h is the infinite dilution surface partial molar heat of mixing of the surfactant at the interface. The surface excess concentration, Γ, of the surfactant is related to the slope of the surface tension curve with respect to the true bulk concentration through the Gibbs adsorption isotherm [1],

$$\Gamma = -\frac{1}{RT}\frac{d\gamma}{d\ln c} \tag{3-3}$$

where R is the gas law constant and T the absolute temperature. This equation can be integrated directly to yield the surface tension as a function of the surface excess concentration by applying the Frumkin isotherm to eliminate the true bulk concentration:

$$\gamma = \gamma_0 + \Gamma_\infty RT\left[\ln\left(1-\frac{\Gamma}{\Gamma_\infty}\right)+\frac{h}{RT}\left(\frac{\Gamma}{\Gamma_\infty}\right)^2\right] \tag{3-4}$$

where γ_0 is the surface tension of pure water, i.e., 72 mN/m.

Equations (3-1)-(3-4) relate the surface tension and the true bulk concentration to the nominal bulk concentration parametrically through the surface excess concentration. Thus, for a given set of data relating experimental surface tension values to the nominal concentration, we extracted the appropriate model parameters by least squares regression, and evaluated the true surface tension versus bulk concentration curves, and the true surface excess concentrations. The fitting procedure is summarized in Figure 3-2. As an example, the results are plotted together with experimental data in Figure 3-3, for trans and cis $C_4AzoOC_6E_2$. The surface tension as a function of true concentration is plotted in Figure 3-4, together with the surface tension versus nominal, or as prepared, concentration. The area occupied per molecule at the surface is obtained simply from the inverse of this surface excess concentration as $A_s = 1/\Gamma N_A$, where N_A is Avogadro's number. Table 3-1 gives the Frumkin parameters and other relevant solution and interfacial properties for both isomers of these surfactants. These results are summarized graphically in Figure 3-6, and discussed below.

Table 3-1 Optimal model parameters

	$C_4AzoOC_2E_2$		$C_4AzoOC_4E_2$		$C_4AzoOC_6E_2$		$C_4AzoOC_8E_2$	
	Trans	Cis	Trans	Cis	Trans	Cis	Trans	Cis
$\Gamma_\infty(\mu\text{-mol/m}^2)$	8.04	8.01	8.01	5.02	8.01	5.01	4.35	5.01
h/RT	2.03	2.01	1.41	0.00	1.00	0.03	0.04	0.12
$k(\text{mol/m}^3)$	237	107	1380	555	2880	2625	271	647

Table 3-2 Photo-responsive surfactant solution properties under different illumination conditions

	$C_4AzoOC_2E_2$		$C_4AzoOC_4E_2$		$C_4AzoOC_6E_2$		$C_4AzoOC_8E_2$	
	Trans	Cis	Trans	Cis	Trans	Cis	Trans	Cis
CMC (μM)	4.09	7.98	1.59	23.8	1.01	4.51	7.20	10.80
γ_{CMC} (mN/m)	32.4	32.4	28.9	39.6	29.5	40.6	59.3	45.0
Γ_{CMC} (μ-mol/m^2)	7.89	7.83	7.78	4.67	7.63	4.64	2.92	4.39
Γ_∞ (μ-mol/m^2)	8.04	8.01	8.01	5.02	8.01	5.01	4.35	5.01
$A_{s,CMC}$ (Å^2)	20.9	21.1	21.2	35.4	21.8	34.3	56.4	37.6
h/RT	2.03	2.01	1.41	0.00	1.00	0.03	0.04	0.12
k (m^3/mol)	237	107	1380	555	2880	2625	271	647

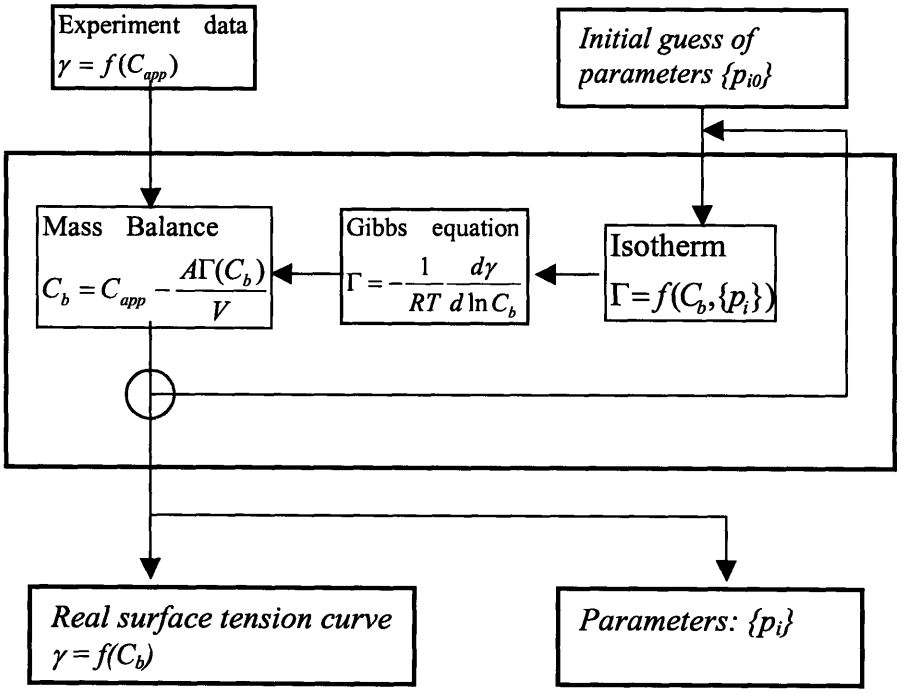

Figure 3-2 Schematic flow chart of the fitting program. The program is used to fit experimental surface tension versus nominal concentration data to obtain the optimal model parameter values.

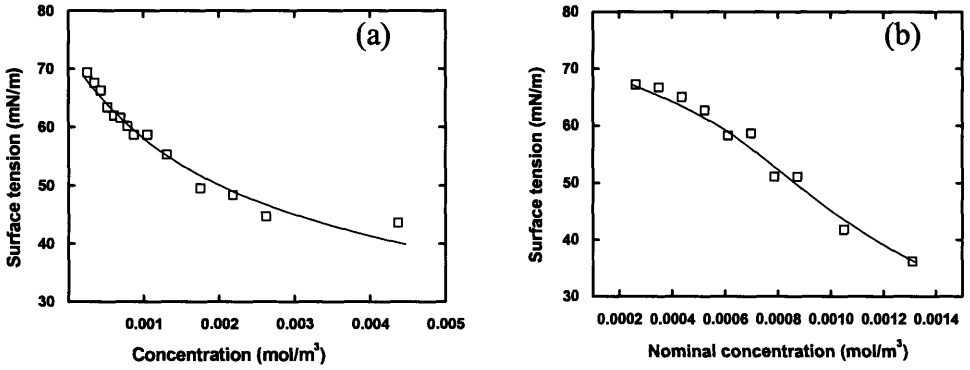

Figure 3-3 Curve fitting of surface tension vs nominal concentration data in $C_4AzoOC_6E_2$. The solid line represents the optimal fitting. (a) Trans; (b) Cis.

3.2.2 Results and Discussion

The raw results of surface tension, before and after taking the adsorption effect into account, are represented in Figure 3-4. These results are consistent with established behavior [1] in that the surface tension initially decreases with increasing concentration but then levels off and does not change with further concentration increases. The concentration at which this abrupt change in slope occurred and above which the surface tension is constant corresponds to the critical micelle concentration (CMC) [1]. The absence of any dip in the surface tension curve in this region suggests the absence of highly surface-active impurities in the solutions. $C_4AzoOC_2E_2$, $C_4AzoOC_4E_2$, and $C_4AzoOC_6E_2$ were observed to form micelles, but $C_4AzoOC_8E_2$ precipitated at high concentrations.

The different responses of the individual surfactants to changes in illumination conditions attest to the sensitivity of bulk and interfacial properties of solutions of amphiphilic compounds to small changes in surfactant structure. With only two methylene groups in the spacer, the effect of changes from the trans to the cis conformation was simply to shift the entire curve to the right; neither the shape of the surface tension curve nor the equilibrium surface tension beyond the CMC changed significantly. As the number of methylene groups increased to four and then six, however, we observed significant changes in the shapes of the curves and in the

equilibrium surface tensions. For both n = 4 and n = 6, the trans curve initially follows the curve for the cis conformation as the surfactant concentration is increased, but at some point the trans curve breaks away and the surface tension drops off more sharply until the CMC is reached. In contrast to the C_2 case, above their respective CMCs, the equilibrium surface tensions for the cis and trans forms were significantly different, with the surface tension of the trans conformation being at least 10 mN/m lower than that of the cis conformation. With a further increase in the spacer length, to eight methylene groups, the qualitative behavior of the surfactants changed dramatically as at higher concentrations the surfactant precipitated, and the surface tension curve for the trans isomer was always above that for the cis conformation.

The effect of spacer length on the CMC of the surfactants is shown in Figure 3-5 (a). For the trans form, there was a steady drop in CMC with increasing spacer length from two to six, which reflects the effect of increasing hydrophobicity of this group on the surfactant solubility within the aqueous phase. This monotonic decrease in the CMC is not seen with the cis form of the surfactant, as an increase in the spacer length from two to four methylene groups resulted in a doubling of the CMC, but a further increase in spacer length to six CH_2 groups caused a decrease in the CMC. In all three cases the CMC for the cis conformation was higher than that for the trans form of the surfactants. A similar dependence of CMC on spacer length in ionic photoresponsive surfactant systems was reported by Hayashita et al., who found that the CMC difference between trans and cis forms attained a maximum value for surfactants with moderate alkyl spacer or tail chain length [3]. These results all point to the importance of the configuration of the surfactants in determining the ease with which they can aggregate to form micelles.

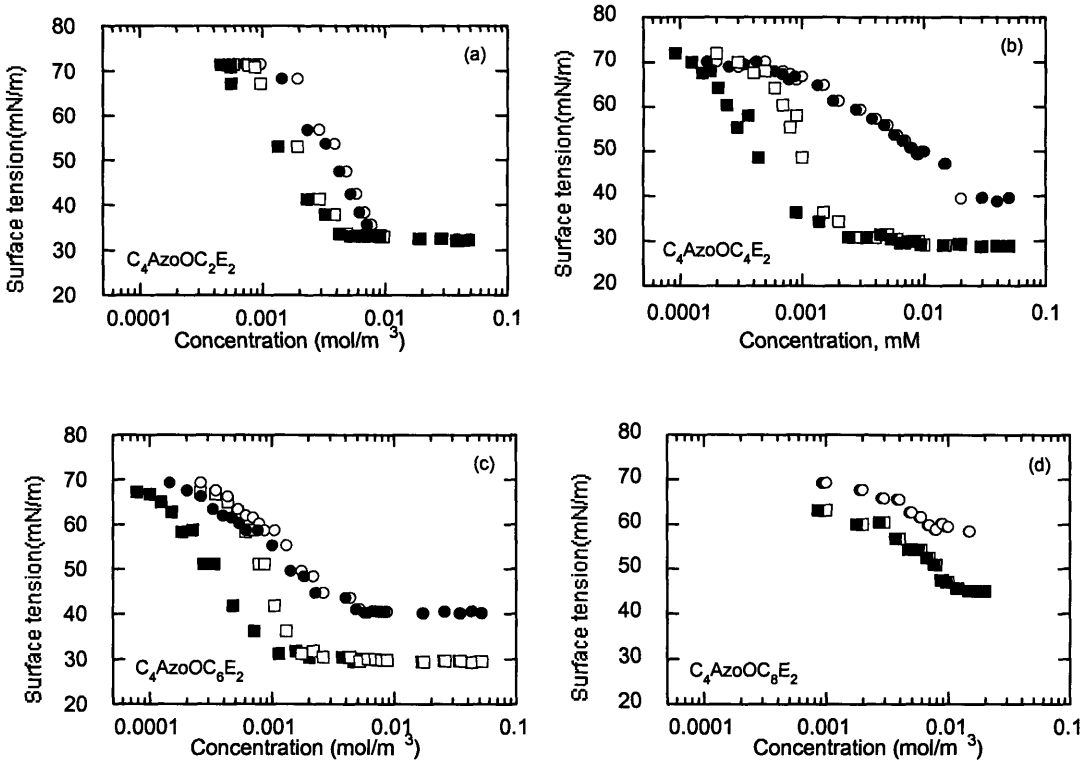

Figure 3-4 Concentration dependence of the equilibrium surface tension for photoresponsive surfactants at 25 °C under both visible (squares) and UV light (circles) illumination. The open symbols represent the original data as a function of the nominal, as-prepared concentration; the solid symbols represent data corrected for interfacial adsorption to give the true bulk concentration. (a) $C_4AzoOC_2E_2$ (b) $C_4AzoOC_4E_2$ (c)$C_4AzoOC_6E_2$ (d) $C_4AzoOC_8E_2$

The C_8 surfactant precipitated at the higher concentrations and the values reported for the CMCs actually reflect the equilibrium solubilities of the two forms of this surfactant. It is interesting to note that the C_8 surfactant has solubility limits higher than the CMCs of the less hydrophobic C_6 surfactant.

The magnitude, and even the direction, of the change in saturated surface tension with illumination wavelength depended rather dramatically on spacer length, as noted above and summarized in Figure 3-5(b). For $C_4AzoOC_2E_2$, the saturated surface tension was essentially unaffected by the wavelength of illumination, although significant surface

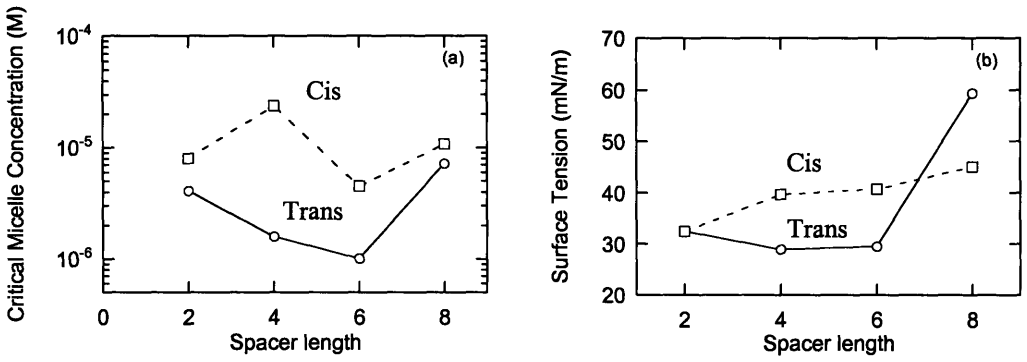

Figure 3-5 The variation of properties of photo-responsive surfactants with spacer length. (a) Critical micelle concentration; (b) Saturated surface tension

tension differences did occur at lower concentrations. In contrast, $C_4AzoOC_4E_2$ and $C_4AzoOC_6E_2$ showed differences between saturated surface tensions as large as 10.4 mN/m ($C_4AzoOC_4E_2$) and 11.0 mN/m ($C_4AzoOC_6E_2$) (The largest surface tension differences were found below the CMC, at 28.6 mN/m for $C_4AzoOC_4E_2$ and 19.1 mN/m for $C_4AzoOC_6E_2$.) $C_4AzoOC_8E_2$ showed a reverse trend in surface tension response to illumination in that, after UV illumination, its surface tension decreased rather than increased, in contrast to the behavior observed with the other three surfactants. The difference between the saturated surface tensions was 14.4 mN/m. Clearly, slight variations in molecular structure have very large effects on solute physical properties.

The values for the surface excess concentrations and for the areas occupied per molecule are shown in Figures 3-6(a) and (b), respectively. The surface excess concentrations reported using filled symbols in Figure 3-6(a) are at the respective CMCs of the surfactants (solubility limit for $C_4AzoOC_8E_2$), while open symbols denote the limiting values for Γ_∞ obtained from the Frumkin model, which would be the excess concentrations at high bulk concentrations if micelles did not form or precipitation did not occur. The molecular areas at the CMC (or at the solubility limit) are given in Figure 3-6(b). The calculated areas for the two isomers of the C_2 surfactant and for the trans forms of the C_4 and C_6 surfactants are almost constant at about 21 $Å^2$/molecule, similar to those reported for simple alkyl fatty acids (~18-24 $Å^2$/molecule) [4]. The near constancy of

the molecular areas for these four cases suggests that they have similar packing properties within the interface, as will be discussed later.

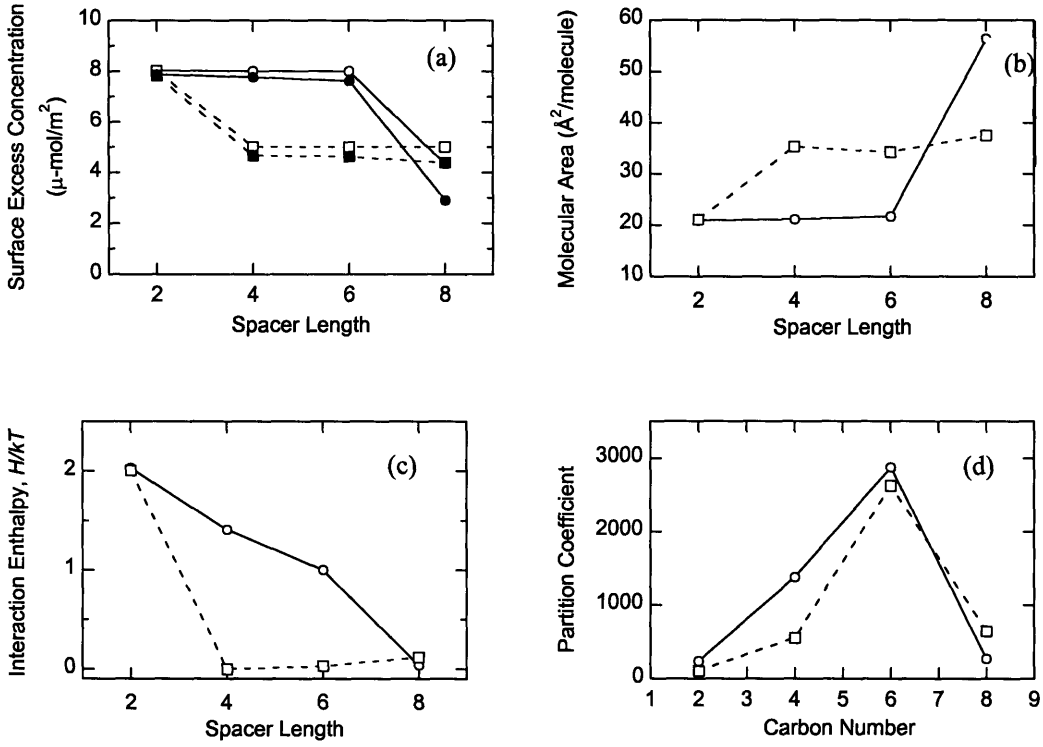

Figure 3-6 The variation of photo-responsive surfactant solution properties with spacer length. Circles represent properties under visible illumination (trans isomer); squares represent cis isomer properties, under UV irradiation. (a) Surface excess concentrations, Γ_{CMC} (solid symbols) and Γ_{∞}(open symbols); (b) Molecular areas at the CMCs; $A_{s,,CMC}$; (c) Interaction enthalpies, h/RT; (d) Adsorption coefficients, k.

The behavior noted for the surface tensions of the cis forms of the C_4 and C_6 surfactants, and for both the cis and trans forms of the C_8 surfactant, is different from the behavior discussed above. In all three cases, the cis conformations have similar surface excess concentrations with surface areas per molecule of approximately 34 to 37 $Å^2$, while the trans form of the C_8 surfactant has a lower surface excess and larger molecular area (~55 $Å^2$) than the cis form of this surfactant. Based on these observations, we conclude that the cis forms of the C_4, C_6 and C_8 surfactants have similar conformations at the interface, while the trans C_8 surfactant adopts an interfacial conformation that is

different from those of all the other cases considered here. We develop below a simple physical picture of the molecular configurations for these different cases that provides a consistent interpretation of all the experimental observations, and suggests some underlying principles for the design of surfactants with large photo-responsive characteristics.

Additional insight into the behavior of these surfactants at the interface can be gleaned from the trends shown for the interaction enthalpies and adsorption coefficients for the surfactants under different illumination conditions. As shown in Figure 3-6(c), under those conditions where the surface excess concentration is high, or the molecular area is about 21 $Å^2$, there is a significant interaction enthalpy, which decreases as the spacer length increases, while for lower surface excess concentrations there appears to be little if any interaction enthalpy in the adsorbed surfactant layer. This information is used below to reinforce a molecular interpretation of the structure of the adsorbed surfactant layer at the interface.

The adsorption coefficient, k ($= \frac{\Gamma/\Gamma_\infty}{C_b}$ *for* $\Gamma \rightarrow 0$), in Figure 3-6(d) increases with increasing spacer length from C_2 through C_6, reflecting the increasing hydrophobicity of the spacer. Lower values were obtained for k for the cis forms of the surfactant because of the more nature form of the azobenzene group in this configuration. The low value for the adsorption coefficient of the C_8 surfactant is anomalous, again consistent with the other properties exhibited by this surfactant.

The surface excess concentrations and interfacial molecular areas discussed above reflect the behavior of the surfactants at their respective CMCs. The variations in these surface properties at lower bulk concentrations are also of interest, and we show the molecular area normalized with respect to the area at the CMC, $A_s/A_{s,CMC} = \Gamma_{CMC}/\Gamma$, as a function of the normalized surface pressure π/π_{CMC}, where $\pi = \gamma_0 - \gamma = 72.0 - \gamma$ mN/m, in Figure 3-7. For any given bulk concentration, the Frumkin isotherm, Equation 3-2 was used to determine Γ, and Γ_{CMC}/Γ was plotted against the normalized experimental value for the surface pressure obtained for that bulk concentration (symbols), or against the

theoretical value for the surface pressure at that surface excess concentration obtained using Equation 3-4, shown using lines. The agreement between the experimental points and the theoretical results is an indication of the good quality of the fits of the model to

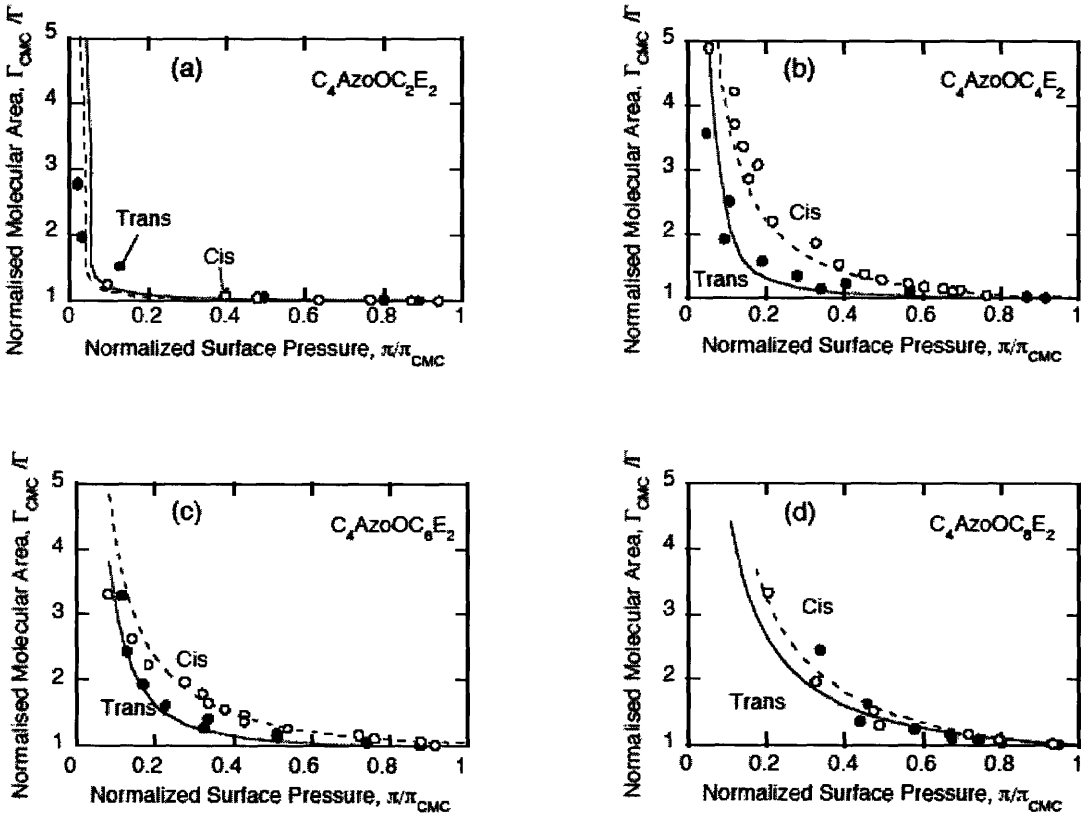

Figure 3-7 Effect of surface pressure, π, on molecular areas, $A_s=1/N_A\Gamma$, both normalized with respect to their values at the CMCs, for the trans (solid symbols) and cis (open symbols) isomers. The lines (solid for trans, broken for cis) represent the theoretically evaluated surface pressures calculated using the Frumkin parameters extracted from the experimental surface tension results. (a) $C_4AzoOC_2E_2$ (b) $C_4AzoOC_4E_2$ (c) $C_4AzoOC_6E_2$ (d) $C_4AzoOC_8E_2$

the experimental surface tension data. For both the cis and trans forms of the C_2 surfactant, and for the trans forms of the C_4 and C_6 surfactants, the molecular areas were approximately constant despite significant changes in surface tension or surface pressure.

This behavior is consistent with the presence of a nearly incompressible layer in which there is very little change in surface coverage over these surface pressure ranges. For the cis forms of the C_4 and C_6 surfactants and for both isomers of the C_8 amphiphile, the molecular area varies quite strongly with surface pressure, even close to the CMC. Such layers are considered to be compressible. The degree of compressibility of the adsorbed surfactant layers correlates directly with the interaction enthalpies for the surfactants, as the more incompressible the layer (i.e., the wider the range of surface pressures over which the area is close to that at the CMC), the larger the value of the interaction enthalpy. This behavior is consistent with there being a tightly packed interface stabilized by $\pi - \pi$ interactions between the azo-benzene groups. Completely compressible layers behave essentially ideally over the entire surface pressure range, suggesting that such $\pi - \pi$ interactions are not present in these adsorbed surfactant layers. This information is used in the discussions that follow.

3.2.3 Contact Angle Measurement

The change in surface tension, γ, upon changing illumination conditions is reflected in changes in the contact angle, θ, of a droplet of the solution on a hydrophobic surface according to the Young Equation

$$\gamma \cos\theta = \gamma_{SV} - \gamma_{SL} \tag{3-5}$$

where γ_{SV} and γ_{SL} are the surface energies at the solid-vapor and solid-liquid interfaces, respectively.

We show in Figure 3-8(a) photographs of a droplet of 0.08 mM $C_4AzoOC_6E_2$ solution on a hydrophobic glass surface coated with octadecyl trichlorosilane (OTS) with the surfactants in both the trans and the cis configurations. The contact angle for pure water on this surface was about 105°. The surfactant drop was equilibrated for 10 minutes under ambient light and its equilibrium contact angle was determined using a goniometer to be 35.8°. Following this equilibration, the system was covered by an optical curtain to prevent further exposure to ambient visible light, and the liquid drop was irradiated with UV light using a pen lamp. Within 3 minutes, the contact angle had increased

significantly and finally reached its equilibrium value of 53.5° after about 4 minutes. The contact angle variation with changing light conditions was shown to be reversible by subsequently illuminating the drop with visible light provided by a flashlight coupled with a long pass 400 nm filter. Within 3 minutes, the contact angle decreased significantly, and the previous equilibrium value of 35.8° was recovered after 5 minutes. The time-course of the contact angle variation upon changing illumination is shown in Figure 3-8(b). There was an initial lag of approximately 40 s before significant changes in contact angle were evident, following which the variation with time followed a typical exponential approach to equilibrium indicative of a first order process.

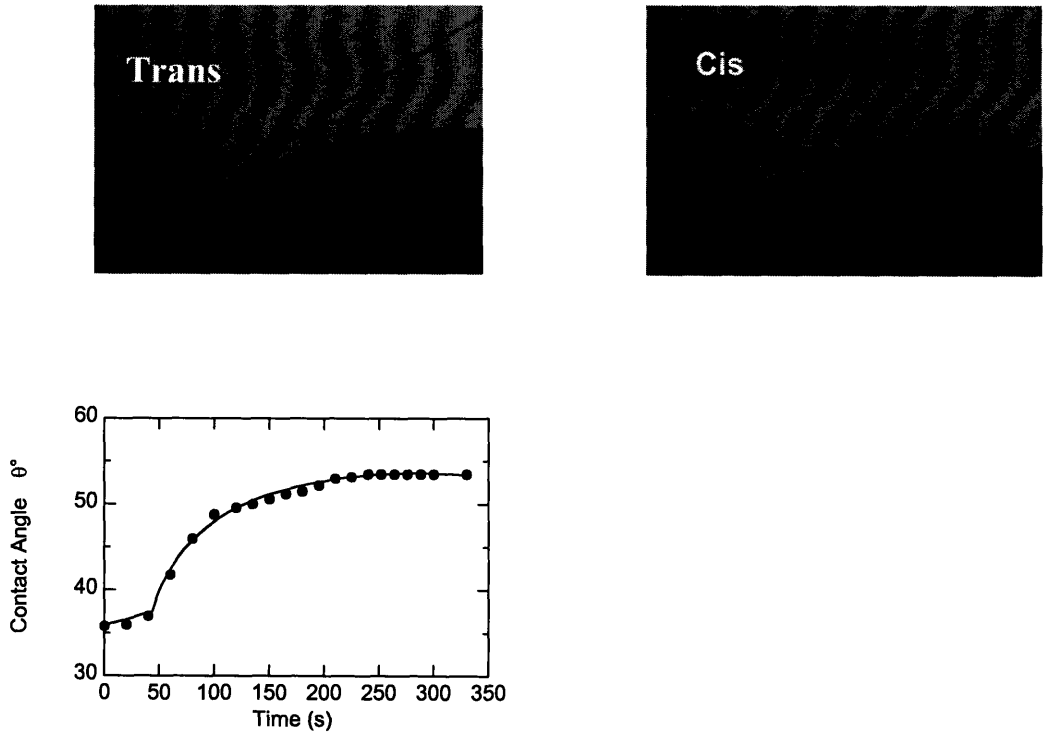

Figure 3-8. Contact angle changes for droplets of $C_4AzoOC_6E_2$ solutions (0.07 mM) on a hyrophobized surface under different illumination conditions (visible illumination for the trans isomer, UV illumination for the cis isomer). The time-course of contact angle variation under UV illumination is shown.

With these results, we established that the ratio

$$\frac{(\gamma\cos\theta)_{trans}}{(\gamma\cos\theta)_{cis}} = \frac{(\gamma_{SV}-\gamma_{SL})_{trans}}{(\gamma_{SV}-\gamma_{SL})_{cis}} = 1.12 \qquad (3\text{-}5)$$

deviates from the expected value of unity, which we attribute to changes in the solid liquid surface energy owing to changes in the properties of the adsorbed surfactant on the solid under different illumination conditions.

3.3 Molecular Mechanism for Surface Tension Response to Radiation in Photoresponsive Surfactants

As shown in the section 3.2, the response of saturated surface tension to different illumination conditions is very sensitive to the surfactant molecular structures, as reflected in the spacer length. For the purpose of designing new surfactants for even more effective performance in surface tension control, a deeper understanding of the relationship between surfactant molecular structure and the saturated surface tension is necessary. In this section, we present a molecular thermodynamic analysis of the structure-performance relationship of our new surfactants. A detailed molecular mechanism consistent with the observed surface tension response is proposed based on an elucidation of the various interactions between surfactants, and between surfactant and water.

3.3.1 Molecular Thermodynamic Analysis of Surface Tension above CMC

As we stressed in Chapter 1, for practical applications, a significant and reversible change in saturated surface tension is preferred. The dependence of surface tension on surfactant molecular structure has been investigated by several groups, mainly through

experiments. It has been found that structural changes in the tail have little effect on saturated surface tension [5]. On the other hand, from studies on azobenzene-containing photoresponsive surfactants, it was discovered that a large change in surface tension is easy to achieve when concentrations are below the CMC because differences in hydrophobicities of the two photo-isomers affect the surface adsorption processes; however, it is difficult to attain a large change in saturated surface tension, which is surface tension for concentrations above the CMC.

The limited effect of tail structure on saturated surface tension can be qualitatively understood, as follows. The surface tension is proportional to the adsorption of surfactant at the interface; the more adsorbed surfactants, the lower the surface tension. The hydrophobicity effect is the driving force for surfactant adsorption. Increases in the hydrophobicity of surfactants, such as lengthening of the tail length, will no doubt facilitate the adsorption of surfactant at the interface, and therefore lower the surface tension. This is true when the surfactant concentration is below the CMC. However, for saturated surface tensions, the effect of increasing hydrophobicity is largely canceled by the decrease in CMC, which is the upper concentration limit of free monomer in the surfactant solutions (it is well established that the CMC decreases with the hydrophobicity of the surfactant). The amount of surfactant adsorbed at the interface is proportional to the free monomer concentration. As a result of this constanct in monomer concentration, the variation of surfactant adsorption is negligible when the concentration is above the CMC, and therefore saturated surface tension changes very little. Although the above qualitative argument can explain observed experimental phenomena, a deeper analysis is required for finding the quantitative connection between surfactant molecular structure and saturated surface tension.

Self-assembly of a surfactant as well as its adsorption at an air-liquid interface, is driven by the hydrophobic effect. In principle, the molecular thermodynamic theory of micellar self-assembly is also applicable to the adsorption processes. Here, by applying molecular thermodynamic theory, we calculate surfactant adsorption at the air-liquid interface at the CMC, which is essentially the same as that for all concentrations above CMC. Because there exists a certain relationship between surface tension and surfactant

adsorption, as can be seen from, for example, the Gibbs equation, the saturated surface tension can be inferred from the degree of surfactant adsorption.

In general, the interface can be viewed as a special phase distinguished from the bulk phase. The partition coefficient of surfactant between the bulk and interface phases can be evaluated from the difference in the standard chemical potentials,

$$\frac{x_s}{x_b} = \exp\left(-\frac{\mu_{1,s}^0 - \mu_{1,b}^0}{RT}\right) \tag{3-6}$$

where x_s is the mole fraction of surfactant in the interfacial phase and x_b is the mole fraction of surfactant monomer in the bulk phase; ${\mu_{1,s}}^0$ and ${\mu_{1,b}}^0$ are the standard chemical potentials of the surfactant in the interfacial and bulk phases, respectively.

If micelles appear in the solution, the monomer concentration is essentially fixed at the CMC, which can be expressed by[6]

$$x_{b,CMC} = e^{\frac{(\tilde{\mu}_m^0 - \mu_{1,b}^0)}{RT}} \tag{3-7}$$

where $\tilde{\mu}_m^0$ is the average standard chemical potential of surfactant in micelles.

Equations (3-6) and (3-7) combine to yield

$$x_s = e^{-\frac{(\mu_{1,s}^0 - \tilde{\mu}_m^0)}{RT}} \tag{3-8}$$

Because of the similarity between surfactant packing in micelles and at the interface, the molecular thermodynamic theory developed for micellization can be applied to surfactant adsorption without significant modification.

According to molecular thermodynamic theory [6], the free energy of micellization g_{mic} ($=\tilde{\mu}_m^0$) of nonionic surfactants can be expressed as the sum

$$g_{mic} = g_{w/hc} + g_\sigma^t + g_{hc/mic} - g_\sigma^h + g_{st} \tag{3-9}$$

where $g_{w/hc}$ is the free energy to transfer the tail from an aqueous to a hydrocarbon environment[6],

$$g_{w/hc} = h_{w/hc} - Ts_{w/hc} \tag{3-10}$$

in which $h_{w/hc}$ and $s_{w/hc}$ depend only upon the chemical composition of the tail, and $g_\sigma = g_\sigma^t - g_\sigma^h$ is the total interfacial free energy contribution per monomer, in which g_σ^t is the interfacial free energy of the tail; g_σ^h is the reduction of interfacial free energy because of the presence of the head group. The value of g_σ depends on the curvature of the interface [6],

$$g_\sigma = \sigma(a - a_0) \tag{3-11}$$

where σ is the interfacial free energy per unit area; $a = Sv/l_c$ is the interfacial area per monomer; and a_0 is the area of the chemical bond connecting the head and tail group. The curvature dependency of σ can be captured by the equation [6],

$$\sigma = \sigma_0[1-(S-1)\frac{\delta}{l_c}] \tag{3-12}$$

where σ_0 is the interfacial free energy of a planar hydrocarbon-water interface.

The steric contribution to the free energy is [6],

$$g_{st} = -kT\ln\left(1-\frac{a_h}{a}\right) \tag{3-13}$$

in which a_h is the average cross-sectional area of the head.

The free energy loss associated with anchoring the tail at the interface $g_{hc/mic}$, which includes also the interactions between tails, can be estimated numerically from the single-chain mean-field model. This energy loss also depends on the shape of the micelles.

The adsorption free energy g_{ads} ($\mu_{l,s}^{0}$) can be evaluated by a similar procedure and formulation. Terms in g_{ads} are similar to those in g_{mic}, the only difference being the curvature, the surfactant adsorbed layer is essentially planar. However, at concentrations just above the CMC, micelles are basically spherical and have a curved water-hydrocarbon interface. Thus, in $g_{ads} - g_{mic}$, only terms depending on curvature are retained, i.e.,

$$g_{ads} - g_{mic} = \Delta g_{\sigma} + \Delta g_{st} + \Delta g_{hc/mic} \tag{3-14}$$

The first two terms on the right hand side of (3-14) can be calculated in a straightforward manner using

$$\Delta g_{\sigma} = \frac{2\sigma_0}{l_c}(-v + \frac{3\delta v}{l_c} - \delta a_0) \tag{3-15}$$

and

$$\Delta g_{st} = (-kT)\ln(\frac{1-\frac{l_c a_h}{v}}{1-\frac{l_c a_h}{3v}}) \tag{3-16}$$

In evaluating g_{ads}, complicated interactions and conformations must usually be accounted for. It is difficult to assess its curvature dependence analytically. However, from numerical simulations, it can be inferred that the anchoring energy indeed depends on the interfacial curvature, and that the variations between different interfacial curvatures are very small, and usually less than 0.5 $k_B T$ [6]. This curvature insensitivity can be attributed to the flexibility of surfactant tail. The available area per molecule at the interface usually decreases with an increase in interfacial curvature. The decrease in available area can lead to an increase in the interaction energy, and simultaneously, a decrease in conformational entropy. Therefore, the total free energy increases. When the tail is highly flexible, it can always take on alternative conformations in response to the decrease in available area, in which the energetic interactions are avoided as much as possible. Therefore, the interactions do not increase significantly unless the available area

is small enough to be comparable with the "hard sphere" area of the surfactant. On the other hand, anchoring at the interface exerts a stringent restriction on the surfactant, in the guise of a significant decrease in conformational entropy. In comparison with the restriction from anchoring, the effect on entropy from the decrease in available area is rather small, although not negligible. Therefore, the change in conformational entropy is very small during the variation of available area. As the result, the anchoring free energy changes little when the interfacial curvature changes. It can be neglected in comparison with other terms.

From above analysis, $g_{ads} - g_{mic}$ can be represented by

$$g_{ads} - g_{mic} = \frac{2\sigma_0}{l_c}(-v + \frac{3\delta v}{l_c} - \delta a_0) - kT \ln(\frac{1 - \frac{l_c a_h}{v}}{1 - \frac{l_c a_h}{3v}}) \qquad (3\text{-}17)$$

Equation (3-17) correlates the adsorption and micellization free energy differences with various molecular structural parameters, such as molecular length l_c, molecular volume v, the average head group area a_h, and the Tolman distance δ.

The Tolman distance can be estimated approximately by scaling with the liquid molecular radius. Since hydrocarbon molecules adopt an extended conformation in bulk hydrocarbon, the Tolman distance can be calculated by scaling with the molecular fully extended length [6],

$$\frac{\delta(n)}{\delta(11)} = \frac{l_{\max}(n)}{l_{\max}(11)} \qquad (3\text{-}18)$$

in which δ(11) is fixed and given the value 2.25 Å.

Equation (3-18) implies that δ/l_c is roughly constant for various molecules. Taking this into consideration, (3-17) can be further simplified to give,

$$g_{ads} - g_{mic} \approx \eta \frac{2\sigma_0 v}{l_c} - kT \ln\left(\frac{v - l_c a_h}{3v - l_c a_h}\right) \qquad (3\text{-}19)$$

where η is positive constant.

In an homogeneous surfactant series, v/l_c is almost constant. Furthermore, the variation in v/l_c between various surfactants is small, as indicated by the fact that almost every surfactant tail has a well-defined geometry and close cross sectional area. Therefore, v/l_c can be viewed roughly as a constant. One direct conclusion from this analysis is that simply lengthening the surfactant tail has little effect on adsorption, and therefore on surface tension itself, consistent with experimental results. It was found a long time ago that although a longer surfactant tail can make the CMC decrease significantly, the saturated surface tension changes very little. The reason for this observation is clear from the above analysis.

From equation (3-16), it can be inferred that surfactant adsorption depends solely on a single dimensionless structure parameter $\frac{l_c a_h}{v}$, which we call the adsorption parameter N_{ads}. This parameter, which contains the molecular structural parameters of both head and tail groups, summarizes the effect of surfactant architecture on surfactant adsorption. The free energy difference $g_{ads} - g_{mic}$ is plotted against the adsorption parameter N_{ads} in Figure 3-9.

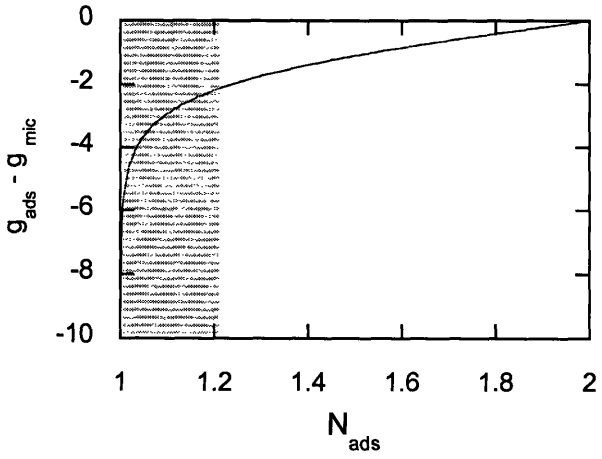

Figure 3-9 The dependence of free energy difference $g_{ads} - g_{mic}$ on adsorption parameter N_{ads}. The shaded region designates the tail dominant conformations.

It can be seen that the free energy difference changes slowly whenever N_{ads} is larger than 1.2, but that it varies drastically for N_{ads} smaller than 0.8. From simple geometrical analysis, the average area of the surfactant at the interface is determined by either the tail or by the head (Figure 3-10). In the case of tail domination, the interfacial molecular conformation is determined to a large extent by the tail, and the average area is close to the cross sectional area of tail a_t. Similarly, in the case of head domination, the head plays the primary role in determining the surfactant interfacial conformation, and

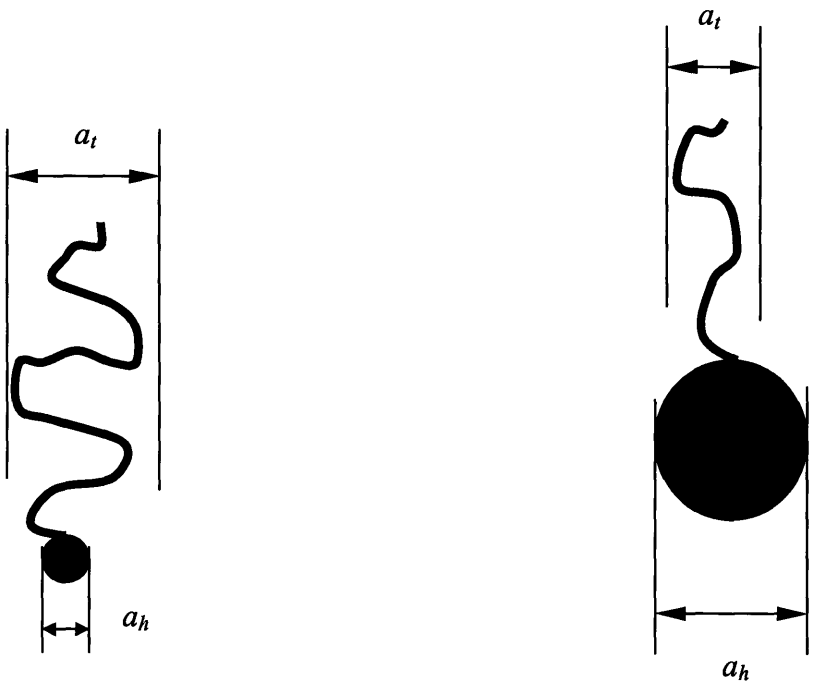

Figure 3-10 Surfactant conformation at the interface. (a) Tail dominates (b) Head dominates

correspondingly, the average area is completely determined by the cross sectional area a_h. The adsorption parameter N_{ads} is close to 1 when the surfactant conformation is tail dependent at the interface; whereas N_{ads} is much larger than 1 when the head dominates the surfactant conformation. As a consequence, it is clear that adsorption is small when the surfactant conformation is dominated by the head, and becomes large when the surfactant interfacial conformation is tail controlled.

From the above molecular thermodynamic analysis, it can be concluded that the most effective method to control surface tension is to switch the surfactant conformation between two totally distinct conformation types, that is, between the head dominated and the tail dominated conformations. As illustrated in Figure 3-9, the relevant adsorption free energy $g_{ads} - g_{mic}$ in these two conformations is very different, and ensures the surfactant adsorption in these two conformations differs significantly from each other, and therefore so do their saturated surface tensions.

We can analyze the surface tension response in our photoresponsive surfactants based on the above analysis. Essentially, the trans-cis conformation change in the azobenzene group only affects the tail conformation. Without the involvement of the head group, it is difficult to "push" the surfactant into the head dominant conformation by the photoisomerization of azobenzene. It is concluded that the photoresponsive surfactant is still in a tail dominant conformation even when the azobenzene changes to the cis conformation. The saturated surface tensions of trans and cis are essentially the same. This is supported by the lack of a saturated surface tension change with C_2 surfactants. However, it is contradicted by the surface tension response of C_4, C_6 and C_8 surfactants. According to our theory, the large change of saturated surface tension in cis form strongly indicates the appearance of the head dominant conformation. In the next section, we will propose a molecular mechanism to explain the large change of saturated surface tension in C_4, C_6 and C_8, in which the appearance of head dominant conformation will become clear.

3.3.2 Molecular Configuration of Trans and Cis in the Adsorbed Layer

The changes in the physical properties discussed above can be ascribed to the orientation and conformation of the surfactants at the air-liquid interface, which are the result of complex interactions between the head and tail groups, both with each other and with the water sub-phase. It is well understood that the head groups are generally buried within this sub-phase, while the hydrophobic tail groups either lie within the plane of the interface (under very dilute conditions where surface coverage is low) or are oriented away from the water interface at high surfactant activities and surface packings, as

indicated in Figure 3-11. The insertion of polar groups such as ethylenic unsaturation, ethers, esters, amide linkages, and hydroxyls somewhere within the tail can lead to changes in the surfactant conformation, however, because of the preferred interactions of these middle polar groups with the water at the interface [7]. These interactions can lead to conformations of the type shown schematically in Figure 3-10, in which the

spacer between the polar head and the intermediate polar group forms a loop anchored at both ends in the interfacial plane, or lies within the interface as sketched in Figure 3-11. The resulting reduced surface coverage density by the surfactant has been cited as the probable cause of significant decreases in surfactant efficiency and effectiveness observed experimentally with such surfactant systems [7]. These decreases are generally more pronounced the longer the spacer between the middle polar group and the head group, and we suggest here that this is one of the primary reasons for the changes observed with our $C_4AzoOC_nE_2$ surfactants as spacer length n increases.

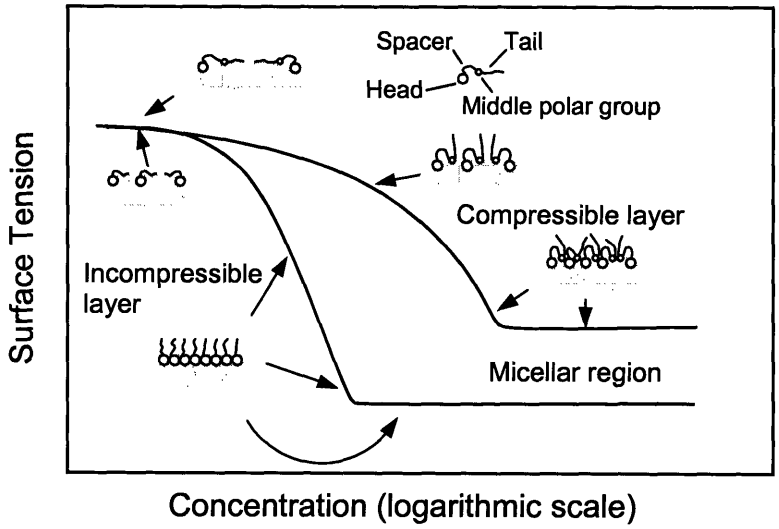

Figure 3-11 Schematic representation of conformations of adsorbed surfactants at different bulk concentrations showing the effect of an intermediate polar group on the surface tension. The upper curve shows that the conformation induced by this polar group leads to a more compressible layer with reduced surface excess concentrations and a lowering of the surface tension reduction efficiency relative to the case when there is no middle polar group.

The interfacial configurations of the surfactants developed in this work are also mediated by the conformational states of the azobenzene groups themselves, and their interactions with the polar interface, since the localization of the middle polar group at the interface would necessarily cause the azobenzene group to lie in, or be in close proximity and at some angle to, the interfacial plane. If these interactions are sufficiently unfavorable then they will negate the advantages gained by localizing the intermediate polar group at the interface, hence inhibiting formation of the loop, and the preferred configuration would be to have both the spacer and polar group oriented away from the interface. The cis form of the azobenzene group has a folded state with a high dipole moment of 3.1Debye, while the trans state is planar and has a significantly lower dipole moment of 0.5 Debye (Figure 3-12). The cis form, in allowing one of the benzene rings to bend away from the interface, reduces unfavorable hydrophobic interactions with the sub-phase relative to those that would be in effect for the planar trans form with a larger exposed area. Moreover, the significant dipole moment of the cis conformation of the azobenzene group allows for favorable interactions with the interface; whereas, for the trans conformation, such strong dipole interactions will not be evident. It is the balance between these different energetic contributions that determines the ultimate conformation at the interface. In Figure 3-13 we show schematically, based on these arguments, the probable conformations taken on by the four surfactants under different illumination conditions.

The C_2 spacer and the ether oxygen combined constitute a third ethylene oxide moiety, forming a large polar E_3 head group (as opposed to the E_2 head group of the other surfactants) and thus this surfactant has the more conventional structure of a single polar head group attached to a hydrophobic tail moiety, and both the trans and cis conformations extend away from the interface and have similar surface excess concentrations. The surface areas per molecule of about 21 $Å^2$ for the two forms of this surfactant show that both conformations are tightly packed within the interface, as illustrated schematically in Figure 3-13(a). The molecular structures were obtained using the energy minimization routine in ChemDraw, and do not take into consideration interactions with the water subphase or interactions other than steric exclusion between the molecules.

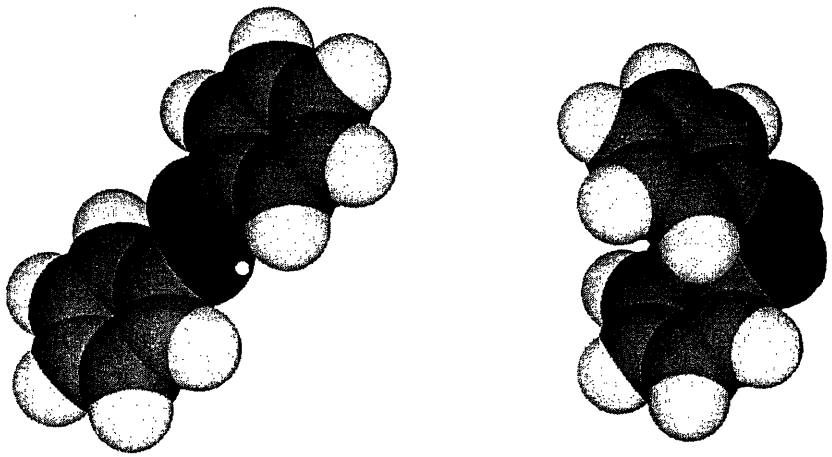

Trans **Cis**

Figure 3-12 Photo-isomerization of azobenzene. The 3D structures show the planar trans and bent cis isomers

The C_4 and C_6 spacers, in contrast, are sufficiently long that they are capable of forming loops if energy considerations favor this configuration. The trans surfactant appears to adopt an orientation normal to the interface, however, probably stabilized by π-π interactions[8], as shown in Figure 3-13(b). This assertion is supported by the observation that the trans forms of the C_4 and C_6 surfactants have surface excess concentrations and surface areas per molecule similar to those of the C_2 surfactants. Moreover, the interaction enthalpies for these cases are high, indicating that such interactions must be occurring between the surfactants within the adsorbed layer. As the spacer length increases, the interactions are reduced (see Figure 3-6(d)) owing to a greater degree of configurational freedom with longer alkyl chains.

The reduction in the stabilizing π-π interactions when the azobenzene group adopts the cis conformation, on the other hand, coupled with its strong dipole moment, favors a configuration where the azobenzene group is partially in the interfacial plane, as shown in the second of the surfactant orientations in Figure 3-13(b). The areas occupied per molecule for these surfactants in the cis state (~36 $Å^2$) are higher by about 15 $Å^2$ than those for the C_2 surfactant, a difference that is consistent with the molecular models of

the surfactants. This loss of interactions owing to looser packing of molecules in the interface is reflected in the lack of interaction enthalpies for these surfactants in these configurations.

Finally, for the C_8 surfactant, the spacer is sufficiently long that it can adopt a loop configuration with a greater number of degrees of freedom, relieving some of the entropic penalty associated with the anchoring of both ends of the spacer at the interface and avoiding unfavorable hydrophobic interactions between the spacer methylene groups and water, even as it allows for the azobenzene group to lie within the interfacial zone. Under these circumstances, even the trans form of the azobenzene group may be favored thermodynamically to lie in the interface, as shown in Figure 3-13(c). Consequently, the area occupied by the trans form of the surfactant would be expected to be larger than that of the cis form, as indeed it is. The actual increase in area is less than that inferred from the molecular model probably because, in reality, the azobenzene group does not

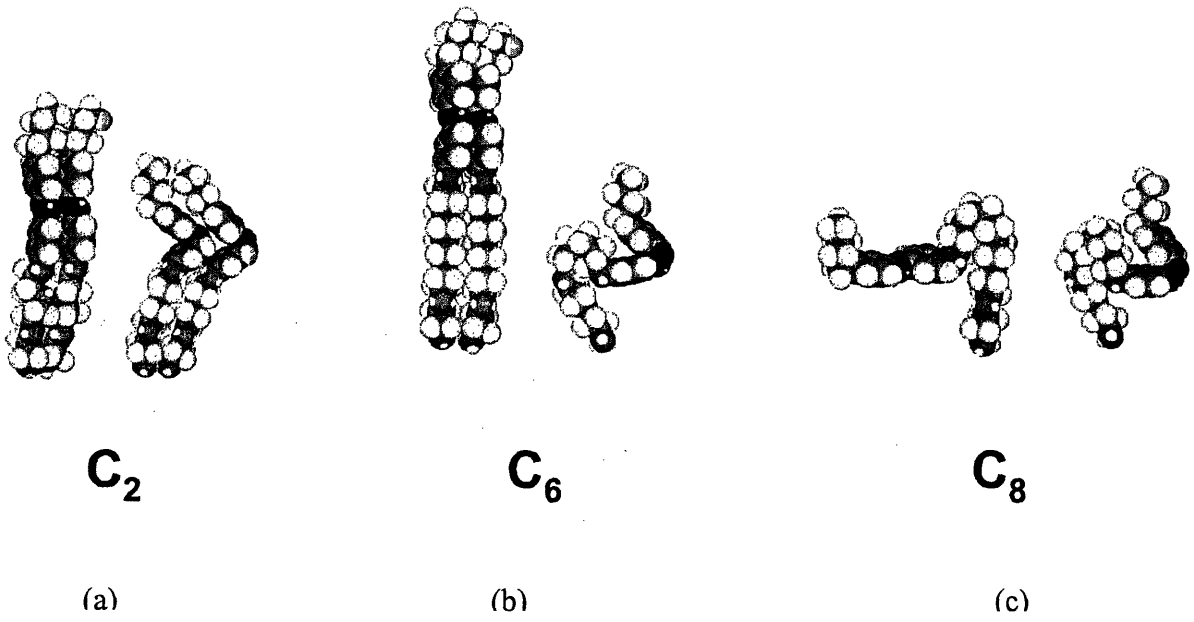

Figure 3-13 Proposed surfactant conformations in the adsorbed layer under different illumination conditions for the $C_4AzoOC_2E_2$, $C_4AzoOC_6E_2$ and $C_4AzoOC_8E_2$ surfactants. Trans is on the left and cis on the right for each surfactant isomer pair.

lie fully within the interface, but at some angle to it, or because there may some overlapping of molecules at the interface to reduce the overall effective molecular area. The surface tension of the trans form of the surfactant would in this case be higher than that of the cis form, which is again consistent with the experimentally observed trends. Note that the area per molecule and the surface tension determined experimentally for the cis form of the C_8 surfactant are very close to the values observed for the C_4 and C_6 surfactants in the same state, indicating that the configurations in the interfacial zone are similar for all three surfactants in the cis state. Again, no interaction non-idealities are observed for these cases.

The molecular analysis presented above is consistent with and supports the conclusions from the molecular thermodynamic theory. The regular conformation of surfactant at the interface is exactly the tail dominant conformation. The loop conformation, adopted by cis C_4, cis C_6, and C_8 in both trans and cis forms, corresponds to the head dominant conformation, in which the middle polar group is anchored at the interface, and together with the spacer and ethylene oxide, consists of a new huge "head group" (The cross sectional area is actually defined as a "hard disk" area at the interface. In the loop conformation, this "hard disk" area is actually determined by middle polar group and the spacer). The large difference in saturated surface tension is acquired when the surfactant switches between tail dominant (regular) and head dominant (loop) conformation.

3.3.3 Design Principle for Photoresponsive Surfactants

The above experimental results and analyses suggest that the middle polar group plays an important role in determining surfactant conformation in the adsorbed layer and hence in determining the surface tension. This realization provides insight relative to the formulation of molecular design principles for surfactants for the active photo-control of surface tension. Because of its hydrophobicity, the azobenzene group is usually incorporated into the tails of photosensitive surfactants. However, it is known experimentally that structural changes in the tail group usually exert a much smaller effect on surface tension than do changes in the head group [5], which is consistent with

reports in the literature that the photoisomerization of photosensitive ionic surfactants does not yield large changes in equilibrium surface tension, especially in the saturated surface tension region. The results reported in this paper indicate that large photo-induced surface tension changes can be achieved by the introduction of an intermediate polar group within the tail of a non-ionic surfactant, which can induce loop formation to bring the azobenzene moiety into close proximity with the interface. If the spacer length is such that loop formation is favored for one conformation (cis) but not for the other (trans) because of the different interfacial interaction energies associated with the two photoisomers, then the trans form will be oriented away from, and be more tightly packed at, the interface, and will exhibit a lower surface tension than the cis form of this surfactant. If, on the other hand, loop formation is favored for both photo-isomers, then the cis form will be more effective in lowering surface tension than will the trans form. Thus, through a coupling of photoisomerization with the effect exerted by the intermediate polar group in driving the formation of loops, the influence of photoisomerization on surface tension can be amplified.

3.4 Summary

In this chapter, the surface adsorption properties of a new class of photoresponsive surfactants were examined both experimentally and theoretically. The experimental results indicate that the response of saturated surface tensions depends strongly on the molecular structure of the surfactants, more specifically, on their spacer lengths. When the spacer length is short, such as the two methylene groups in C_2, the response of saturated surface tension to different illumination conditions is negligible. When the spacer is elongated to 4 or 6 methylene groups (C_4 or C_6), saturated surface tensions under UV light are significantly higher than under visible light. However, when the spacer is further increased to 8 methylene groups (C_8), the saturated surface tension under UV light was much lower than that under visible illumination. These experimental results show that slight variations in molecular structure can cause dramatic changes in saturated surface tensions, for instance, upon changes in illumination conditions.

Because of the similarity between self-assembly and surfactant adsorption, a model is proposed to analyze the surfactant adsorption based on the molecular thermodynamic theory of self-assembly. The molecular thermodynamic analysis indicates that, in the context of the saturated surface tension, the effect of elongating the tail length is largely balanced by the decrease in CMC, which sets the upper limit for the free monomer concentration in surfactant solutions. As a consequence, the sole structural change in the surfactant tail has little effect on saturated surface tension. Moreover, it was found that the behavior of surfactant adsorption was almost completely determined by a single dimensionless group, the adsorption number N_{ads}, which is the ratio of the product of tail length and cross sectional area of head to the volume of surfactant tail. Starting from this result, it was deduced that large changes in saturated surface tension are possible when the surfactant head involved in the conformation changes in this way, in which surfactant can switch between head dominant conformation (molecular area is determined by head group area) and tail dominant conformation (molecular area is determined by tail area).

A molecular mechanism is proposed to explain the response of the saturated surface tension to irradiation. Because of the role of the middle polar group (ether oxygen), the surfactant can potentially take on a "loop conformation" as the result of a preferred interaction between the middle polar group and water. In contrast to the normal conformation, in which the head group is buried in the water sub-phase, while the surfactant tail is oriented away from the water, in the loop conformation the spacer between the middle polar group and the head group forms a loop anchored at both ends in the interface. The formation of the loop conformation depends on various subtle factors, such as the spacer length, the polarity of head and tail constituents, and the π - π interaction between azobenzene groups. In surfactant C_2, both trans and cis forms adopt the regular conformation. In contrast, surfactants C_4 and C_6 in the trans form prefer the regular conformation because of the strong π - π interaction; while their cis forms adopt the loop conformation because of the flexibility provided by the long spacer, and the greater polarity of the bent cis isomer of the azobenzene moiety. As a result of the large difference in these conformations, the trans and cis forms have very different saturated

surface tensions. In surfactant C_8, the spacer is so long that both the trans and cis forms adopt a loop conformation, in which the azobenzene group is favored thermodynamically to lie within the interfacial zone. Consequently, the area occupied by the trans form of the surfactant would be expected to be larger than that of the cis form, as indeed it is. The surface tension of trans form in this circumstance is higher than that of cis form. These explanations are consistent with experimental observations.

The above experimental results and analyses suggest that the middle polar group plays an important role in determining surfactant conformation in the adsorbed layer and hence in determining the surface tension. This realization provides insight relative to the formulation of molecular design principles for surfactants for the active photo-control of surface tension. Because of its hydrophobicity, the azobenzene group is usually incorporated into the tails of photosensitive surfactants. However, it is known experimentally that structural changes in the tail group usually exert a much smaller effect on surface tension than do changes in the head group, which is consistent with reports in the literature that the photoisomerization of photosensitive ionic surfactants does not yield large changes in equilibrium surface tension, especially in the saturated surface tension region. The results reported in this paper indicate that large photo-induced surface tension changes can be achieved by the introduction of an intermediate polar group within the tail of a non-ionic surfactant, which can induce loop formation to bring the azobenzene moiety into close proximity with the interface. If the spacer length is such that loop formation is favored for one conformation (cis) but not for the other (trans). Then, the large surface tension change in response to different illumination conditions can be obtained. Therefore, through insertion middle polar group and careful selecting spacer length, the surfactant with the excellent photocontrolled surface tension performance can be developed from azobenzene.

The surfactant conformation and distribution of the tail moieties near the interface have been inferred based on surface tension results, but these can not give a direct picture of the adsorption layer of these surfactants. In the next chapter, we use neutron reflectivity to probe a more directly the tail group distributions normal to the interface to corroborate the surfactant interfacial configuration proposed in this chapter. Because of

the short wavelength of neutron (3~ 5 Å), the interfacial configuration of surfactants can be obtained with atomic resolution.

3.5 Appendix

Table 3-3 Raw surface tension data

$C_4AzoOC_2E_2$			$C_4AzoOC_4E_2$			$C_4AzoOC_6E_2$			$C_4AzoOC_8E_2$		
C (mM)	γ (mN/m)		C (mM)	γ (mN/m)		C (mM)	γ (mN/m)		C (mM)	γ (mN/m)	
$\times 10^3$	Trans	Cis	$\times 10^3$	Trans	Cis	$\times 10^3$	Trans	Cis	$\times 10^3$	Trans	Cis
0.582	71.4	71.6	0.2	72	70.2	0.26197	67.2	69.4	63.1	69.3	63.1
0.776	71.2	71.6	0.3	70	69.1	0.3493	66.7	67.6	59.9	67.7	59.9
0.873	70.8	71.5	0.4	67.6	69.6	0.43662	65	66.3	60.4	65.8	60.4
0.97	67.1	71.6	0.5	68.1	70.2	0.52395	62.7	63.4	56.7	65.6	56.7
1.94	53	68.3	0.6	64.2	68.1	0.61127	58.3	62	54.3	62.6	54.3
2.91	41.2	56.7	0.7	60.4	68.1	0.6986	58.7	61.6	54.2	61.6	54.2
3.88	37.8	53.6	0.8	55.4	67.4	0.78592	51.1	60.2	52.4	59.8	52.4
4.85	33.5	47.5	0.9	58	66.1	0.87325	51.1	58.7	50.9	58.9	50.9
5.82	33	42.4	1	48.6	66.9	1.05	41.8	58.7	47.5	60.1	47.5
6.79	33	38.3	1.5	36.3	64.9	1.31	36.2	55.3	47	59.4	47
7.76	33.2	35.6	2	34.3	61.4	1.75	31.2	49.6	45.6		45.6
8.73	33	35.2	3	30.8	59.4	2.18	31.7	48.4	45	58.4	45
9.7	32.9	33.3	4	30.7	57.3	2.62	30.4	44.7	45		45
19.4	32.4	32.4	5	31.4	55.9	4.37	30.4	43.6	44.9		44.9
29.1	32.4	32.5	6	30.4	53.7	5.24	29.4	41			
38.8	32	32.4	7	29.5	52.4	6.11	30	40.2			
48.5	32.1	32.4	8	29.8	50.8	6.99	29.9	40.6			
			9	29.9	49.4	7.86	29.7	40.5			
			10	29.1	50	8.73	29.7	40.5			
			15	29	47.2	17.46	29.3	40.1			
			20	29.2	39.5	26.2	29.5	40.5			
			30	28.7	39.6	34.93	29.5	40.1			
			40	28.8	38.8	43.66	29.2	40.6			
			50	28.9	39.6	52.39	29.4	40.1			

Table 3-4 Surface tension data after concentration correction

$C_4AzoOC_2E_2$				$C_4AzoOC_4E_2$				$C_4AzoOC_6E_2$				$C_4AzoOC_8E_2$			
Trans		Cis		Trans		Cis		Trans		Cis		Trans		Cis	
C (mM) $\times 10^3$	γ (mN/m)	C (mM) $\times 10^3$	γ (mN/m)	C (mM) $\times 10^3$	γ (mN/m)	C (mM) $\times 10^3$	γ (mN/m)	C (mM) $\times 10^3$	γ (mN/m)	C (mM) $\times 10^3$	γ (mN/m)	C (mM) $\times 10^3$	γ (mN/m)	C (mM) $\times 10^3$	γ (mN/m)
0.45897	71.4	0.53631	71.6	0.091792	72	0.16635	70.2	0.07887 5	67.2	0.14597	69.4	0.92968	69.3	0.85724	63.1
0.54935	71.2	0.70986	71.6	0.12578	70	0.25117	69.1	0.10116	66.7	0.20309	67.6	1.8812	67.7	1.7858	59.9
0.55414	70.8	0.79447	71.5	0.15327	67.6	0.33706	69.6	0.12471	65	0.26477	66.3	2.8475	65.8	2.7448	60.4
0.55857	67.1	0.87837	71.6	0.17764	68.1	0.42392	70.2	0.15144	62.7	0.32921	63.4	3.8207	65.6	3.7184	56.7
1.3432	53	1.4425	68.3	0.20501	64.2	0.51165	68.1	0.18388	58.3	0.39665	62	4.8016	62.6	4.6995	54.3
2.2935	41.2	2.3339	56.7	0.24256	60.4	0.60018	68.1	0.22578	58.7	0.46829	61.6	5.7851	61.6	5.6857	54.2
3.2562	37.8	3.2821	53.6	0.29499	55.4	0.69018	67.4	0.27732	51.1	0.54031	60.2	6.7723	59.8	6.6758	52.4
4.2229	33.5	4.2428	47.5	0.362	58	0.77966	66.1	0.33791	51.1	0.61429	58.7	7.7675	58.9	7.6676	50.9
5.1929	33	5.2061	42.4	0.44022	48.6	0.87001	66.9	0.4817	41.8	0.76963	58.7	8.7675	60.1	8.6612	47.5
6.1629	33	6.1721	38.3	0.89724	36.3	1.3305	64.9	0.71728	36.2	1.0063	55.3	9.7675	59.4	9.6559	47
7.1329	33.2	7.1393	35.6	1.3841	34.3	1.8004	61.4	1.1437	31.2	1.4205	49.6	14.768	58.4	11.651	45.6
8.1029	33	9.0775	33.3	2.3812	30.8	2.7585	59.4	1.5737	31.7	1.8349	48.4			14.651	45
9.0729	32.9	18.777	32.4	3.3812	30.7	3.7309	57.3	2.0137	30.4	2.2634	44.7			17.651	45
18.773	32.4	28.477	32.5	4.3812	31.4	4.7117	55.9	3.7637	30.4	3.9909	43.6			19.651	44.9
28.473	32.4	38.177	32.4	5.3812	30.4	5.6967	53.7	4.6337	29.4	4.8715	41				
38.173	32	47.877	32.4	6.3812	29.5	6.6855	52.4	5.5037	30	5.7415	40.2				
47.873	32.1			7.3812	29.8	7.6769	50.8	6.3837	29.9	6.6215	40.6				
				8.3812	29.9	8.6695	49.4	7.2537	29.7	7.4915	40.5				
				9.3812	29.1	9.6636	50	8.1237	29.7	8.3615	40.5				
				14.381	29	14.645	47.2	16.854	29.3	17.091	40.1				
				19.381	29.2	29.629	39.6	25.594	29.5	25.831	40.5				
				29.381	28.7	39.629	38.8	34.324	29.5	34.561	40.1				
				39.381	28.8	49.629	39.6	43.054	29.2	43.291	40.6				
				49.381	28.9			51.784	29.4	52.021	40.1				

3.6 Bibliography

1. Hiemenz, P. C. & Rajagopalan, R. *Principles of Colloid and Surface Chemistry* (Marcel Dekker, Inc., New York, 1997).

2. Lucassen-Reynders, E. H. in *Anionic Surfactants: Physical Chemistry of Surfactant Action* (ed. Lucassen-Reynders, E. H.) 1-54 (Marcel Dekker,Inc., New York, 1981).

3. Hayashita, T., Kurosawa, T., Miyata, T., Tanaka, K. & Igawa, M. Effect of Structural Variation within Cationic Azo-Surfactant Upon Photoresponsive Function in Aqueous-Solution. *Colloid Polym. Sci.* **272**, 1611-1619 (1994).

4. Prosser, A. J. & Franses, E. I. *Colloids Surf. A* **178**, 1-40 (2001).

5. Aratona, M. & Ikeda, N. in *Structure-Performance Relationships in Surfactants* (eds. Esumi, K. & Ueno, M.) 83-146 (Marcel Dekker,Inc., New York, 1997).

6. Puvvada, S. & Blankschtein, D. Thermodynamics Description of Micellization, Phase-behavior, and Phase-Separation of Aqueous-Solution of Surfactant Mixtures. *J.Phys.Chem.* **96**, 5567-5579 (1992).

7. Myers, D. *Surfaces, Interfaces, and Colloids* (Wiley - VCH, New York, 1999).

8. Steed, J. W. & Atwood, J. L. *Supramolecular Chemistry* (Wiley, New York:, 2000).

Chapter 4

Neutron Reflection Study on Adsorbed Photoresponsive Surfactant Layer

4.1 Introduction

The surface tension of a surfactant solution is determined by the structure of the surfactant adsorbed layer. In the previous chapter, the properties of adsorbed layers of photoresponsive surfactants were studied using the Gibbs adsorption isotherm, by which the surface excess, or equivalently, the molecular area, can be extracted from surface tension vs concentration curves. Based on the surface excesses, a qualitative picture on surfactant interfacial conformation was proposed to explain the observed surface tension changes under different illumination conditions. However, molecular areas as calculated from the Gibbs equation only provide averaged, coarse gained structural information on the adsorbed layer and cannot provide detailed information at the molecular level, such as surfactant configuration and distributions. Our proposed mechanism can be validated unambiguously only when the surfactant interfacial conformation with atomic resolution is available. Therefore, a detailed adsorbed layer structure with spatial resolution of order Angstrom is desirable.

Neutron reflection is a powerful experimental technique to probe interfacial structure with spatial resolution on the order of Angstroms[1]. In the typical neutron reflection experiment, a neutron beam is radiated onto the thin layer and reflected by the thin layer. The reflected neutrons are collected. The neutron reflected from the upper surface are interfered with those from lower surface. From this interference, the structural information of the thin layer can be acquired. Neutrons provide high spatial resolution as the result of their short wavelengths (3~ 5 Å), and because they disturb the system slightly because of their weak interaction with nuclei. This weak interaction also allows one to interpret experimental data in terms of the Fourier transform of correlation functions [2]. Normally, in neutron reflection, the one dimensional scattering length density

(SLD) profile along the normal of the interface can be determined experimentally, which, in principle, can be converted directly to the profile of chemical constituents[1]. From this distribution, the surfactant conformation can be deduced directly[3]. Contrast variation, which utilizes the sensitivity of scattering length to isotopic substitution, enhances the power and flexibility of neutron as a structural probe. The large difference between the scattering lengths of hydrogen isotopes, for which $b_H = -3.74 \times 10^{-5}$ Å and $b_D = 6.67 \times 10^{-5}$ Å, can be used to select any specific moiety in the surfactant to be highlighted by deuteration, such that only the deuterated part is visible under neutron illumination. Through selective deuteration of different moieties, a comprehensive picture of surfactant conformation can be obtained with high resolution[4]. Of course, the successful application of contrast variation techniques is based on the underlying assumption that deuteration does not change the chemistry and interaction between the atoms significantly. This assumption has been found to be true in most situations although there do exist several exceptions. In addition, through mixing D_2O and H_2O in a certain ratio, namely 8.0 % wt, the SLD of the solution can be adjusted to be zero — the same value as that of air, such that the air-water interface is invisible; such a mixture is termed "null reflecting water" (NRW)[4]. The advantage of NRW is that reflection signals arise solely from the surfactant adsorbed layer, and thus that the structure of the adsorbed layer can be further clarified without disturbances from the air-liquid interface.

Recently, with significant improvements in neutron sources and more sophisticated instrumentation, the neutron reflection (NR) technique has experienced a surge in applications probing various interfacial structures[2]. NR has been used extensively to study various surface structures ranging from liquid interfaces to solid films. Examples include the adsorbed layers of polymers and surfactants at air-liquid interfaces [5-10], solid–liquid interfaces [11], and fluid – fluid interfaces [12,13] [14]. NR has been extended to probe soft interfaces also, such as liquid crystal surfaces[15-18], microemulsion surfaces[19-21], biological membranes[22,23], and Langmuir-Blodgett films [24-28]. In particular, there have been several studies on the structure of surfactant adsorbed layers at air-water interfaces using NR. The adsorbed layer structures of nonionic surfactants[29], ionic

surfactants[30], and mixed surfactants [31] have been worked out in detail, by which a deeper understanding of surfactant interfacial conformation has been acquired and accumulated.

In addition to the localized interface structure, the extended mesoscopic interfaces can also be investigated using NR[2]. These interfaces cannot be described by a uniform thickness, but instead, are characterized by a power law decay of the order parameter, which cannot be modeled by a simple step-like index of reflection. Among them, critical adsorption at air-liquid interfaces is the magnificent example [32]. For such interfaces, the reflectivity exhibits increasingly peculiar properties: in certain cases it is discontinuous at the angle of total reflection [33-35], and in other cases it allows one to determine the power law decay of the order parameter uniquely by inverting the reflectivity data unambiguously[36].

From the above account, it can be concluded that NR is a valuable technique for probing the structure of surfactant adsorbed layers with atomic resolution. In this chapter, we describe in detail a study on the effect of photoresponsive surfactant conformation on the structure of adsorbed surfactant layers by neutron reflection. We first introduce briefly the synthesis of deuterated surfactants, followed by the experimental procedures for neutron reflectivity measurements. Then, the theoretical methods by which neutron reflectivities are analyzed are introduced, with emphasis on the segment distribution that is first proposed in this work to describe the surfactant distribution in dense adsorbed layers. Finally, the interfacial surfactant conformations under both UV and visible light are deduced based on the results of neutron reflection experiments. The resultant conformations are close to those that we proposed in Chapter 3, and support our proposed mechanisms for the surface tension response on illuminations by light of different wavelengths.

4.2 Experiments

4.2.1 Synthesis

Materials

4-butylaniline (97%), sodium carbonate (99.95%), phenol (99+ %), di(ethylene glycol) (99%), 1,6-dibromohexane (96%), bis(trimethylsiyl)trifluoro-acetamide (99+%), and sodium hydride (95%) were purchased from Aldrich (Milwaukee, WI). 4-butylaniline 2,3,5,6 - d_4, ND2 (D, 99.1%) was purchased from CDN Isotope. 1,6-dibrohexane d_{12} (D, 98%) and Phenol d_6 (D, 98%) were purchased from Cambridge Isotope. Sodium nitrite (AR grade), potassium hydroxide (AR grade), hydrochloric acid (37%), and sodium hydroxide (AR grade) were obtained from Mallinckrodt Baker (Paris, Kentucky), and tetrahydrofuran and hexane from EM Science (Gibbstown, NJ). All chemicals were used as received without further purification.

Synthesis Procedure

The protonated, azobenzene deuterated, and spacer deuterated surfactants, diethylene glycol mono(4',4-hexyloxy, butyl-azobenzene) ($C_4AzoOC_6E_2$), were synthesized by the same procedures as described in the Chapter 2. The molecular structures of all products were verified by mass spectrometry (Bruker DALTONICS APEX, 3 Tesla, FT-ICR-MS, with Electrospray Ion source), and the purities of all products were above 99.0 wt % as analyzed by gas chromatography (HP 5890) (Chapter 2).

4.2.2 Measurement of Neutron Reflectivity

Neutron reflection experiments were conducted on the NG7 reflectometer at NIST. The samples were placed in a Teflon trough and stabilized for about 60 minutes before measurements. Neutrons with fixed 4.76 Å wavelength were focused on the sample surface at some incident angle θ_i after being deflected by a pyrolytic graphite monochromator array. The reflected neutrons were captured by the detector in the specular direction after passing through an exit slit system. The reflectivities were measured at room temperature and at different incident angles, which corresponded to a

Q range from 0.05 $Å^{-1}$ to 0.2 $Å^{-1}$ ($Q = \frac{4\pi}{\lambda}\sin\theta_i$). The reflectivities from two deuterated species of $C_4AzoOC_6E_2$, azobenzene deuterated and spacer deuterated, were measured in two types of solvents, i.e., NRW and pure D2O, and under both UV and visible illuminations, respectively. The light source used to change the surfactant conformations was a 200W mercury lamp (Oriel 6283) mounted in an arc lamp housing (Oriel 66902) and powered by an arc lamp power supply (Oriel 68910). Monochromatic UV light was obtained using a 320 nm band pass filter (Oriel 59800). The reflections from trans isomers were measured in an ambient light environment. To conduct reflectivity measurement in cis systems, surfactant solutions were first illuminated by UV light for about 30 minutes, and then carefully transferred to the trough under the protection of an optical curtain. During measurements, samples were illuminated continuously by UV light through a custom made, quartz topped cover box. During the course of an experiment, the sample trough, together with the cover box and the UV lamp, were covered by the optical curtain to minimize the disturbance from visible light as much as possible. The experiment for each sample normally lasted for several hours to collect sufficient neutrons to ensure a satisfactory signal/noise ratio. The collected data were processed to extract reflectivities using software provided by NIST, .

4.3 Theory

In a typical neutron reflection experiment, the incident neutron beam impinges the interface with an incident angle, and its reflected away from the interface with reflected angle. Depending on the refractive index of the interface, the incident beam can be partially or totally reflected[37]. In the case of an interface with a uniform lateral density distribution, almost all the reflected neutrons are in the specular direction, in which the reflected angle is equal to the incident angle, as shown in Figure 4-1. However, if there exist significant lateral density correlations in the interface, some neutrons are reflected away from the interface with a reflected angle that is different from the incident angle (Figure 4-1), in what is known as non-specular reflection[37]. Normally, specular reflection probes the interfacial SLD profile along the normal direction, while non-specular reflection provides lateral structural information. Owing to the extreme low intensities of

non-specular reflection, its routine use as a tool for probing lateral variation in surface structures must await the development of reliable experimental instruments and methods. In contrast, experimental techniques for specular neutron reflection are mature, and as a result, specular neutron reflection has become an important experimental tool for investigating interfacial structurein a wide range of systems.

In this section, we introduce the theory of specular neutron reflection in the langurage of quantum mechanics, because it is the simplest way to do so. Then, the optical matrix method together with the kinematic approximation are introduced as these are the two main methods for analyzing neutron reflection data. Finally, we will present a detail analysis of segment density distributions in various adsorbed layers, which will be used in our data analysis.

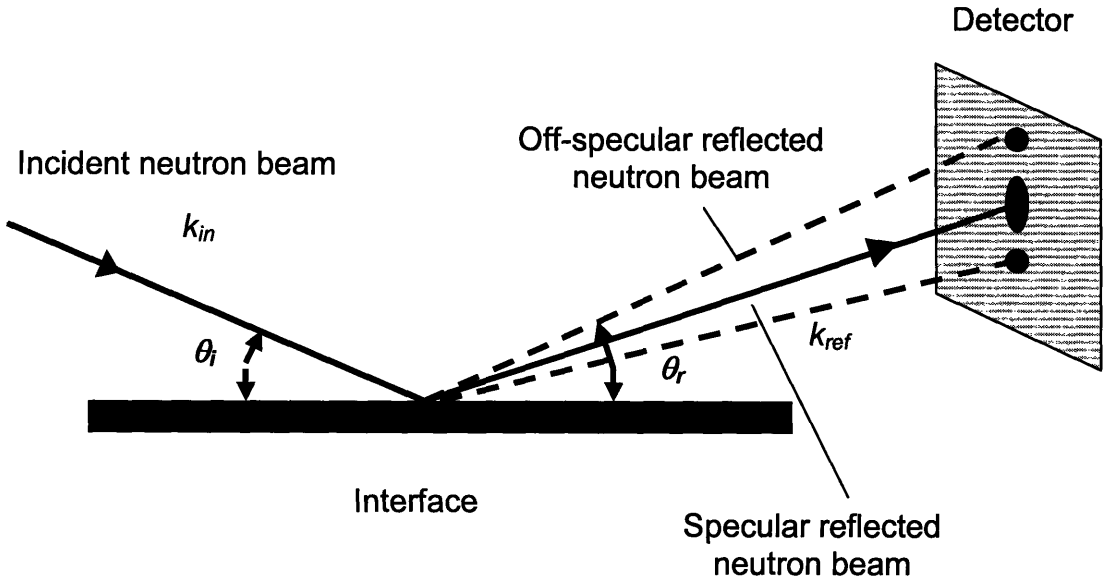

Figure 4-1 Schematic illustration of neutron reflection. θ_i is the incident angle, θ_r is the reflection angle, k_{in} is the wavevector of incident neutron beam, k_{ref} is the wavevector of reflected beam. In specular reflection, reflected angle is equal to the incident angle; while in off-specular reflection, reflected angle is not equal to incident angle.

4.3.1 Neutron Reflection

The specular reflection is actually the quantum mechanics scattering in 1-dimension. Because of the equality of the incident and reflected angles, only the normal component of the wave vector changes during reflection; the lateral wave vector remains unchanged. Therefore, only the normal direction is the analysis of specular neutron reflection. The Schrodinger equation along the normal to interface is[38],

$$-\frac{\hbar^2}{2m}\frac{d^2}{dx^2}\psi(k,z)+V(z)\psi(k,z)=E\psi(k,z)=\frac{\hbar^2k^2}{2m}\psi(k,z) \qquad (4\text{-}1)$$

in which k is the wave vector in the normal direction; which has coordinate z; $V(z)$ is the potential energy distribution in the interface, which captures the interaction of the interface with neutrons; $\psi(k,z)$ is the neutron wave function; E is the energy of the neutron, which is unchanged during elastic scattering; and m is the mass of the neutron.

The potential energy $V(z)$ is related to the SLD of the interface by[38],

$$V(z)=4\pi\rho(z) \qquad (4\text{-}2)$$

in which $\rho(z)$ is the scattering length density in the interface at position z.

Thus, the specular neutron reflection is equivalent to the scattering by the potential function $V(z)=4\pi\rho(z)$, as shown in Figure 4-2.

Equation (4-1) can be solved formally through Green's function[38],

$$\psi_{reflect}(k,z)=\frac{-i}{2k}(e^{-ikz}{}_{|z->\infty})\int_{-\infty}^{+\infty}dz'[-4\pi\rho(z')]\psi(k,z')e^{ikz'} \qquad (4\text{-}3)$$

where $\Psi_{reflect}(k,z)$ is the amplitude of the reflected wave and $\Psi(k,z)$ is the total wave function. It should be noted that although equation (4-3) is only a formal expression, it clearly reveals the relationship between the reflected and total wave functions. However,

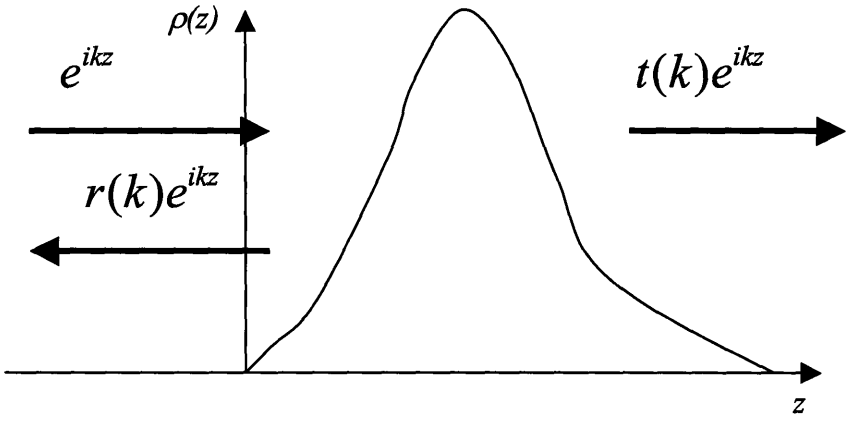

Figure 4-2 Schematic representation of specular neutron reflection with incident wave, e^{ikz}, transmission wave $t(k)e^{ikz}$, and reflected wave $r(k)e^{ikz}$.

the total wave function is involved in the integral, which is the superposition of the incident wave function with the reflected or transmitted wave function, equation (4-3) is not readily applied in the analysis of experimental data, and must be supplemented by other methods to enable data analysis to be performed effectively.

Usually, the experimental data are analyzed in terms of the reflectivity, *R*, which is defined as the intensity ratio of the reflected wave to the incident wave[38],

$$R = \frac{I_r}{I_i} = \frac{\left|\psi_{reflect}(Q)\right|^2}{\left|\psi_{in}(Q)\right|^2} \tag{4-4}$$

in which I_r is the intensity of the reflected beam, and I_i is the intensity of the incident beam. $\Psi_{reflect}(Q)$ is the amplitude of the reflected wave at infinity, and $\Psi_{in}(Q)$ is the amplitude of incident wave at infinity. $Q = 2k$ is the reflected wave vector, in which k is the normal component of the incident wave vector.

4.3.2 Optical Matrix Method

The optical matrix method is a popular approach for performing data analysis and relevant experimental fitting[39]. The basic problem addressed by the optical matrix method

is the calculation of the amplitude of the reflected wave given the SLD of the interface. In the optical matrix method, the interface is divided into many slices in which the SLD or refractive index is assumed to be constant, as shown in Figure 4-3.

In order to determine the reflectivity from multiple layers, we consider first a single interface between two mediums with refracted index n_1 and n_2, respectively (Figure 4-4). The reflectivity can be determined from the continuity of wave functions and their derivatives at interfaces without solving the Schrodinger equation. In medium I, the wave function is[39]

$$\psi_1(z) = e^{ik_0 \sin\theta_0 z} + R^{1/2} e^{-ik_0 \sin\theta_0 z} \tag{4-5}$$

in which k_0 is the wave vector of the incident wave.

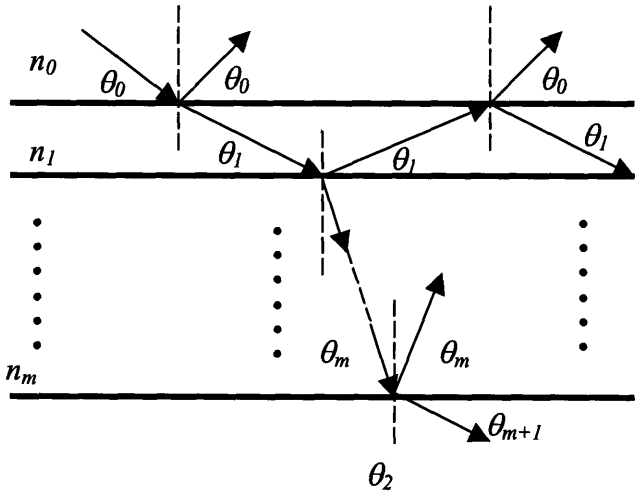

Figure 4-3 Schematic illustration of the optical matrix method. n_0, n_1, and n_m are refracting indices of thin layer 0, thin film 1, and thin layer m. θ_1, θ_2, and θ_m are the incident angles of neutron beams in thin layer 0, thin film 1, and thin layer 2.

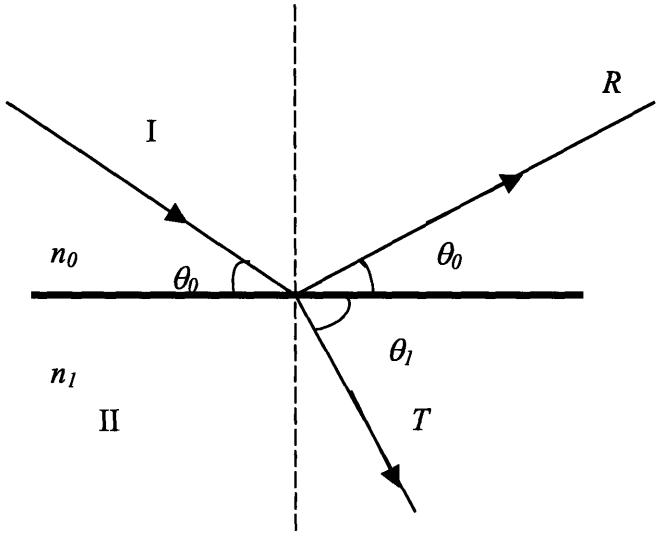

Figure 4-4 Reflection from an interface between two optically distinct media. θ_0 is the angle between the incident (or reflected) wave and the interface. θ_1 is the angle between the refracted wave and the interface. T and R are the intensities of the refracted and reflected waves, respectively. n_0 and n_1 are the refractive indices of the two media.

Similarly, in medium II, wave function is[39],

$$\psi_1(z) = T^{1/2} e^{ik_1 \sin\theta_1 z} \tag{4-6}$$

in which k_1 is the wave vector of the refracted wave.

Without losing generality, we assume that the interface is located at $z=0$. Wave functions and their first derivatives in media I and II should be continuous at interface[39],

$$1 + R^{1/2} = T^{1/2} \tag{4-7}$$

and

$$k_0 \sin\theta_0 - R^{1/2} k_0 \sin\theta_0 = k_1 T^{1/2} \sin\theta_1 \tag{4-8}$$

Finally, from mass conversation of neutrons, we have

$$T + R = 1 \tag{4-9}$$

Solving equations (4-7), (4-8), and (4-9) simultaneously, we show that the reflectivity is given by[39],

$$R = \left| \frac{k_0 \sin\theta_0 - k_1 \sin\theta_1}{k_0 \sin\theta_0 + k_1 \sin\theta_1} \right|^2 \tag{4-10}$$

The reflectivity for a thin layer (see Figure 4-5) with thickness d can be calculated by the same procedure. The only difference is that there are now three refractive indices and two interfaces. By matching both wave functions and their derivatives at the two interfaces, the reflectivity is found to be[39],

$$R = \left| \frac{r_{01} + r_{12} \exp(2i\beta)}{1 + r_{01} r_{12} \exp(2i\beta)} \right|^2 \tag{4-11}$$

where r_{ij} is defined as $\frac{n_i \sin\theta_i - n_j \sin\theta_j}{n_i \sin\theta_i + n_j \sin\theta_j}$, and $\beta = \frac{2\pi}{\lambda} n_1 d_1 \sin\theta_1$.

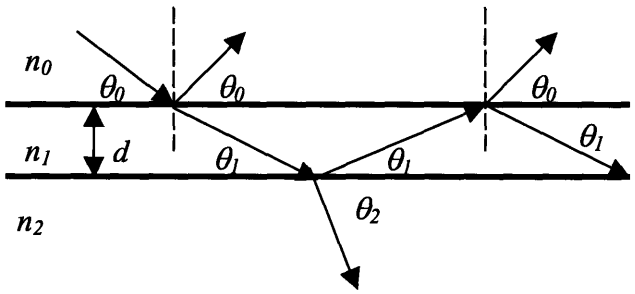

Figure 4-5 Reflection from a thin layer of thickness *d*. n_0, n_1, and n_2 are refractive indices of optical medium 1, thin film , and optical medium 2. θ_1, θ_2, and θ_3 are the incident angles of the neutron beams in medium 1, thin film, and medium 2, respectively.

The refractive index n can be calculated from the SLD of the thin layer[39],

$$n = 1 - \frac{2\pi\rho_b}{k^2} \tag{4-12}$$

in which n is the refractive index, ρ_b is the SLD of the thin layer, and k is the wave vector.

For the general case, the interface is approximated by a sequence of layers, each with a constant refractive index, as shown in Figure 4-3. Following the same procedure as used in deriving (4-10) and (4-11), the reflectivity R can be expressed in terms of the components of a 2×2 matrix M, which is the product of a series of matrices M_i associated with each of the layers[39].

$$M = M_1 M_2 \ldots\ldots M_n$$

and

$$M_i = \begin{bmatrix} \cos\beta_i & -(i/\kappa_i)\sin\beta_i \\ -i\kappa_i \sin\beta_i & \cos\beta_i \end{bmatrix} \tag{4-13}$$

in which $\kappa_i = n_i \sin\theta_i$.

The reflectivity R is[39],

$$R = \left| \frac{(M_{11} + M_{12}\kappa_s)\kappa_a - (M_{21} + M_{22})\kappa_s}{(M_{11} + M_{12}\kappa_s)\kappa_a + (M_{21} + M_{22})\kappa_s} \right|^2 \tag{4-14}$$

in which the subscript a refers to the outer (air) medium and s to the final (substrate) medium, and M_{11}, M_{12}, M_{21},and M_{22} are the elements of matrix M.

The optical matrix method is well-suited for calculation of the reflectivity from a complex interface. However, when applying this method to analyze experimental data, one often suffers from the difficulty of extracting clear physical pictures from the fitted results. The optical matrix method results in a series of thin layers with certain thicknesses and reflective indices, and one usually needs other supportive information about interface structure to determine the physical significance of these results.

4.3.3 Kinematic Approximation

In equation (4-5), the reflectivity is difficult to calculate because of the appearance of the total wave function in the integrand. However, for thin interfaces and weak reflection, equation (4-5) can be simplified significantly by replacing the total wave function with the incident wave function e^{ikz}. Then equation (4-5) becomes

$$\psi_{reflect}(k,z) = \frac{-i}{2k}(e^{-ikz}{}_{|z->\infty}) \int_{-\infty}^{+\infty} dz'[-4\pi\rho(z')]e^{2ikz'} \tag{4-15}$$

and can be transformed to,

$$\psi_{reflect}(k,z) = \frac{4\pi}{iQ} \int_{-\infty}^{+\infty} dz' \rho(z') e^{iQz'}$$

Correspondingly, the reflectivity can be expressed as[39],

$$R = \frac{16\pi^2}{Q^2} \left| F(\rho(z)) \right|^2 \tag{4-16}$$

or in its alternative form,

$$R = \frac{16\pi^2}{Q^4} \left| F(\frac{d\rho(z)}{dz}) \right|^2 \tag{4-17}$$

where R is the reflectivity; $Q=2k$ is the scattering wave vector; $\rho(z)$ is the SLD profile of the interface; F represents Fourier transformation; and z is the distance along the normal to the interface.

Equation (4-16) is the so-called kinematic approximation, in which the total wave function is approximated by the incident wave function, and is valid when the amplitude of the reflected wave is much smaller than that of the incident wave. Simultaneously, because in the kinematic approximation, the SLD distribution is related directly to the

reflectivity, the fluctuation of the interface is relatively easy to take into account by simulating the interface as having a smooth spatial distribution in SLD. Therefore, in the case of a thin and fluctuating interface, the kinematic approximation is better than the optical matrix method for extracting information on the adsorbed layer structure.

4.3.4 Scattering Length Density Distribution along within the Interface

According to equation (4-16), the Fourier transformation of the SLD profile can be obtained from reflectivities measured as a function of Q. Although, theoretically, the SLD profile can be extracted from inversion of its Fourier transformation, it is impractical to do so because of the finite Q range covered by the experiment. The SLD profile can be extracted from experimental reflectivities through model fitting, however. The SLD profile of the surfactant adsorbed layer ρ(z) can be represented by the sum of the SLDs of each segment $\rho_i(z^4)$

$$\rho(z) = \sum_i \rho_i(z) \tag{4-18}$$

where each $\rho_i(z)$ can be calculated from the scattering length, molecular area, and segment distribution through[40],

$$\rho_i(z) = \frac{b_i}{A} p_i(z) \tag{4-19}$$

in which b_i is the scattering length of the ith segment, A is its molecular area, and $p_i(z)$ is the probability that part of ith segment is located at position z normal to the interface.

At the position where the surfactant segment is mixed with the solvent, the solvent probability distribution $p_s(z)$ is based on the simple assumption that there are no vacancies in the liquid bulk phase. The space was occupied either by a surfactant segment or by solvent molecules. Thus,

$$p_s(z) = \frac{A - \sum_i V_i p_i(z)}{V_s} \tag{4-20}$$

where V_s is the van der Waals hard sphere volume of a solvent molecule, and V_i is the van der Waals hard sphere volume of the i_{th} segment of the surfactant.

Finally, the SLD profile at the interface can be expressed as,

$$\rho(z) = \frac{1}{A}\sum_i b_i p_i(z) + b_s \frac{A - \sum_i V_i p_i(z)}{V_s} \tag{4-21}$$

for $z < z_0$ beneath the air-liquid interface, and

$$\rho(z) = \frac{1}{A}\sum_i b_i p_i(z) \tag{4-22}$$

for $z > z_0$, above the air-liquid interface, where b_s is the scattering length of the solvent; and z_0 is the position of the water interface. The coordinate system is such that the positive direction of the z axis is directed toward the air phase.

The scattering lengths b_i and the van der Waals volumes V_i are all tabulated in handbooks. The structural information on the interface is contained in the segment probability distribution function $p_i(z)$, which we will discuss in the next section.

4.3.5 Surfactant Segment Distribution

The segment probability distribution function $p_i(z)$ contains all of the fitting parameters that characterize the surfactant conformation at the interface, and plays a crucial role in the analysis of neutron reflection spectra.

Adsorbed surfactant layers have been investigated extensively using neutron reflection. In almost all published works, it has been reported that the segment distribution $p_i(z)$ can be captured by the Gaussian distribution function[3,4], and the resulting SLD can be used to fit experimental reflectivities satisfactorily. It can be proved from mean field theory that if surfactant molecules have sufficient free space at the

interface and fluctuate significantly, the segment distribution should be Gasussian, and described by,

$$p_i(z) = \frac{1}{\sqrt{2\pi}\sigma_i} e^{-\frac{(z-z_i)^2}{2\sigma_i^2}} \tag{4-23}$$

in which σ_i is the deviation from, and z_i is the position of, the center of the segment. Because the Fourier transform of the Gaussian distribution can be expressed analytically, i.e.,

$$F[p_i(z)] = e^{iQz_0} e^{-\frac{Q^2\sigma_i^2}{2}} \tag{4-24}$$

the reflectivity of the interface can be calculated by,

$$R = \frac{16\pi^2}{A^2Q^2}\left|\sum_i b_i e^{iQz_i} e^{-\frac{Q^2\sigma_i^2}{2}}\right|^2 \tag{4-25}$$

in NRW, where z_i is the center position of i^{th} segment.

In solvent D_2O, the situation is more complicated because of the appearance of sharp interface. Under such circumstances, the Fourier transform of the SLD over the interface is,

$$F[\rho(z)] = \sum_i \frac{1}{A} e^{iQz_i}\left(b_i e^{-\frac{Q^2\sigma_i^2}{2}} - b_w \frac{V_i}{V_w}(A_i + iB_i)\right) + \frac{i}{V_w Q} e^{iQz_0} \tag{4-26}$$

in which z_0 is the position of air-D_2O interface; $A_i = \frac{1}{\sqrt{2\pi}\sigma_i}\int_{z_0}^{+\infty} dz \cos Qz e^{-\frac{(z-z_i)^2}{2\sigma_i^2}}$ and $B_i = \frac{1}{\sqrt{2\pi}\sigma_i}\int_{z_0}^{+\infty} dz \sin Qz e^{-\frac{(z-z_i)^2}{2\sigma_i^2}}$. By substituting (4-26) into (4-16), the reflectivity from the adsorbed layer in D_2O can be obtained in a straightforward manner.

As shown by both experiments and theoretical analysis, the Gaussian distribution is a good description of loose adsorbed layers, in which the surfactant occupies a large molecular area and fluctuates without severe steric restriction. However, in a dense adsorbed layer, molecular area is small, and surrounding surfactants exert a significant influence on any specific surfactant through hard sphere repulsion and other interactions. As a result, the surfactant is actually confined in a well-defined cylindrical cavity whose wall consists of surrounding surfactants. The amplitude of fluctuation is also significantly

lower than that in a loose layer. Under such circumstances, it is to be expected that the Gaussian function is no longer able to capture the segment distribution in the adsorbed layer. A new distribution function must be found to characterize the segment distribution in such close-packed adsorbed layers.

The segment distribution in a dense layer can be analyzed through mean field theory. Our derivation depends on the assumption that the fluctuation magnitude is smaller than or comparable to the tilt angle, which is the equilibrium angle between surfactant and the normal to the interface. For surfactants undergoing drastic fluctuations, the central limit theorem assures that their segment distributions can be well approximated by the Gaussian function.

Consider one tagged surfactant segment in the adsorbed layer, whose length is l, and tilted from the normal to interface with angle θ at equilibrium. We also assume that the length of this segment is of the same order as the neutron wavelength or shorter, so it is safe to neglect the internal degrees of freedom of the segment, and idealize it as a rigid rod. Moreover, in the dense adsorbed layer, the equilibrium tilt angle is small as the consequence of severe steric restriction exerted by surrounding surfactants.

The tagged surfactant segment is assumed to fluctuate around its equilibrium angle. Because of the restriction exerted by surrounding surfactants, the amplitude of this fluctuation is very small. According to the spirit of mean field theory, this tagged segment can be viewed as sitting in a sea of surfactant segments, and feel a smeared interaction potential, U. For any specific point within this segment, this potential is a function only of the tilt angle θ and the equilibrium tilt angle θ_c, $U(\theta,\theta_c)$. Because the fluctuations are small, $U(\theta,\theta_c)$ can be expanded as,

$$U(\theta,\theta_c) = U(\theta_c) + \frac{1}{2!}\frac{\partial^2 U(\theta,\theta_c)}{\partial\theta^2}\Big|_{\theta=\theta_c}(\theta-\theta_c)^2 + O(\theta^3) \qquad (4\text{-}27)$$

in which only the second derivative is dominant; the first derivative is zero.

According to statistical mechanics, the probability that a segment takes as a tilt angle θ is,

$$\Pr ob(\theta) = se^{-\frac{U(\theta,\theta_c)}{kT}} = se^{-\frac{U(\theta_c)+\frac{1}{2}c(\theta-\theta_c)^2}{kT}} \qquad (4\text{-}28)$$

in which s is the normalization constant, T is temperature, k is Boltzman constant, and c is the constant related to the physical properties of the surfactant . The probability density in (4-28) is Gaussian, and can be expressed more simply as,

$$f(\theta') = \frac{1}{\sqrt{2\pi\langle\theta^2\rangle}} e^{-\frac{\theta'^2}{2\langle\theta^2\rangle}} \tag{4-29}$$

in which $<\theta^2>$ is the variance of the angle fluctuations and depends on temperature T and properties of surfactant (from $U(\theta)$), and θ' is θ - θ_c, the difference between tilt angle and the equilibrium tilt angle.

In specular neutron reflection, only the density distribution normal to the interface is of interest. As a result of the angular fluctuations, the projected length of the segment on the normal to the interface changed with time and is shorter than the segment length,

$$\frac{l\cos\theta_c - l\cos\theta}{l\cos\theta_c} = \frac{1}{2}\theta'^2 + \tan(\theta_c)\theta' \tag{4-30}$$

It is interesting to note that, even for small fluctuations, the segment density distribution is still Gaussian if the equilibrium tilt angle θ_c is far larger than θ'.

It is convenient to work with strain $\bar{L}(\theta')$, defined as[1],

$$\bar{L}(\theta') = \frac{l\cos\theta_c - l\cos\theta}{l\cos\theta_c} = \frac{1}{2}\theta'^2 + \tan(\theta_c)\theta' \tag{4-31}$$

The probability density of $\bar{L}(\theta')$ is the convolution of two random variables $Y = \frac{1}{2}\theta'^2$ and $X = (\tan\theta_c)\theta'$, with probability density functions,

$$f_X(x) = \frac{1}{\sqrt{2\pi\sigma_X^2}} e^{-\frac{x^2}{2\sigma_X^2}} \tag{4-32}$$

and

$$f_Y(y) = \frac{1}{\sqrt{\pi y\sigma_\theta^2}} e^{-\frac{y}{\sigma_\theta^2}} \tag{4-33}$$

[1] The linear term can also be considered as the variable to describe the segmental length variation as the result of segment conformation change

respectively, in which $\sigma_X^2 = \tan^2(\theta_c)\sigma_\theta^2$ is the standard deviation of random variable *X*, and $\sigma_\theta^2 = \langle \theta'^2 \rangle$ is the standard deviation of θ'.

This density distribution function of strain $\bar{L}(\theta)$ is

$$f_L(\overline{L(\theta)} = \bar{l}) = \int_0^\infty dz f_X(\bar{l} - z) f_Y(z) = \frac{1}{\sqrt{\pi \bar{l} \sigma_\theta^2}} \frac{1}{\sqrt{2\pi\sigma_X^2}} \int_0^\infty dz e^{-\frac{(\bar{l}-z)^2}{2\sigma_X^2}} e^{-\frac{z}{\sigma_\theta^2}} \tag{4-34}$$

Above density distribution can be integrated out as,

$$f_L(\overline{L(\theta)} = \bar{l}) = \frac{1}{2\pi\sigma_\theta^2 \tan(\theta_c)} \sqrt{\tan^2(\theta_c) - \bar{l}} e^{-\frac{\bar{l}^2}{2\sigma_\theta^2 \tan^2(\theta_c)} + \frac{(\bar{l}-\tan^2(\theta_c))^2}{4\sigma_\theta^2 \tan^2(\theta_c)}} K_{0.25}[\frac{(\bar{l} - \tan^2(\theta_c))^2}{4\sigma_\theta^2 \tan^2(\theta_c)}]$$

for $\bar{l} < tan^2(\theta_c)$, and

$$f_L(\overline{L(\theta)} = \bar{l}) = \frac{1}{2\sqrt{2}\sigma_\theta^2 \tan(\theta_c)} \sqrt{\bar{l} - \tan^2(\theta_c)} e^{-\frac{\bar{l}^2}{2\sigma_\theta^2 \tan^2(\theta_c)} + \frac{(\bar{l}-\tan^2(\theta_c))^2}{4\sigma_\theta^2 \tan^2(\theta_c)}} \{I_{0.25}[\frac{(\bar{l} - \tan^2(\theta_c))^2}{4\sigma_\theta^2 \tan^2(\theta_c)}] + I_{-0.25}[\frac{(\bar{l} - \tan^2(\theta_c))^2}{4\sigma_\theta^2 \tan^2(\theta_c)}]\}$$

for $\bar{l} > tan^2(\theta_c)$.

(4-35)

in which $K_{0.25}(x), I_{0.25}(x)$ and $I_{-0.25}(x)$ are the modified Bessel functions[41].

In order to obtain the density distribution function for a given segment, we establish the local coordinate for this segment such that origin is set to the middle point of the segment, the positive direction of z axis pointing away from the bulk water phase. The density distribution function of the segment is the integral of the density distribution function for the segment length, i.e.,

$$pdf(x) = n \int_x^{l/2} dz p_l(z) \tag{4-36}$$

in which x is the position of a point within the half segment $(0, l/2)$, $p_l(z)$ is the probability distribution function for segment whose projection length is *z*, *n* is the normalization constant. The probability distribution function for the projection length is easily calculated from the PDF for the strain,

$$p_l(z) = \frac{2}{l\cos\theta_c} f_l\left(1 - \frac{2z}{l\cos\theta_c}\right) \tag{4-37}$$

such that the segment distribution function is, finally,

$$pdf(x) = n\int_a^b dw f_l(w) \tag{4-38}$$

in which a is the lower limit, $1 - \frac{2x}{l\cos\theta_c}$ and b the upper limit, $1 - \frac{1}{\cos\theta_c}$.

Equation (4-38) gives the probability distribution function for $x \in (0, \frac{l}{2})$, the density distribution for $x \in (-\frac{l}{2}, 0)$ is just *pdf(-x)* because of the symmetry of the density distribution function about the middle point of the segment. After taking the Fourier transforms of the probability distribution (4-38) for each segment *i*, and substituting them into (4-18), (4-19), and (4-16), we can obtain the reflectivity from the interface. Because of the complexity of the probability distribution (4-38), analytical solutions cannot be found and the integrals must be evaluated numerically.

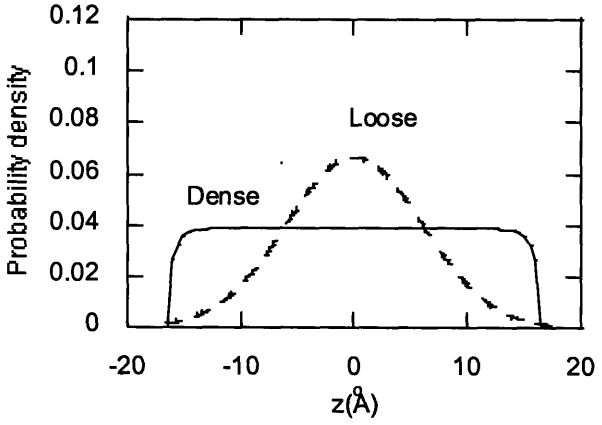

Figure 4-6 The schematic probability density distribution of a segment in a dense adsorbed layer (solid line) and in a loose adsorbed layer (dashed line). The z-axis is normal to the interface and the origin is at the middle point of the segment.

4.4 Result and Discussion

4.4.1 Experimental results

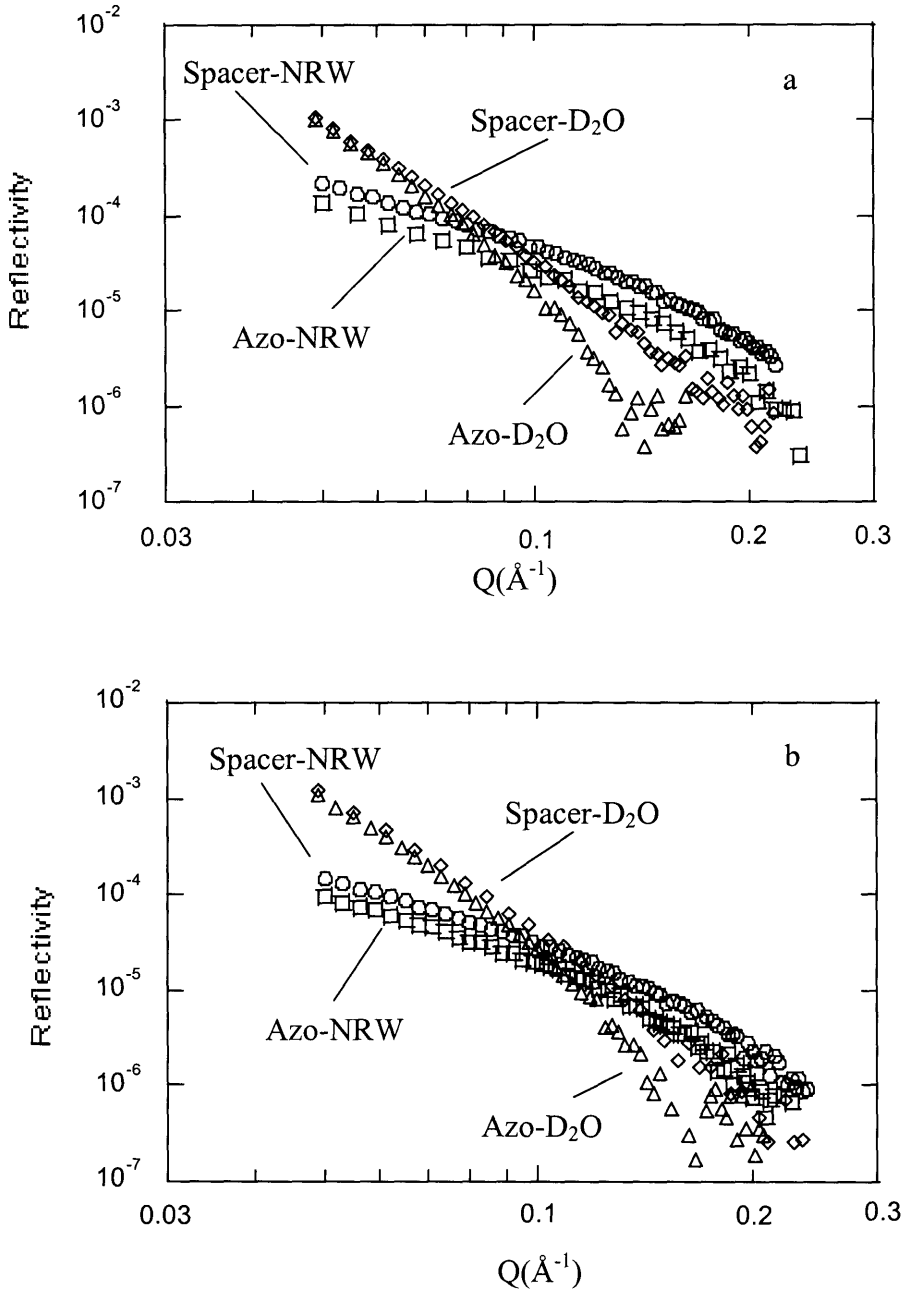

Figure 4-7 The measured reflectivities from a $C_4AzoOC_6E_2$ solution. (a) Trans isomer (b) Cis isomer. Azo indicates the azobenzene deuterated species, and spacer indicates the spacer deuterated species; D_2O means the D_2O as solvent; NRW means that NRW is solvent.

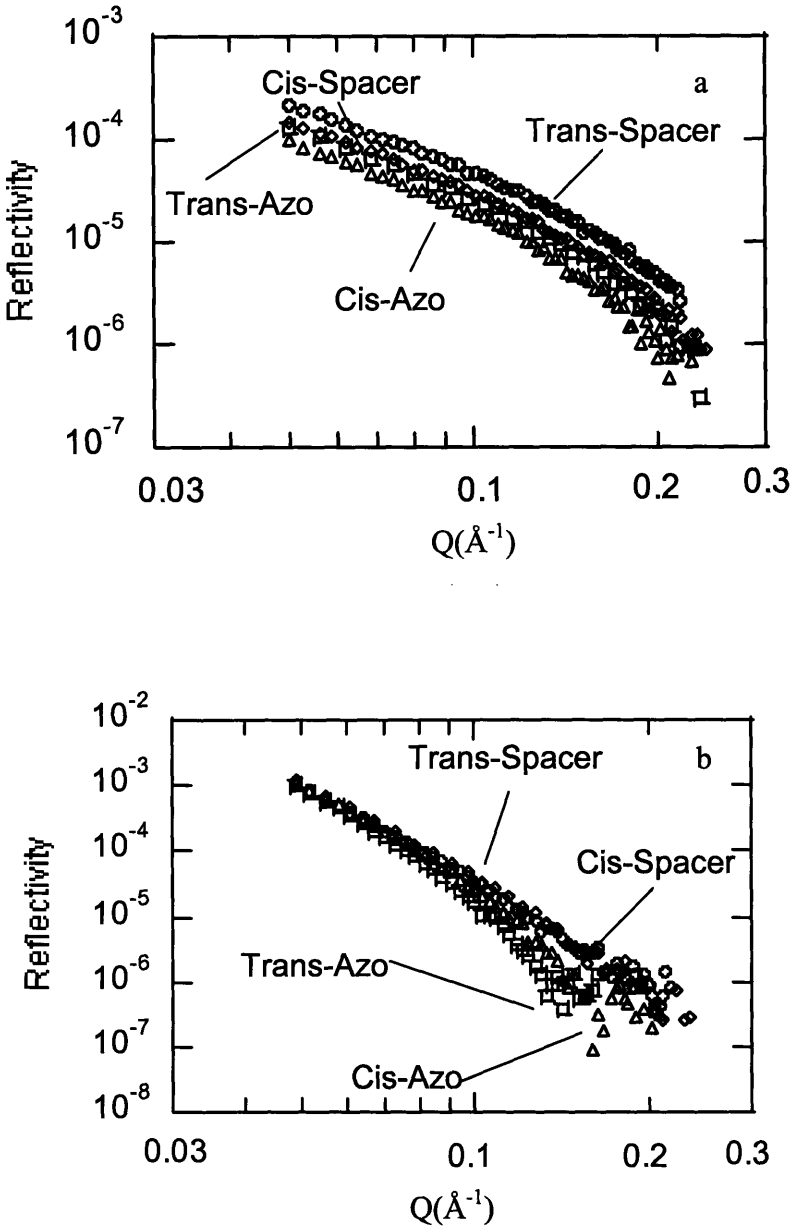

(b)

Figure 4-8 Measured reflectivities in trans and cis $C_4AzoOC_6E_2$ are plotted together in (a), zero contrast solvent, and in (b) D_2O. Spacer indicates spacer deuterated species, and azo indicates azobenzene deuterated species.

The measured neutron reflectivities of both trans and cis isomer samples in both NRW and D_2O are plotted in Figure 4-8. As shown in the figure, in NRW, reflectivities

from azobenzene-deuterated and spacer-deuterated samples, in both the trans and cis forms, essentially parallelled each other in the low Q range. A similar situation is evident for D_2O, in which reflectivities from the two species (both trans and cis forms) almost overlapped each other in the low Q range. This tendency is consistent with scale analysis. In neutron reflection, the structural features of the interface that can be resolved are roughly of the order of $2\pi/Q$. In the small Q range, the spatial resolution in neutron reflection is much larger than the thickness of the adsorbed layer, so in these Q-ranges the reflectivities reflect only the simple structureless thin layers with different SLDs. This explains why reflectivities from both samples had similar trends in the low Q range. The different magnitudes of the reflectivities in the azobenzene-deuterated and spacer-deuterated samples arose mainly from their different SLDs. This argument can be described quantitatively by the thin-layer approximation, in which the molecular area can be extracted from the reflectivities in NRW over the small Q range [3].

$$R = \frac{16\pi^2\left(\sum_i b_i\right)^2}{A^2} Q^{-2} \qquad (4\text{-}39)$$

in which A is the molecular area, R is the reflectivity, and $\sum_i b_i$ is the scattering length of the entire surfactant. If we plotted R vs Q^{-2}, a straight line is obtained, with slope of $\frac{16\pi^2\left(\sum_i b_i\right)^2}{A^2}$, from which we can estimate the molecular area in the adsorbed layer. This approximation is only valid when $Ql << 1$, where l is the thickness of the adsorbed layer. The molecular areas calculated by equation (4-39) are 30 $Å^2$ for the trans isomer and 45 $Å^2$ for the cis form of the surfactant.

For Q greater than 0.1 $Å^{-1}$, reflectivities from the two deuterated samples (both trans and cis isomer) began to deviate from each other, this deviation becoming more pronounced with increasing Q. This deviation in the large Q range was even more obvious in D_2O than in NRW. These deviations in the reflectivities implied that the azobenzene and spacer groups offered different spatial distributions within the adsorbed

layer. These results suggest that the cis isomer is more loosely packed at the interface than the trans isomer.

More strikingly, it was found that reflectivities of the trans adsorbed layer were significantly different from those of the cis adsorbed layer for both azobenzene-deuterated and spacer-deuterated species, in both NRW and D_2O, as shown in Figure 4-8. The difference in reflectivities between the trans and cis isomers are more significant in the large Q range, indicating that the adsorbed layer structures for the trans and cis isomers, and therefore the interfacial conformations of these isomers, were quite different from each other, consistent with the conclusions drawn from surface tension measurements.

4.4.2 Fitting Results

Although the structural differences in the adsorbed layer between the trans and cis forms can be perceived qualitatively from the reflectivity curves, a quantitative description of the surfactant segment distributions can be revealed only by model fitting.

In this study, we adopted the density distribution functions given by equations (4-38) and (4-23) to describe surfactant segment distributions in trans and cis adsorbed layers, respectively. The kinematic approximation was used to relate the reflectivity to the SLD, as given in equations (4-16), and (4-18)- (4-22). For each of the trans and cis forms, all four reflectivity curves were fitted globally. The fittings were conducted in MATLAB 6.5 with Optimization toolkit.

In the case of D_2O, the roughness of the air-D_2O interface, which comes from short wavelength capillary waves, is incorporated by weighting the reflectivity with an additional factor $e^{-Q^2\sigma_s^2}$ where σ_s is the surface roughness. In all samples in this study, the surface roughness σ_s was found to be about 2.5 Å, which is very close to the value reported in the literature.

In Figures 4-9 and 4-10, we show the theoretical fitting and resultant segment distribution in adsorbed layers of the cis and trans forms, respectively. The optimal parameters are summarized in Table 4-1.

In the fitting, each segment is specified by its center position, standard deviation (cis isomer) or angular fluctuation (trans), and the equilibrium tilt angle (trans only). The position of air-water interface is taken as an additional fitting parameter. The relative distance between adjacent segments is calculated from the differences in their center positions.

Table 4-1 Optimal parameters in fitting of neutron reflectivities

Sample	A, Å^2	σ_{azo}, Å	σ_{spacer}, Å	σ_{head}, Å	$\delta_{w\text{-}azo}$, Å	$\delta_{azo\text{-}spacer}$, Å	$\delta_{spacer\text{-}hea}$, Å
Trans	30.0	0.1	0.01	0.01	9.6	7.0	6.0
cis	45.0	6.00	3.35	6.00	3.16	1.5	6

Note: A is the molecular area. In cis form, σ_{azo}, σ_{spacer}, and σ_{head} are the deviations of the azobenzene, spacer and head groups, respectively. In trans form, σ_{azo}, σ_{spacer}, and σ_{head} are the dimensionless angular fluctuations of the azobenzene, spacer and head groups, respectively. $\delta_{w\text{-}azo}$ is the distance between the azobenzene group and the water interface; $\delta_{azo\text{-}spacer}$ and $\delta_{spacer\text{-}hea}$ are the distances between the azobenzene and spacer groups, and the spacer and head groups, respectively. In the trans fitting, the equilibrium tilt angle of each segment is also a fitting parameter. However, the optimal values of the tilt angles are very small (the tile angles for azobenzene, spacer and head group are 0.1, 0.01, and 0.01, respectively), and essentially zero, so we do not list them in the Table 4-1.

From the Figure4-9 (b), it can be seen that most of the head group is immersed in the bulk water phase; and that the hydrophobic segments such as azobenzene and the spacer group are mostly in the air, consistent with the usual picture of surfactant conformations at the interface, in which the hydrophobic group lies above the interface while the hydrophilic group is anchored within the water sub-phase. The large width of the distribution of segments indicates that surfactants undergo drastic fluctuation at the interface, which is consistent with our model assumption and also consistent with several recent molecular dynamic studies on adsorbed surfactant layers. It would appear from

these simulations that, in the not-too-closely packed adsorbed layer, the fluctuation amplitudes of surfactant segments are of the same order of, and sometimes even larger than, their lengths. This clearly appears to be the case in the experimentally-determined segment distributions for the cis-surfactant. Probably the most striking feature revealed by Figure 4-9 (b) is the close distance between the azobenzene and spacer groups and the overlap of their distributions to a large extent. It is found from neutron reflection that the relative distance between these two groups is only about 1.5 Å, and the standard deviations are 6.0Å (azobenzene) and 3.35 Å(spacer), respectively. It can be inferred that the azobenzene and spacer groups are located at essentially the same height above the interface. This kind of segment distribution implies that the tail group fold over to lie in the interface zone. Such a near distance of the two groups would not be possible if the tail group were oriented vertically toward the air. Moreover, it is found that the distance between the center of azobenzene group and interface was 3.16 Å. This, together with standard deviation of azobenzene and spacer groups, indicated that both the azobenzene and the spacer groups are close to the air-water interface. This quantitative structural information on segment distributions excludes the possibility of a regular vertical conformation, and strongly supports the loop conformation, in which the surfactant head is immersed in the water sub-phase, and the spacer loops out from the interface with both ends anchored at the interface. As a result, the azobenzene group is also located at almost the same position above the interface as the spacer and most of their segments overlap in their positions to the interface. The segment density distributions from neutron reflection analysis provide the strong support for this picture. Moreover, the molecular area 40 $Å^2$ obtained from neutron reflection data is consistent with the loop conformation, especially fit with spacer loop. Therefore, we conclude that the cis surfactant takes on a loop conformation at the air-water interface.

The theoretical fitting and resultant segment distributions for the trans form are shown in Figure 4-10. The Gaussian density distribution was not able to fit the experimental reflectivities satisfactorily, and even for the best fits, there were always significant deviations between the experimental data and fitting curves. As shown in Figure 4-10 (b), however, the new density distribution (4-38) did give excellent theoretical fitting to the experimental data, strongly supporting the assumptions about

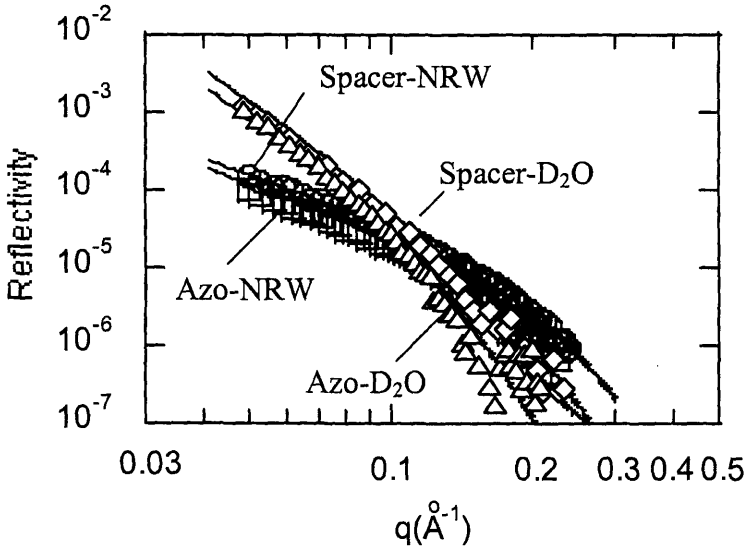

(a)

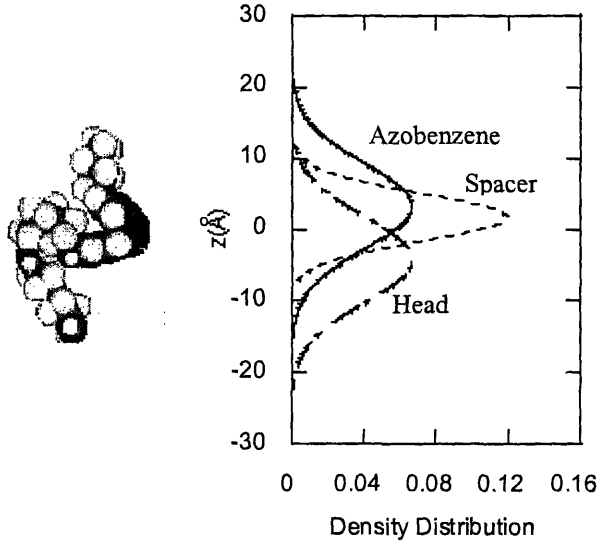

(b)

Figure 4-9 The curve fitting of neutron reflectivities in cis $C_4AzoOC_6E_2$ (a) and corresponding segmental density distribution (b). In (a), solid lines represent model fitting. Spacer and azo mean the spacer and azobenzene deuterated species, respectively. NRW and D_2O indicate the NRW solvent and D_2O, respectively.

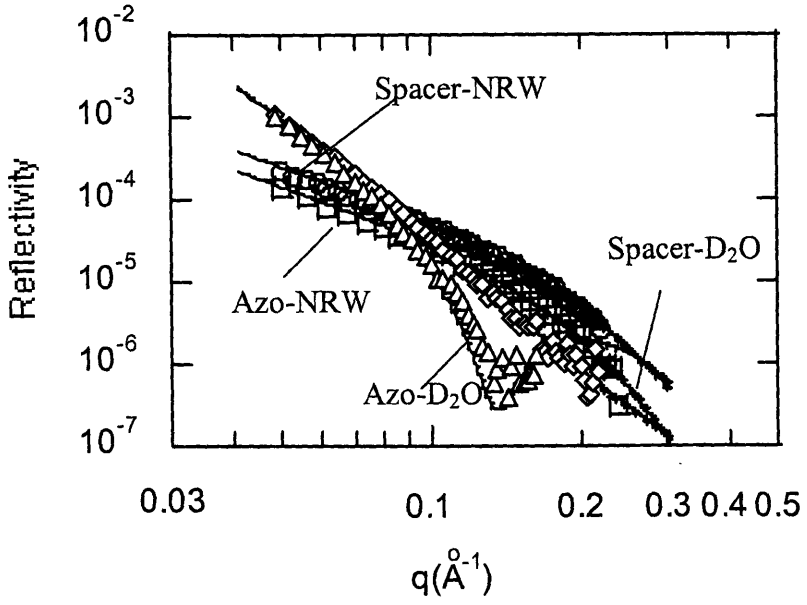

(a)

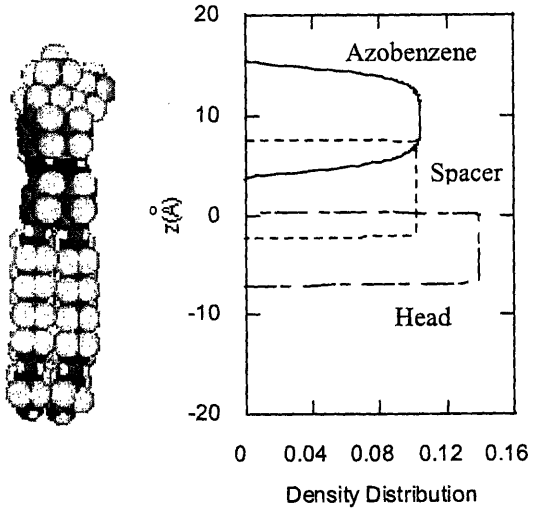

(b)

Figure 4-10 The curve fitting of neutron reflectivities in trans $C_4AzoOC_6E_2$ (a) and corresponding segmental density distribution (b). In (a), solid lines represent model fitting. Spacer and azo mean the spacer and azobenzene deuterated species, respectively. NRW and D_2O indicate the NRW solvent and D_2O, respectively.

the segment distributions inherent in the development of this model. The optimal fitting parameters are listed in Table 4-1. As shown in Figure 4-10(b), the head group of the trans form was immersed in the water sub-phase, consistent with its hydrophilic nature; the tail groups, such as azobenzene and spacer group were all oriented vertically related to and away from the air-water interface. In contrast to the cis isomer, in which the azobenzene and spacer were located almost at the same distance from the air-water interface, in the trans from, the azobenzene group was well-separated from the spacer with relative distance as large as 6 Å. This result is consistent with the surfactant conformation that both groups are aligned along the normal to the interface. Moreover, the molecular area 30 $Å^2$ as obtained from NR analysis is close to the projection area of the vertical benzene group and supports the vertical surfactant conformation at the interface. Based on above analysis, we can conclude that trans isomer take vertical conformation at the adsorbed layer. In addition, as shown in the density distributions for the trans surfactant, all segments showed only small fluctuations, consistent with our model assumptions.

There is a discrepancy in the molecular areas derived from the NR and the surface tension measurements. In the trans form, the molecular area found from the NR fitting was 30 $Å^2$, while it was about 22$Å^2$ from surface tensions using Gibbs equation. From the size of various groups in the $C_4AzoOC_6E_2$ surfactant obtained from quantum mechanics computations using Gaussian94, the 30 $Å^2$ seems to be more reasonable than 22 $Å^2$. As discussed in Chapter 3, the surfactant $C_4AzoOC_6E_2$ is very surface active, and strongly adsorbed on various high energy surfaces. In Chapter 3, the effect of surfactant adsorption on the air-liquid interface on surface tension has been taken into account, but the adsorption of surfactant on the glass surfaces was not considered as it was thought to be unimportant. This surfactant loss may, however, cause the additional deformation of surface tension curves, with the result that the surface excess estimating using the Gibbs equation may be over-estimated. Thus, the molecular areas from surface tension measurements reported in Chapter 3 may be lower than the actual values.

4.5 Summary

In this chapter, the adsorbed layer structures of the photoresponsive surfactant $C_4AzoOC_6E_2$, were probed by neutron reflection techniques under both UV and visible illumination. The neutron reflection (NR) technique provides a non-invasive and least disruptive way to study the structure of thin, soft interfaces with atomic resolution.

The experimental NR results indicate that the structures of the adsorbed layers of trans and cis $C_4AzoOC_6E_2$ were significantly different from each other. Neutron reflectivities from the trans form showed obvious deviations from those of the cis isomers in the large Q range, in both null reflecting water (NRW) and D_2O. This deviation is consistent with there being basic structural differences in the adsorbed layers between the trans and cis isomers.

The NR data were analyzed quantitatively through model fitting within the framework of the kinematic approximation. As illustrated by surface tension studies, the cis adsorbed layer was loosely packed, which suggested that the surfactant segment distribution should be well-described by the Gaussian distribution, which led to a satisfactory fitting of experimental data. However, for the trans form, with a dense adsorbed layer, the Gaussian distribution was no longer valid for the characterization of the surfactant segment distribution, and indeed, was unable to provide good fits to the experimental data. We proposed a theoretical model to take care the segment distribution in this case. As shown by this model, because of the stringent steric restriction exerted by neighboring surfactants, the surfactant segment can only fluctuate around its equilibrium position with small amplitude. The resultant segment distribution was no longer Gaussian, but was the one that varies slowly in the middle part and rapidly at the both ends. The NR trans data were fitted very well by the proposed segment distribution, while the Gaussian type distribution function failed to give a satisfactory fit of the reflectivity data.

From a quantitative analysis of NR data, it was determined that the spacer and azobenzene group in the cis adsorbed layer overlapped each other to a large extent. It was concluded that the cis surfactants adopted a loop conformation at the interface, in which

the spacer group forms a loop, anchored at its two ends at the air-liquid interface by the E_2 head group and the ether oxygen, forcing the azobenzene group to be located at the almost the some distance as the spacer from the interface. In contrast, in the trans from, as found from NR analysis, the azobenzene group was well separated from the spacer with a relative distance as large as 6 Å. Therefore, it can be concluded that the trans surfactant is oriented vertically away from the interface as is normally pictured for most regular surfactants. The conclusions from NR analysis strongly support our interpretation of the molecular factors affecting the surface tension response as discussed in Chapter 3. The large surface tension differences between the trans and cis isomers arise from their different interfacial conformations.

4.6 Bibliography

1. Zhou, X. L. & Chen, S. H. Theoretical Foundation of X-ray and Neutron Reflectometry. *Phys. Rep.* **257**, 223-348 (1995).

2. Dietrich, S. & Haase, A. Scattering of X-rays and Neutrons at Interface. *Phys.Rep.* **260**, 1-138 (1995).

3. Lu, J. R., Thomas, R. K. & Penfold, J. Surfactant Layers at the Air/water Interface: Structure and Composition. *ADV. COLLOID INTERFACE* **84**, 143-304 (2000).

4. Lu, J. R. & Thomas, R. K. Neutron Reflection from Wet Interfaces. *J. CHEM. SOC. FARADAY T.* **94**, 995-1018 (1998).

5. Bradley, J. E. et al. Adsorption at the Liquid Surface Studied by means of Specular Reflection of Neutrons. *Langmuir* **4**, 821-826 (1988).

6. Jones, R. A. L. et al. The Form of the Enriched Surface-Layer in Polymer Blends. *Europhys. Lett.* **12**, 41-46 (1990).

7. Lee, L. T., Guiselin, O., Lapp, A. & Farnoux, B. Diect Measurements of Polymer Depletion Layers by Neutron Reflectivity. *Phys.Rev. Lett.* **67**, 2838-2841 (1991).

8. Li, Z. X. et al. The Structure of the Surface of Ethanol-Water Mixtures. *Mol. Phys.* **80**, 925-939 (1993).

9. Saville, P. M., Gentle, I. R., White, J. W., Penfold, J. & Webster, J. R. P. Specular and Off-Specular Neutron Reflectivity of a Low -Molecular-Weight Polystyrene Surfactant at the Air-Water-Interface. *J. Phys. Chem.* **98**, 5935-5942 (1994).

10. Lu, J. R., Hromadova, M., Simistter, E. A., Thomas, R. K. & Penfold, J. Neutron Reflection From Hexadecyltrimethylammonium Bromide Adsorbed at the Air/Liquid Interface-The Variation of the Hydrocarbon Chain Distribution with Surface Concentration. *J.Chem. Phys.* **98**, 11519-11526 (1994).

11. Lee, E. M., Thomas, R. K. & Rennie, A. R. Reflection of Neutrons From a Polymer Layer Adsorbed at the Quartz-Water Interface. *Europhys. Lett.* **13**, 135-141 (1990).

12. Lee, L. T., Langevin, D. & Farnoux, B. Neutron Reflectivity of an Oil-Water Interface. *Phy. Rev. Lett.* **67**, 2678-2681 (1991).

13. Cosgrove, T., Phipps, J. S. & Richardson, R. M. Neutron Reflection from a Liquid Interface. *Colloids and Surf.* **62**, 199-206 (1992).

14. Kellay, H., Hendrikx, Y., Meunier, J., Binks, B. P. & Lee, L. T. Local Properties of an AOT Monolayer at the Oil-Water Interface-Neutron-Scattering Experiments. *J.Physique II* **3**, 1747-1757 (1993).

15. Pershan, P. S., Braslau, A., Weiss, A. H. & Als-Nielsen, J. Smectic Layering at the Free-Surface of Liquid-Crystals in the Nematic Phase -X-ray Rrflectivity. *Phys.Rev. A* **35**, 4800-4813 (1987).

16. Als-Nielsen, J., Christensen, F. & Pershan, P. S. Smectic-A Order at the Surface of a Nematic Liquid-Crystal -Synchrotron X-ray -Diffraction. *Phy. Rev. Lett.* **48**, 1107-1110 (1982).

17. Als-Nielsen, J. *Physica B&C* **126**, 759 (1984).

18. Ocko, B. M., Braslau, A., Pershan, P. S., Als-Nielsen, J. & Deutsch, M. Quantitzed Layer Growth at Liquid-Crystal Surfaces. *Phy. Rev. Lett.* **57**, 94-97 (1986).

19. Zhou, X. L., Lee, L. T., Chen, S. H. & Strey, R. Observation of Surface-Induced Layering in Bicontinuous Microemulsion. *Phy. Rev. A* **46**, 6479-6489 (1992).

20. McClain, B. R. et al. X-ray Reflectivity Study of an Oil-Water Interface in Equilibrium with a Middle-Phase Microemulsion. *Phys.Rev. Lett.* **72**, 246-249 (1994).

21. Chowdhury, D. & Stauffer, D. Nucleation and Size-distribution of Holes in a Microscopic Model of Newton Black Films. *Physica A* **189**, 70-80 (1992).

22. Kjaer, K., Als-Nielsen, J., Helm, C. A., Tippmann-Krayer, P. & Mohwald, H. An X-ray-scattering Study of Lipid Monolayers at the Air Water Interface and on Solid Supports. *Thin Solid Films* **159**, 17-28 (1988).

23. Losche, M. et al. Influence of Surface-chemsitry on the Structural Organization of Monomolecular Protein Layers Adsorbed to Functionalized Aqueous Interfaces. *Biophys. J.* **65**, 2160-2177 (1993).

24. Nicklow, R. M., Pomerantz, M. & Segmuller, A. Neutron-diffraction from Small Numbers of Langmuir-Blodgett Monolayers of Manganses Stearate. *Phys. Rev. B* **23**, 1081-1087 (1981).

25. Hayter, J. B. et al. Critical Reflection of Neutrons - A New Technique for Investigating Interfacial Phenomena. *J. CHEM. SOC. FARADAY T.* **77**, 1437-1448 (1981).

26. Pomerantz, M. & Segmuller, A. High-resolution X-ray-diffraction from Small Numbers of Langmuir-Blodgett Layers of Manganese Stearate. *Thin Solid Films* **68**, 33-45 (1980).

27. Pomerantz, M., Segmuller, A., Netzer, L. & Sajiv, J. Coverage of Si Substrates by Self-assembling Monolayers and Multilayers as Measured by IR, Wettability and X-ray-diffraction. *Thin Solid Films* **132**, 153-162 (1985).

28. Tidswell, I. M. et al. X-ray Specular Reflection Studies of Silicon coated by Organic Monolayers (Alkylsiloxanes). *Phys.Rev. B* **41**, 1111-1128 (1990).

29. Thirtle, P. N. et al. Structure of Nonionic Surfactant Layers Adsorbed at the Solid/Liquid Interface on Self-assembled Monolayers with Different Surface Functionality: A Neutron Reflection Study. *Langmuir* **13**, 5451-5458 (1997).

30. McGillivray, D. J., Thomas, R. K., Rennie, A. R., Penfold, J. & Sivia, D. S. Ordered Structures of Dichain Cationic Surfactants at Interfaces. *Langmuir* **19**, 7719-7726 (2003).

31. Penfold, J. & Thomas, R. K. The Structure and Composition of Mixed Surfactants at Interfaces and in Micelles. *ACS SYMPOSIUM SER.* **861**, 96-115 (2003).

32. Diehl, H. W. & Smock, M. Critical-behavior at the Extraordinary transition - Temperature Singularity of Surface Magnetization and Order-parameter Profile to One -loop Order. *Phys.Rev. B* **47**, 5841-5848 (1993).

33. Guiselin, O. 1st Measurement of the Discontinuity Jump in a Reflectivity Curve near Total Reflection Edge. *Europhys. Lett.* **17**, 57-62 (1992).

34. Guiselin, O. Characteristic Discontinuity of the Reflectivity Curve in Vicinity of Total Reflection in the Case of an Attractive Slowly Varying Potential. *J.Phys.France* **50**, 3407-3425 (1989).

35. Jannink, G. Oscillations in the Reflectivity of a Diffuse Polymer Layer - An Analogy With the Ramsauer Townsend Effect. *J.Phys. I* **3**, 1405-1415 (1993).

36. Dietrich, S. & Schack, R. One -to-one Correspondence Between Slowly Decaying Interfracial Profiles and Reflectivity. *Phy. Rev. Lett.* **58**, 140-143 (1987).

37. Roe, R. J. *Methods of X-ray and Neutron Scattering in Polymer Science* (Oxford University Press, New York, 2000).

38. de Bergevin, F. in *X-ray and Neutron Reflectivity: Principles and Applications* (eds. Daillant, J. & Gibaud, A.) (Springer, Berlin, 1999).

39. Higgins, J. S. & Benoît, H. C. *Polymers and Neutron Scattering / and* (Clarendon Press, Oxford, 1994).

40. Li, Z. X., Dong, C. C., Wang, J. B., Thomas, R. K. & Penfold, J. Unusual Surface Structure in Layers of Cationic Gemini Surfactants Adsorbed at the Air/water Interface: A Neutron Reflection Study. *Langmuir* **18**, 6614-6622 (2002).

41. Gradsbteyn, I. S. & Ryzbik, I. M. *Table of Integrals, Series, and Products* (Academic Press, San Diego, 2000).

Chapter 5

Light Scattering, Small Angle Neutron Scattering, and Cryo-TEM Studies on Self-assembly of Photoresponsive Surfactants

5.1 Introduction

Self-assembly is one of the most fascinating properties of surfactant solutions. It has been shown to have applications in the fabrication of mesoporous materials, in micelle-facilitated filtering of organic containments and metal ions, and in micellar catalysis [1], and is believed to have extensive potential high technologies application in the future. A flexible and convenient method to control self-assembly is necessary to optimize processing. Our new class of photoresponsible surfactants, has their CMCs that change significantly when switching from visible light to UV light, as inferred from the surface tension measurements. This indicates that self-assembly in these systems is quite different under different illumination conditions [2].

The information on bulk self-assembly contained in surface tension curves is rather limited, and the detailed structure of self-aggregates cannot be acquired in this way. For practical applications, however, a thorough understanding of the structure of the self-aggregation behavior is necessary. In this chapter, we present a comprehensive investigation on the structures of self-assembling aggregates in the photoresponsive surfactant solutions under both UV and visible illumination. We show that their structures can be determined unambiguously through integration of information gleaned from light scattering, small angle neutron scattering, and cryo-TEM studies.

In scattering experiments, the incident beam (photons or neutrons) with wave vector k_i, is scattered by the system; the scattered beam arrives the detector with wave

vector k_{out}. The momentum transfer $Q = k_{in} - k_{out} = \frac{4\pi}{\lambda}\sin\frac{\theta}{2}$ where λ is the wavelength of incident beam and θ is the scattering angle (Figure 5-1), is related to the spatial resolution of scattering l through $l \sim Q^{-1}$. The typical q ranges covered by neutron and

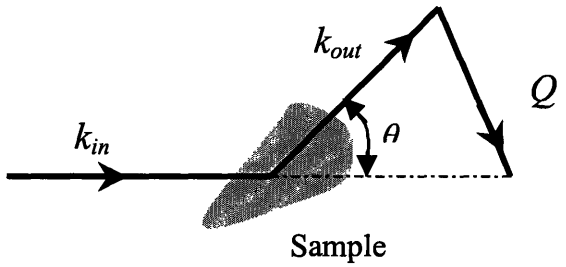

Figure 5-1 The schematic scattering geometry. k_{in} is the wave vector of the incident beam; k_{out} is the wave vector of the scattered beam; θ is the scattering angle; and q is the transfer momentum.

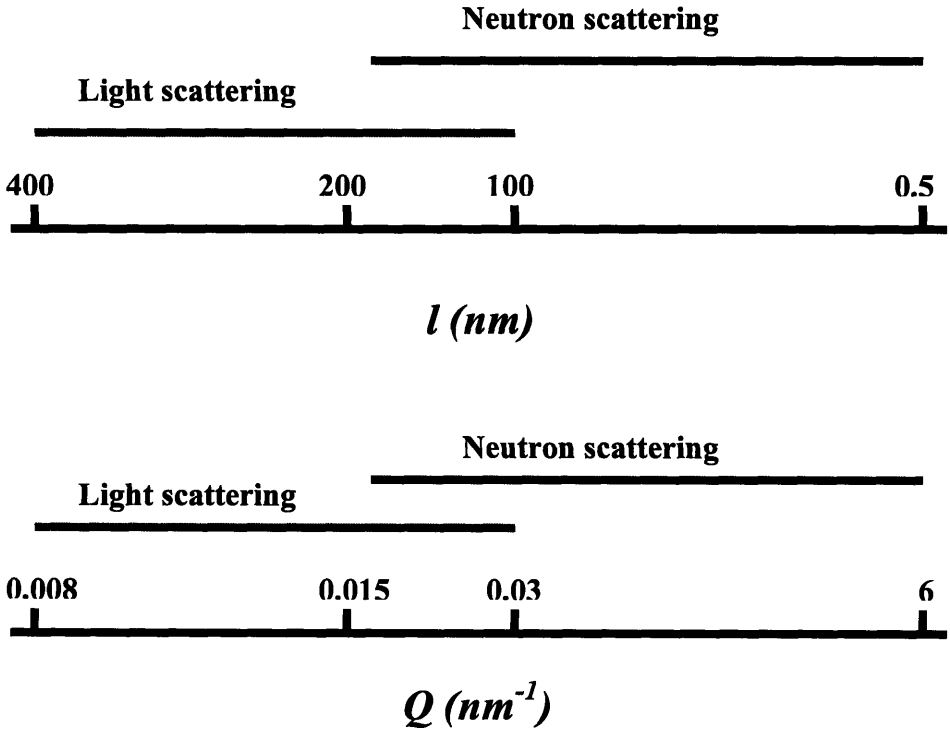

Figure 5-2 Q range and corresponding spatial resolution in light and neutron scattering.

light scattering are sketched in Figure 5-2. It is evident that the Q ranges and structural resolution in light scattering and neutron scattering are complementary to each other. Therefore, the detailed self-assembly structure over a large range of spatial scales can be revealed by combined light scattering and neutron scattering experiments.

In what follows, we first present the light scattering (both static and dynamic) studies; and then we show how to extract structural information with Angstrom resolution from small angle neutron scattering (SANS). We also show cryo-TEM pictures of self-aggregates, which verify the results from the neutron scattering experiments. Finally, a theoretical analysis is presented to assist in interpreting the experimental results.

5.2 Light Scattering

In this study, the self-assembly structures were first probed by both dynamic and static light scattering techniques. In light scattering experiments, the structure of self-assembly aggregate is easy to probe and analyze in the transparent sample; this placed the limitation that only dilute samples be used in our study. In addition, as a consequence of the large wavelength, light scattering is suitable only to probe the structure of relatively large aggregates. Normally, at low concentrations, surfactants seldom self-assemble into large aggregates, which limits the utility of light scattering (static) in probing the self-assembly behavior in surfactant solutions. However, for some special surfactants, such as $C_4AzoOC_6E_2$ in this study, it is possible to form large aggregates at quite low concentrations. Under these circumstances, light scattering becomes a valuable tool for the structural study of self-assembled aggregates. In our photoresponsive surfactant system, with the available Ar-ion laser wavelengths of 488.0 and 514 nm, a significant fraction of the cis isomer is converted back to the trans form during even the shortest period of signal collection, and hence light scattering was not suitable for the study of cis samples. Therefore, this light scattering study provides important insight on the self-assembly behavior of only trans surfactants at low concentrations.

5.2.1 Theory of Static Light Scattering

In this section, we give a brief introduction to the concepts of static light scattering, to lay down the basis for our subsequent analysis. We focus on the basic and essential formulas in static light scattering, and do not consider more complicated theoretical treatments using, e.g., the Maxwell equations. In addition, our formulations incorporate the explicit form factor in the scattering intensity, which is usually neglected in usual treatments. As can be seen later, this form factor is crucial in our light scattering data analysis.

Generally, light is scattered whenever there is a difference in dielectric constant in regions of space. According to Einstein, the dielectric constant of a medium is proportional to its density, and therefore light scattering can probe any spatial inhomogeneity when its length scale matches the transfer momentum of light (Figure 5-3). Compared with scalar waves such as those of the neutron, light is more complicated

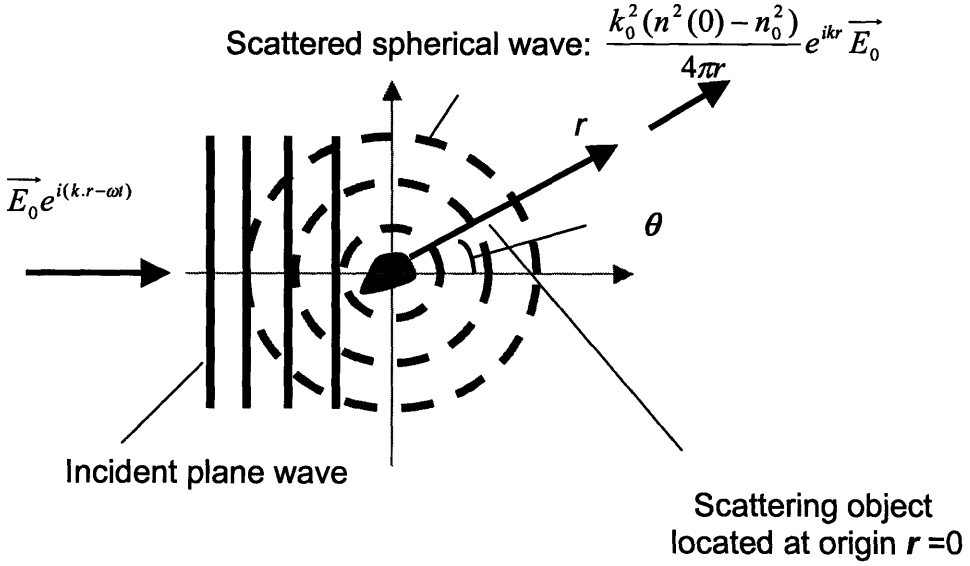

Figure 5-3 Schematic set up of light scattering experiment. $\overrightarrow{E_0}$ is the electric vector of incident light; k_0 and k are the wave vectors of light in vacuum and medium, respectively. θ is the scattering angle.

because of polarization. The electrical field after scattering is described by [3],

$$\nabla^2 \vec{E} + k^2 \vec{E} = -(n^2 - n_0^2) k_v^2 \vec{E} \tag{5-1}$$

where $k_v = \frac{2\pi}{\lambda_0}$ is the wave vector of light in vacuum, $k = n_0 k_v$ is the wave vector in the medium of refractive index n_0.

The total electric field is the superposition of the incident and scattered electrical fields[3],

$$\vec{E}(\mathrm{r},t) = \vec{E}_0 e^{i(k.r-\omega t)} + \int_{sample} d^3 r' G(\mathrm{r}-\mathrm{r}') k_v^2 (n^2 - n_0^2) \vec{E}(\mathrm{r}',t) \tag{5-2}$$

where the Green's tensor *G(r-r')* is the field at point ***r*** due to a point source at ***r'***.

In the far field, where $k|r\text{-}r'| >> 1$, Green's tensor can be shown to take an asymptotic form[3],

$$G(\mathrm{r}-\mathrm{r}') = (I - \mathrm{r}\mathrm{r}) \frac{e^{ikr}}{4\pi r} e^{-ik'r'} \tag{5-3}$$

where k' = k***r*** is the wave number of scattered light in the ***r*** direction; *I* is the unit tensor.

Thus, in this limit, the total electrical field after scattering becomes,

$$\vec{E}(r,t) = \vec{E}_0 e^{i(k.r-\omega t)} + k_v^2 (I - rr) \frac{e^{ikr}}{4\pi r} \int_{sample} d^3 r' e^{-ik'.r'} \vec{E}(r',t)(n^2(r') - n_0^2) \tag{5-4}$$

If the scattering is weak, it is appropriate to replace the total electrical field *E(**r'**,t)* with incident electrical field E_i*(**r'**,t)* in the above integral,

$$\vec{E}(\mathrm{r},t) = \vec{E}_0 e^{i(k.r-\omega t)} + k^2 (I - \mathrm{r}\mathrm{r}).\vec{E}_0 \frac{e^{ikr}}{4\pi r} \int_{sample} d^3 \mathrm{r}' e^{iQ.r'} (m^2(\mathrm{r}') - 1) \tag{5-5}$$

where $Q = k - k'$ is the transfer momentum, which is the momentum that particles transfer to the photon during collision, and $m^2(r') = \frac{n^2(r')}{n_0^2}$.

Equation (5-5) is the so-called Rayleigh-Gans-Debye approximation; it can be simplified further in VV geometry[3], in which the electric fields of both the incident and scattered waves are normal to the scattering plane,

$$\vec{E}_s(r,t) = \vec{E}_0 \frac{e^{ikr}}{r} e^{i(Q.R-\omega t)} \frac{k^2}{2\pi} F(Q) \tag{5-6}$$

where R is the position of the particle center. $F(Q) = \int_V d^3\rho e^{iQ\rho} \frac{\Delta n(\rho)}{n_0}$ is the particle form factor.

In deriving equation (5-6), we assume n is close to n_0, and that $m^2(\rho) - 1 = (1 + \frac{\Delta n(\rho)}{n_0})^2 - 1 \approx 2\frac{\Delta n(\rho)}{n_0}$ where $m(\rho) = \frac{n(\rho)}{n_0}$.

The scattering intensity, is therefore,

$$\frac{d\sigma}{d\Omega} = \frac{|E_s|^2 r^2}{|E_i|^2} = \frac{k^4}{4\pi^2} \left| \int_V d^3\rho e^{iQ\rho} \frac{\Delta n(\rho)}{n_0} \right|^2 \tag{5-7}$$

in which $\frac{d\sigma}{d\Omega}$ is the differential scattering section describing the number of scattered photons per unit solid angle per unit time and Δn is the difference in refractive index between the aggregate and the medium. Usually, the density of particles is approximately uniform. Under such circumstance, the refractive index difference $\Delta n(\rho)$ can be taken out from under the integral in (5-7).

In deriving (5-7), we implicitly assume that the interaction between particles is weak, and the structure factor is almost unity. This assumption, together with that

underlying (5-5), means that (5-7) is suitable only for the study of self-assembly in dilute samples.

In static light scattering experiments, scattering intensities *I(Q)* are collected at different Q, from which the spatial distribution of the refractive index n(r) within the aggregates, and therefore the structure of particles can be obtained.

5.2.2 Dynamic Light Scattering

In static light scattering, we assumed that the collision interaction between photons and matters is elastic, in which the frequency or energy of a photon is the same before and after interactions. In reality, the medium molecules experience constant thermal movements, and thus collisions between photons and medium molecules are no longer elastic, and the photon experiences a frequency shift. We show below that this frequency shift provides us dynamic information on the behavior of the self-assembled aggregates.

Follow the same procedure as in the previous section, the scattered electric field can be expressed as[4],

$$E_s(R,t) = \frac{E_0}{4\pi R\varepsilon_0} e^{ik_f R} \int_V d^3 r e^{i(Q.r-\omega_f t)} \{n_f.[k_f \times (k_f \times (\delta\varepsilon(r,t).n_i)]\} \qquad (5\text{-}8)$$

where Q is the scattering wave vector, k_f is the wave vector of scattered beam, n_i is the unit vector along the incident wave polarization; n_f is the directional vector of the scattered wave polarization, and $\delta\varepsilon(r,t)$ is the dielectric constant fluctuation tensor.

Equation (5-8) can be further simplified by applying spatial Fourier transform of the dielectric fluctuation[4],

$$\delta\varepsilon(Q,t) = \int_V d^3 r e^{iQ.r} \delta\varepsilon(r,t) \qquad (5\text{-}9)$$

We then get[4],

$$E_s(R,t) = \frac{-k_f^2 E_0}{4\pi R\varepsilon_0} e^{i(k_f R-\omega_i t)} \delta\varepsilon_{if}(Q,t) \tag{5-10}$$

where $\delta\varepsilon_{if}(Q,t) = n_f.\delta\varepsilon(Q,t).n_i$ is the projection of the dielectric fluctuation tensor on the initial and final polarization directions.

In dynamic light scattering, the most important quantity is the scattered intensity time correlation function, which can be calculated from the scattered electric field in (5-10)[4],

$$I_{if}(Q,\omega_f,R) = \frac{I_0 k_f^4}{16\pi^2 R^2 \varepsilon_0^2} \frac{1}{2\pi} \int_{-\infty}^{+\infty} dt \left\langle \delta\varepsilon_{if}(Q,0)\delta\varepsilon_{if}(Q,t) \right\rangle e^{i(\omega_f-\omega_i)t} \tag{5-11}$$

where $I_0 = |E_0|^2$.

Equation (5-11) is proportional to the Fourier form of the autocorrelation function of the dielectric constant fluctuation[4],

$$I_{if}^{\varepsilon}(Q,\omega) = \frac{1}{2\pi} \int_{-\infty}^{+\infty} dt I_{if}^{\varepsilon}(Q,t) \tag{5-12}$$

where the autocorrelation function of the dielectric constant fluctuation is defined as[4],

$$I_{if}^{\varepsilon}(Q,t) = \left\langle \delta\varepsilon_{if}^{*}(Q,0)\delta\varepsilon_{if}(Q,t) \right\rangle \tag{5-13}$$

In dynamic light scattering, the measured $I_{if}^{\varepsilon}(Q,\omega)$ contains most of the dynamic information of the system. However, the exact form of $I_{if}^{\varepsilon}(Q,\omega)$ and the dynamic information it contains, are highly dependent on the details of the system. Here, we discuss in detail particle diffusion in a solvent, because it is the most popular case and is utilized in our study on micellar size.

Consider a system in which relatively large particles are suspended in a uniform solvent. The dielectric constant of the particles is much different with that of the solvent, so essentially all scattered light comes from the particles in the certain frequency range.

Under such circumstance, the autocorrelation function of the dielectric constant fluctuation is[4],

$$I_{if}^{\varepsilon}(Q,t) = (n_i.n_f)^2 a_p^2 NS(Q,t) \tag{5-14}$$

in which N is the number of particles in the system, a_p^2 is the polarizability of the particle, and n_i and n_f are the polarization directions of the incident and reflected waves, respectively. The important quantity in (5-14) is the dynamic form factor $S(Q,t)$[4],

$$S(Q,t) = \frac{1}{n^2}\left\langle \sum_{i,j} e^{iQ.[r_i(t)-r_j(0)]} \right\rangle \tag{5-15}$$

which contains the desired dynamic information pertaining to the particles.

The particles experience intensive collisions with solvent molecules and hence undergo a random walk process, which can be described in terms of translational diffusion. Under such circumstances[4],

$$S(Q,t) = \frac{N}{n^2} e^{-Q^2 Dt} \tag{5-16}$$

Therefore, from dynamic light scattering experiments, the diffusion coefficient of large particles can be measured, and the hydrodynamic radius of the particle can be calculated from Stokes-Einstein relation[4],

$$D = \frac{k_B T}{6\pi\eta a} \tag{5-17}$$

where a is the hydrodynamic radius, and η is the solvent viscosity.

Therefore, dynamic light scattering provides an effective method to measure the effective sizes of large particles, such as micelles.

5.2.3 Experimental Procedure

The light scattering experiments were conducted using a Brookhaven light scattering apparatus, which consists of the BI-200SM motor driven goniometer, the BI-9000AT digital autocorrelator, and the BI-9025AT photon counter. The laser light was provided by an Argon ion laser (Spectra-physics 2017-055), operated at either 488 nm or 514 nm.

The samples were first prepared at higher concentrations than those desired for the experiments, and were then filtered using a Millipore 0.45 μm MCE syringe-driven filter. The concentrations of the filtered samples were determined by measuring their UV-VIS absorbance at a specific wavelength of 326 nm and comparing with absorbance-concentration calibration curves. It was found that there was a significant loss of surfactant during filtering. This loss may be due to adsorption of surfactant on the filter surface, or due to large surfactant aggregate which cannot easily pass though the filter.

The self-assembly behavior in trans $C_4AzoOC_6E_2$ solutions was investigated by static and dynamic light scattering over the concentration range $1.720\times10^{-3} \sim 69.444\times10^{-3}$ mM.

5.2.4 Results

It was observed that trans $C_4AzoOC_6E_2$ has a strong tendency to form large aggregates, and even at concentrations as low as 0.1 mM, there were aggregates of size comparable with wavelength of visible light, ie., 500 nm, as indicated by the turbidity of the sample (Figure 5-4).

In the concentration range under investigation, as shown later, there is a series of structural evolutions with increasing concentrations, and several structural crossovers have been discovered in trans $C_4AzoOC_6E_2$. Its self-assembly shows an interesting polymorphism development, and we show below how this behavior can be detected experimentally and explained theoretically.

The concentration of the first sample was 1.720×10^{-3} mM, which was just above the CMC (1.01×10^{-3} mM). When experimental data were represented in the format of a Guinier plot ($\ln I(Q)$ vs Q^2), the expected linear behavior was not observed.

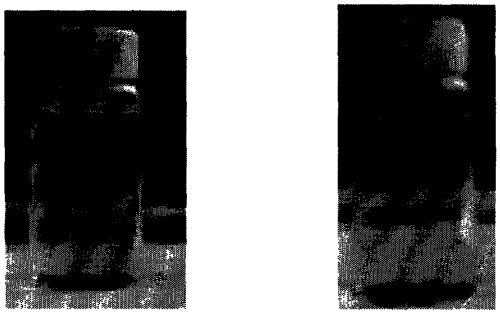

a b

Figure 5-4 Photographs of 0.1 mM solutions of $C_4AzoOC_6E_2$ (a) and $C_4AzoOC_4(NH_4)_3Br$ (b). Their extinction coefficients are approximately equal. The $C_4AzoOC_4(NH_4)_3Br$ solution is clear while the $C_4AzoOC_6E_2$ solution is turbid. The turbid $C_4AzoOC_6E_2$ solution indicates the appearance of large aggregates (several hundreds nanometers).

Because Guinier plots always give a straight line whenever the size of the aggregate is much smaller than the laser wavelength, the failure of linearity in the Guinier plots indicates that the size of the aggregates was relatively large. This was a little surprising, since normally at a concentration just above the CMC, surfactants self-assemble into spherical micelles with radius of several nanometers. However, in $C_4AzoOC_6E_2$, much larger aggregates than would be expected for spherical micelles appeared even at concentrations as low as 1.72×10^{-3} mM.

When scattering intensities were plotted in the format of $Q^2I(Q)$ vs Q, linear behavior was observed in the large Q range, which indicated a rod-like structure, as given by[5],

$$I(Q) \propto \frac{\pi}{QL} - \frac{2}{(QL)^2} \quad \text{i.e.,} \quad Q^2 I(Q) \propto \frac{\pi Q}{L} - \frac{2}{L^2} \tag{5-18}$$

in which L is the length of the rod.

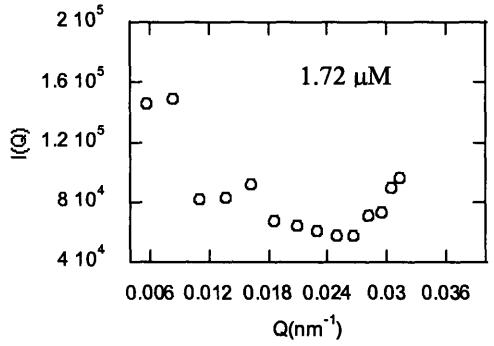

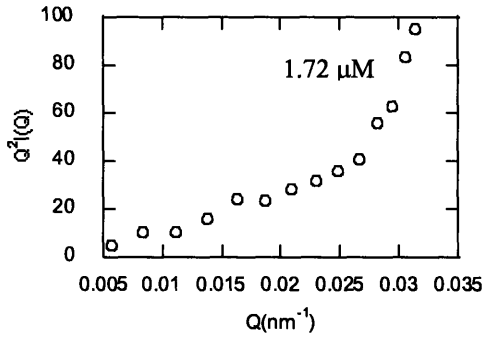

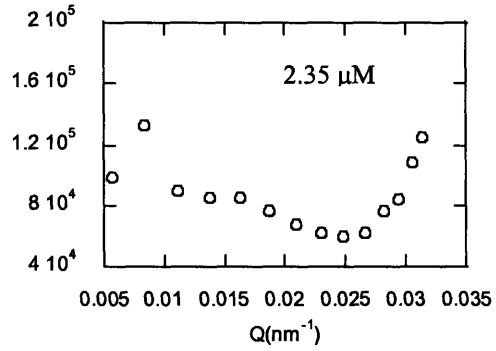

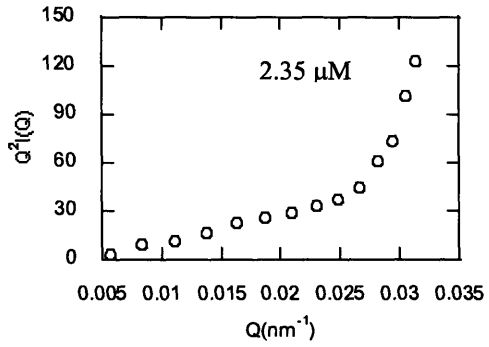

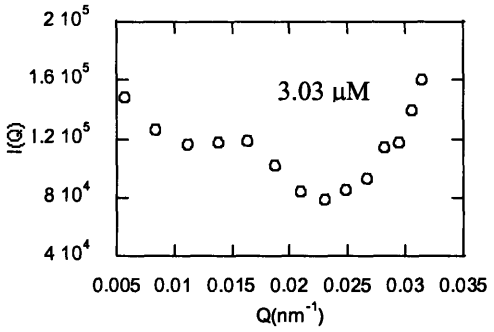

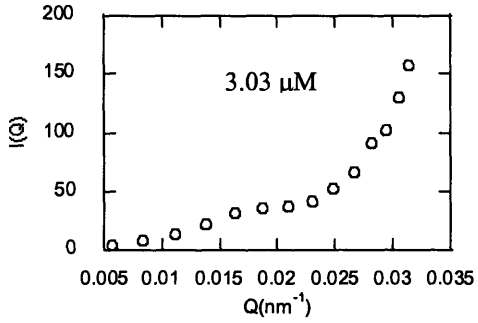

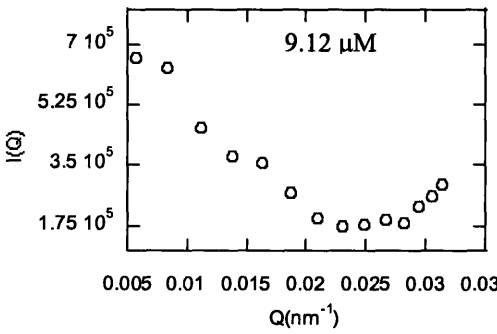

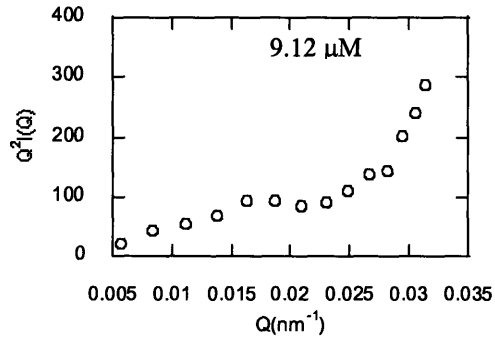

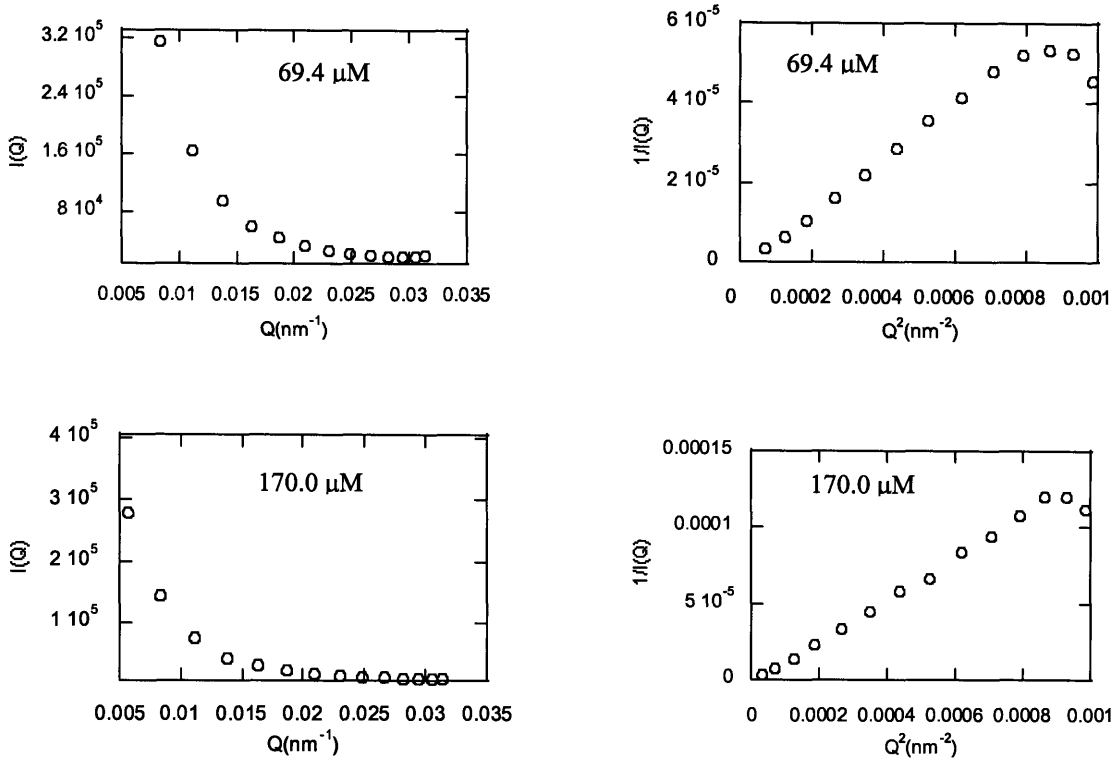

Figure 5-5 Experimental results of static light scattering in trans form of surfactant $C_4AzoOC_6E_2$ at various concentrations.

From (5-18), the length of rod is the ratio of the slope to the intercept in the $Q^2I(Q)$ *vs* Q plot. In this way, the length was found to be 26.6 nm, which just corresponded to the Q range of linear behavior.

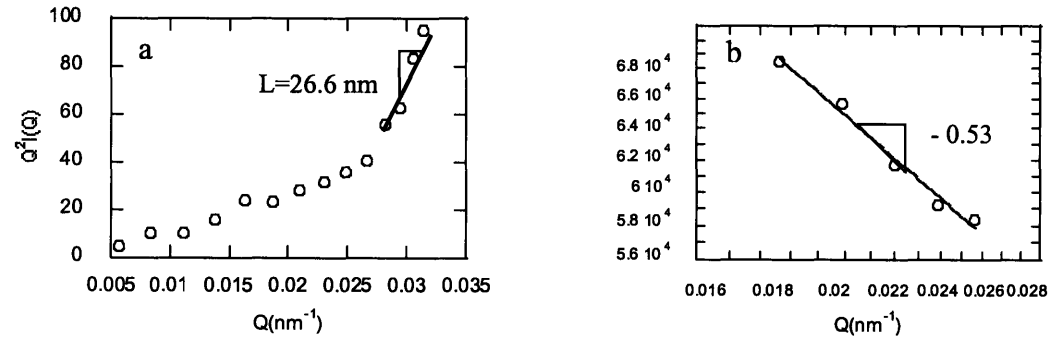

Figure 5-6 Light scattering results for trans C4AzoOC6E$_2$ at 1.720×10^{-3} mM (a) and power law behavior in the intermediate Q range (b).

More interestingly, in the low Q range, I(Q) showed a power law $I(Q) \propto Q^{-a}$ behavior with exponent $a = 0.53$. Since the scattering intensity at large Q describes the structure at small length scales, and vice versa, a tentative picture of the aggregate structure can be gleaned from the scattering curve. According to this picture, trans $C_4AzoOC_6E_2$ essentially self-assembled into long cylindrical micelles even at low concentrations. In contrast to flexible polymer coils, these long cylinders were fairly rigid and were characterized by a persistent length of about 26 nm. For length scales smaller than the persistence length, the micelle behaves exactly as rigid rods; for length scales far larger than the persistence length, micelles behave as flexible polymer coils. Therefore, we have the criteria,

Rigid rod, $l < l_p$

Gaussian coil, $l > l_p$

For the intermediate length scale, the spatial distribution of rigid rods is characterized by power law r^{a-3}, which can be obtained from scattering intensity in lower Q range from $I(Q) \propto Q^{-a}$ and a is the fractal dimension. The rod length found from light scattering corresponds to the persistence length, below which micelles behave like rigid rods. These rigid rods can be viewed as the basic structural units of the cylindrical micelles, which can be viewed as being constituted of many such structural units, with the spatial distribution of these structural units characterized by the power law at low Q range, in which the exponent is the fractal dimension. At a concentration of 1.720×10^{-3} mM, the a value of 0.53 implies that there were only a few rigid rods in the micelle, and the contour length of the micelle was not sufficiently long to lead to Gaussian coil like behavior.

At concentrations of 2.35×10^{-3} mM and 3.03×10^{-3} mM, similar light scattering results were obtained, as shown in Figure 5-7. The persistence length at each concentration was found to be 25.2 nm (2.35×10^{-3} mM) and 25.5 nm (3.03×10^{-3} mM), and the corresponding values of the exponent a were 0.85 and 1.23, respectively. The persistence lengths in both cases were close to each other and to that observed for the 1.72×10^{-3} mM solution. It was consistent with our picture of micellar structure, in which

the rigid rod was the basic structural unit with an unchanging persistence length. The exponent *a* increased with concentration, indicating micellar growth, since the larger *a* is consistent with there being the more rigid rods in cylindrical micelles.

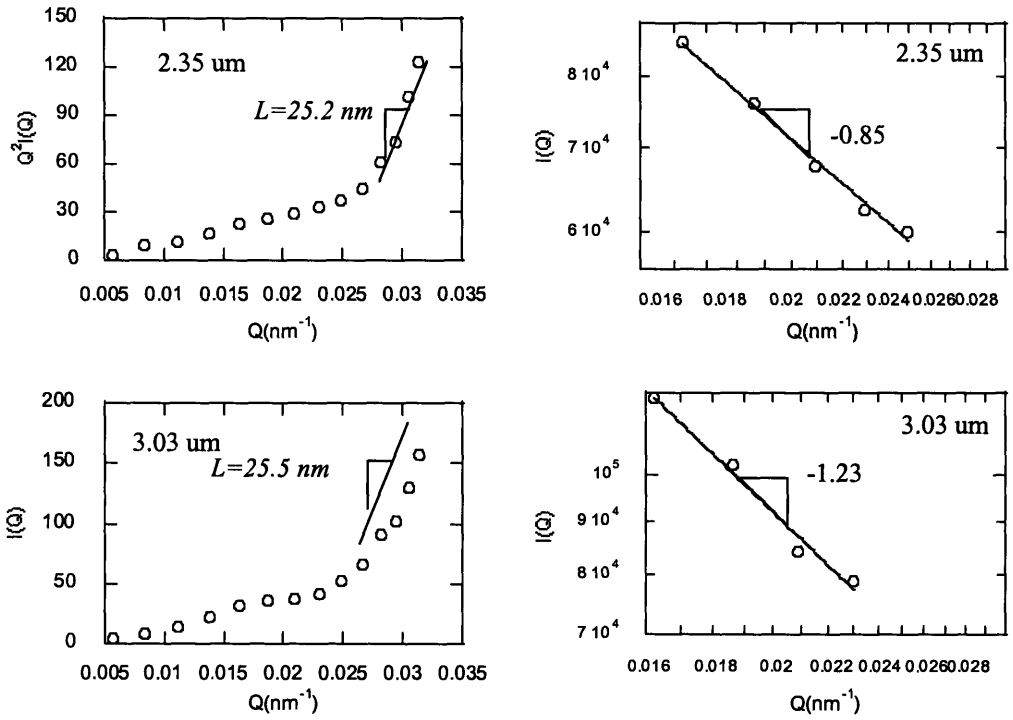

Figure 5-7 Light scattering results of trans C4AzoOC6E$_2$ at 2.35×10^{-3} mM and 3.03×10^{-3} mM, and their power law behaviors in the low Q range.

When the concentration was increased to 9.12×10^{-3} mM, a new feature developed in the scattering curve (Figure 5-8). Over the large Q range, there was still a straight line in the $Q^2I(Q)$ vs Q plot, in which the persistence length was calculated to be 25.6 nm, consistent with the persistence length found at the other concentrations. However, in the intermediate Q range, a plateau developed, which indicated the appearance of 2-dimensional object. The apparent discrepancy between the one dimensional rod in the large Q range and a two-dimensional object in the low Q range was reconciled by inferring the formation of a Gaussian coil, i.e., in which the basic structural unit was a rigid rod with persistent length about 25 nm, and the contour length of the cylindrical micelle was sufficiently long that the micelles possessed sufficient flexibility to form a Gaussian coil.

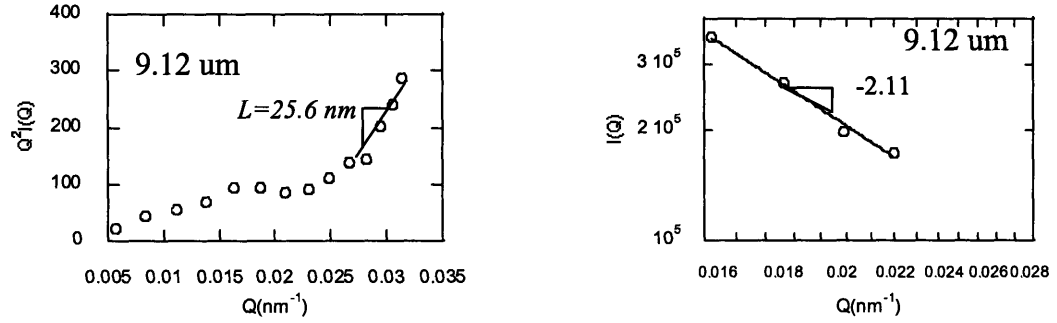

Figure 5-8 Light scattering results and power behavior in the low Q range of trans C4AzoOC6E$_2$ at 9.122×10^{-3} mM. Note there was plateau in the middle Q range

However, when the concentration continued to increase to 69.4×10^{-3} mM, a qualitatively different scattering curve was obtained (Figure 5-9 (a)), in which the $Q^2I(Q)$ curve decreased instead of increasing as Q increased in the low Q range. It seemed that the previous micellar picture was no longer applicable to this situation. However, if the scattering intensities are plotted in the form of $1/I(Q)$ vs Q^2, a perfect straight line is obtained over most of the Q range, as shown in Figure 5-9 (b). Normally, this type of behavior indicates the appearance of a Debye-type correlation with finite correlation length, which can be mostly described by the Debye function,

$$G(r) = \frac{\xi}{r} e^{-\frac{r}{\xi}} \tag{5-19}$$

in which ξ is the correlation length. From the Debye correlation function, the scattering intensity is calculated as[5],

$$I(Q) = A\frac{\phi^2\xi^2}{1+Q^2\xi^2} \tag{5-20}$$

in which ϕ is the volume fraction of micelles, and A is a constant.

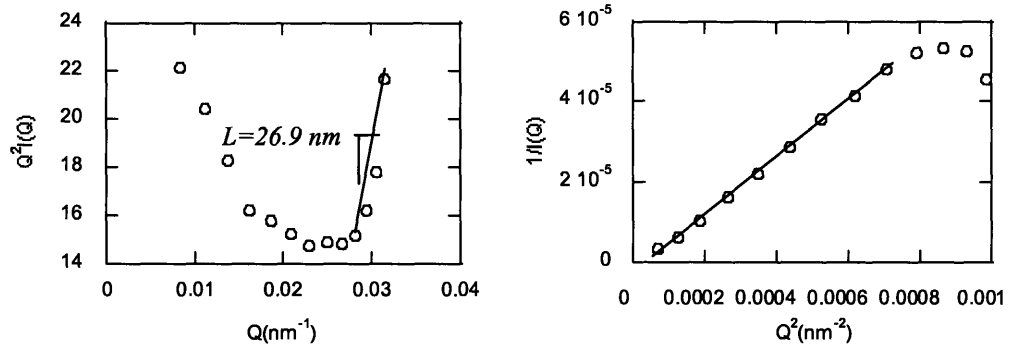

(a) (b)

Figure 5-9 Light scattering results of trans $C_4AzoOC_6E_2$ at 69.4×10^{-3} mM plotted in the format of $Q^2I(Q)$ *vs* Q (a) and $1/I(Q)$*vs* Q^2 (b).

In the system characterized by the Debye correlation function, the plot of $1/I(Q)$ vs Q^2 was a straight line, as shown in Figure 5-9 (b). However, a more careful inspection on Figure 5-9 (b) revealed that the intercept was negative, in contradiction to the term of Debye correlation function, where the intercept of 1/I(Q) curve with y axis is always positive.

A system that demonstrates Debye-type correlation and yet possesses a negative y-axis intercept is that of a branched polymer solution. It was found theoretically that the scattering intensity from a branched polymer solution is described by the equation (5-21)[5],

$$\frac{1}{I(Q)} \propto \frac{3-m}{4M_0} + \frac{Q^2\bar{l}^2 z}{12M_0} \qquad (5\text{-}21)$$

in which m is the number of branches, z is the number of segments in each branch, $\bar{l}^2$ is the average of the square of the length of segments, and M_0 is the molecular weight of a single branch. Equation (5-21) gives a straight line in the plot of $1/I(Q)$ vs Q^2, and the intercept is negative for $m > 3$. The scattering curve for 69.4×10^{-3} mM was fitted very well by (5-21). Therefore, it can be concluded that, at 69.4×10^{-3} mM, surfactants self-

assemble into branched cylindrical micelles, in which the average branch number is larger than 3.

When the system concentration was increased further to 170.0 $\times 10^{-3}$ mM, the scattering intensity showed similar behavior, as shown in Figure 5-9. The scattering curve again showed linear behavior in the *1/I (Q)* vs Q^2 plot, and with a negative intercept, again implying branched micelles.

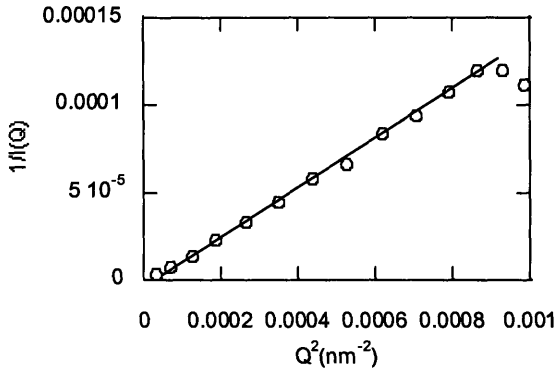

Figure 5-10 Light scattering results of trans $C_4AzoOC_6E_2$ at 170.0×10^{-3} mM plotted in the format of *1/I(Q)vs* Q^2.

The results of the static light scattering studies are summarized in Figure 5-10. Over the concentration range under study, surfactants self-assembled into cylindrical "worm–like" micelles with finite persistence length. The worm-like micelle can be viewed as being constituted of basic structural units, rigid rods, with length given by the persistence length. As shown in Figure 5-11, the persistence length was almost constant over three concentration decades, consistent with the picture of worm-like micelles in which the persistence length is independent of concentration. Similarly, with increasing the concentration increases, the fractal dimension of the micelles, which quantitatively describes the spatial distribution of "rigid rods", increased rapidly with concentration at the beginning, and reached a plateau at high concentrations. It indicates a "micellar growth" phenomenon, in which, with increasing concentration, more and more surfactants incorporate into existing micelles to minimize the overall free energy of the system. At low concentrations, micellar growth led to the appearance of more rigid rods

in the individual cylindrical micelles, as indicated by the increase in fractal dimension. When the cylindrical micelle was sufficiently long, it acquired sufficient flexibility to curve into a Gaussian coil, whose fractal dimension is exactly 2. Further increases in concentration lead to elongation of the contour length of the micelle, with retention of the Gaussian coil structure still a constant fractal dimension of 2 at concentrations above 0.01 mM.

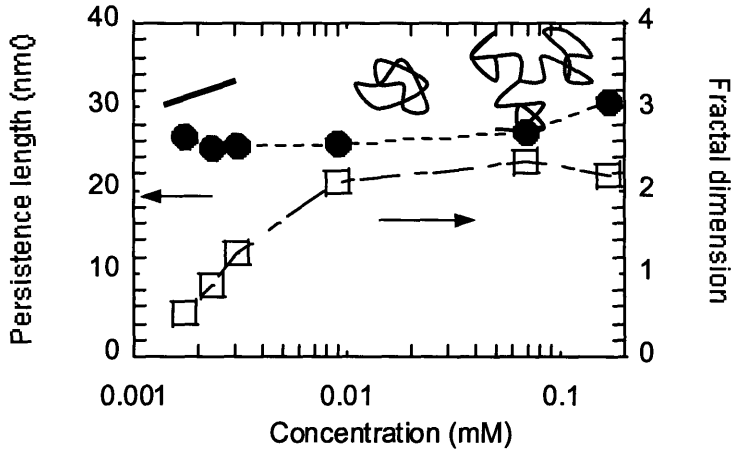

Figure 5-11 Summary of static light scattering (SLS) results on trans $C_4AzoOC_6E_2$. The y-axis at left-hand side represents the persistence length (solid circle). The y-axis at right-hand side is the fractal dimension (square). Above the curve, the aggregate structures are shown in the order of rigid rod, Gaussian coil, and branched coil, each located at the corresponding concentration range.

The "micellar growth" phenomenon in trans $C_4AzoOC_6E_2$ was further verified by dynamic light scattering, as shown in Figure 5-12. At low concentration, the hydrodynamic radius of the micelle increased rapidly with concentration, consistent with elongation of the "straight" cylinder, in which the micellar length was proportional to the number of surfactants inside it. However, for concentrations above 0.01 mM, which corresponded to formation of Gaussian coils as inferred from the SLS results, the increase in hydrodynamic radius with concentration was considerably slower. This was consistent with the Gaussian coil picture, in which the size of Gaussian-like micelles varies with the square root of the number of surfactants inside it. As the sequence, the increase in

hydrodynamic radius at higher concentration was much slower than those at low concentration.

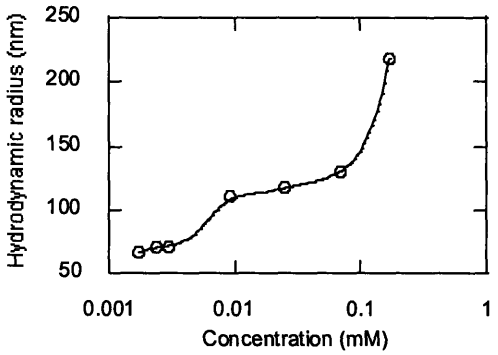

Figure 5-12 Results of Dynamic light scattering (DLS) study on trans $C_4AzoOC_6E_2$.

5.2.5 Theoretical Analysis of Light Scattering Results

The light scattering results indicated that "micellar growth" occurred for trans $C_4AzoOC_6E_2$. In this subsection, we apply established molecular thermodynamic theory to analyze the observed micellar growth phenomena. First, we give a brief introduction to the molecular thermodynamic explanation of "micellar growth". Second, we analyze our experimental results based on this theory, especially, the appearance of rod-like micelles at low concentration. In addition, we point out the possibility of the formation of vesicles from the closing up of disk-like micelles, which will be verified by SANS at high concentration.

5.2.5.1 Molecular Thermodynamic Explanation on Micellar Growth

The notable phenomenon of "micellar growth", in which both the size and shape of the micelle vary with the concentration, can be neatly enunciated by a simple molecular thermodynamic theory, according to which the micelles of various shapes can be described by well-defined geometries. Cylindrical micelles, for instance, can be viewed as cylinders capped at each end, as shown in Figure 5-13. The standard

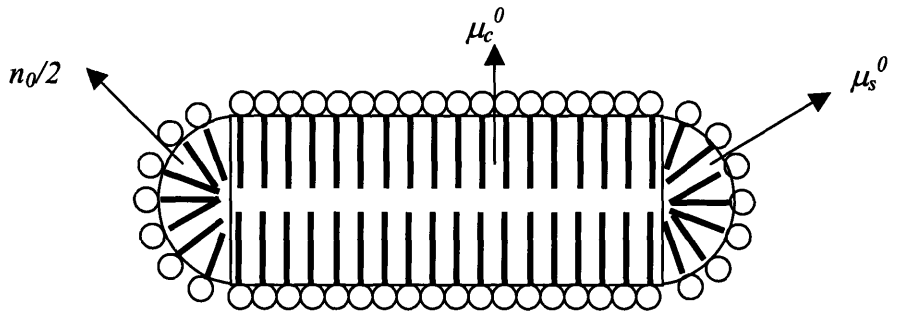

Figure 5-13 Schematic picture of cylindrical micelle. The micelle consists of one cylindrical rod and two spherical caps. μ_c^0 is the standard chemical potential per monomer in the cylinder, which is negative. μ_s^0 is the standard chemical potential per monomer in spherical cap, which is negative too. n_0 is the number of surfactants in the spherical caps.

chemical potential of the cylindrical micelle of size n is the sum of the standard chemical potentials of the spherical caps and the cylindrical rod[6],

$$\mu_n^0 = n\tilde{\mu}_n^0 = n_0\mu_s^0 + (n-n_0)\mu_c^0 \tag{5-22}$$

Equation (5-22) can be rearranged to produce following equivalent form[6],

$$\tilde{\mu}_n^0 = \mu_c^0 + \frac{\frac{n_0(\mu_s^0 - \mu_c^0)}{kT}kT}{n} = \mu_c^0 + \frac{\alpha_c kT}{n} \tag{5-23}$$

in which α_c is the "growth factor". It is the difference in standard chemical potential between spherical and cylindrical geometries.

The standard chemical potential of a cylindrical micelle can be summarized by,

$$\tilde{\mu}_n^0 = \begin{cases} +\infty, & \text{for } 1<n<n_0 \\ \mu_\infty^0 + \dfrac{\alpha_c kT}{n}, & n \geq n_0 \end{cases} \tag{5-24}$$

in which n is the size of micelles, and n_0 is the number of surfactants in spherical caps. From geometrical considerations, when n is smaller than n^0, it is impossible to form micelles. Therefore, for $1<n<n^0$, the micelle standard chemical potential is set to infinity to prohibit the formation of such micelles.

Qualitatively, the standard chemical potential in the spherical cap is higher than in the cylindrical rod, because surfactants pack more closely in the cylinder than the sphere, and as a result, the hydrophobic effect made the cylindrical packing to be more energetic stable than the spherical packing. Therefore, if entropy penalty is not so serious, surfactants tend to elongate the existing cylindrical rod rather than to form new spherical micelles, the cylindrical micelle will become longer and longer. This is the "micellar growth" phenomenon. Normally, at the concentration just above the CMC, surfactants self-assemble into spherical micelles. At the still higher concentrations, when the standard chemical potential difference can compensate for the loss of the translational entropy, surfactants will self-assemble into the cylindrical micelles.

The above argument can be made quantitative through self-assembly theory. Quantitatively, let XCMC denote the mole fraction of the Critical Micellar Concentration (CMC) at which spherical micelles begin to form, and X denote any surfactant mole fraction close to XCMC. Because the surfactant concentration is low, the number of surfactant molecules in the solution is roughly XNw, where Nw is the number of water molecules in the solution. The system free energy in the spherical micelle system is,

$$\mu_n^s = N_m \mu_s^0 + \frac{N_m}{n_0} kT \ln \frac{N_m}{n_0} \tag{5-25}$$

where n_0 is the aggregation number in the spherical micelle; N_m is the total number of self-assembled surfactant, $(X\text{-}X_{CMC})N_w$. However, if surfactants self-assembled into cylindrical micelles with size n, the system free energy is,

$$\mu_n^c = N_m \tilde{\mu}_n^0 + \frac{N_m}{n} kT \ln \frac{N_m}{n} = N_m (\mu_c^0 + \frac{\alpha_c}{n} kT) + \frac{N_m}{n} kT \ln \frac{N_m}{n} \tag{5-26}$$

The free difference between cylindrical and spherical micellar system is,

$$\mu_n^c - \mu_n^s = \frac{N_m kT}{n_0}[(\frac{n_0}{n} - 1)\alpha_c - (\frac{n_0}{n} - 1)\ln\frac{N_m}{n_0} - \frac{n_0}{n}\ln\frac{n_0}{n}] \tag{5-27}$$

Under circumference when n is close to n_0, $n = n_0(1+\Delta n)$, then Eq (5-27) can be simplified by,

$$\mu_n^c - \mu_n^s = -\frac{N_m kT}{n_0}\Delta n(\alpha_c - \ln\frac{N_w}{n_0} - 1) \tag{5-28}$$

, and the corresponding condition when cylindrical micelles are preferred, is,

$$\alpha_c - \ln\frac{N_w}{n_0} - 1 > 0 \tag{5-29}$$

Substituting $N_m = (X\text{-}X_{CMC})N_w$ and $X_{CMC} = \exp(\frac{\mu_s^0 - \mu_1^0}{kT})$ into Eq (5-29), this condition can be rewritten as,

$$\Delta X > \frac{n_0}{N_W} e^{-[\alpha_c - \frac{\mu_s^0 - \mu_1^0}{kT}]} \tag{5-30}$$

where $\Delta X = X\text{-}X_{CMC}$; μ_s^0 is the standard chemical potential per surfactant in spherical micelle; μ_1^0 is the standard chemical potential of monomer surfactant.

Therefore, ΔX will become negligible small when

$$\alpha_c > \frac{\mu_s^0 - \mu_1^0}{kT} \tag{5-31}$$

the concentration range for spherical micelles is almost negligible. As a consequence, it seems that the cylindrical micelles must appear just above the CMC, as was observed experimentally.

Similar considerations can be applied to disc-like micelles, too. The disc-like micelle consists of a disk and a semi-cylindrical rim, in which the standard chemical potential per monomer in the disk is lower than that in the rim. Therefore[6],

$$\mu_n^0 = n\tilde{\mu}_n^0 = n_c\mu_c^0 + (n - n_c)\mu_d^0 \tag{5-32}$$

in which n_c is the number of surfactants in the rim, n is the number in the micelle, μ_c^0 is the standard chemical potential per monomer in the cylindrical rim, and μ_d^0 is the standard chemical potential per monomer in the disk.

Equation (5-32) can be cast into the form of (5-23)[6],

$$\tilde{\mu}_n^0 = \mu_\infty^0 + \frac{\alpha_d kT}{n^{1/2}} \tag{5-33}$$

in which $\mu^0_\infty = \mu^0_d$, and $\alpha_d = (\mu^0_c - \mu^0_d)/kT$.

In case of the rod-to-disk transition, the situation is a little more complicated because the size distribution of rod-like micelles is broad rather than mono-dispersed as in spherical micelles. The size distributions in both rod-like and disk-like micelles can be calculated based on Eq (5-23), (5-33) and the molecular thermodynamic formula presented in Chapter 1. According to Chapter 1, the equilibrium molar fraction of size s-mer X_m is

$$X_m = \exp(-m\frac{\tilde{\mu}_m^0 - \mu}{k_B T}) \tag{5-34}$$

where $\tilde{\mu}_m^0$ is the standard chemical potential per surfactant in m-mer; μ is the chemical potential of the monomer surfactant in bulk phase. Substituting Eq (5-23) and (5-33) into Eq (5-34), the size distribution in rod-like and disk-like micelles are,

$$X_m^c = \exp-(m\beta_c + \alpha_c)$$

and (5-35)

$$X_m^d = \exp-(m\beta_d + \alpha_d m^{1/2})$$

where X_m^c and X_m^d are molar fraction of m-mer of rod-like and disk-like micelles, respectively; α_c and α_d are the growth factors of rod-like and disk-like micelles, respectively; β_c and β_d are the constant in the rod-like and disk-like micelle systems, respectively. As can be seen from Eq (5-35), the size distribution of disk-like micelles is much narrower than rod-like micelles because of the $m^{1/2}$ term in the exponent of X_m^d. As a result, the entropy in rod-like micellar system is higher than that in disk-like micellar system. It is the "entropy barrier" that has to be overcome in the rod-to-disk transition.

The free energies in rod-like and disk-like micellar systems are

$$X^2 N_w \mu_c^0 - X^2 N_w \beta_c k_B T$$

and (5-36)

$$XN_w \sum_s e^{-\beta_d s - \alpha_d s^{1/2}} \left[s(\mu_d^0 - \beta_d k_B T) - \alpha_d k_B T s^{1/2} - \alpha_d k_B T s^{-1/2} \right]$$

, respectively. For X satisfies,

$$X > \frac{\sum_s e^{-\beta_d s - \alpha_d s^{1/2}} \left[s(\mu_d^0 - \beta_d k_B T) - \alpha_d k_B T s^{1/2} - \alpha_d k_B T s^{-1/2} \right]}{\mu_c^0 - \beta_c k_B T} \quad (5\text{-}37)$$

, the free energy in disk-like micellar system is lower than that in the rod-like micellar system. As a consequence, when adding more surfactants, the rod–like micelles no longer elongate and the disk-like micelles begin to appear. The relation between chemical potential per surfactant with aggregation number n is schematically summarized in Figure 5-14.

"Micellar growth" in disk-like micelles can also occur. Because the free energy in the rim is higher than that in the disk, following the same argument as used in the cylindrical micelle case, when more surfactants are added to the solution, most of them are incorporated into the disk. Therefore, the radius of the disk-like micelles increases

with concentration. However, the radius cannot increase indefinitely. It may be expected that the disk-like micelle will fluctuate in curvature, and can close up to form vesicles when the radius increases to a critical value R_c, at which the free energy cost in bending is totally compensated for by the elimination of high energy rims. The critical value R_c can be estimated from the simple criterion,

$$\frac{1}{2}\kappa(\frac{2}{R_c})^2 < 2\pi R_c \lambda \tag{5-38}$$

in which κ is the bending rigidity of the surfactant membrane, and λ is the "line tension" of the disk which is another representation of the chemical potential of the surfactants in the high energy rim.

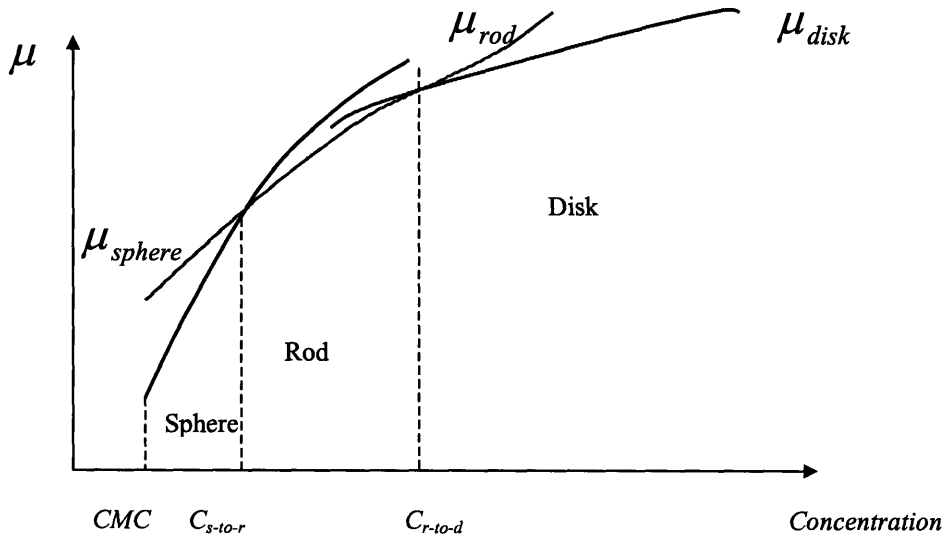

Figure 5-14 The schematic variation of chemical potential per surfactant with concentration in various packing geometry. CMC is the critical micellar concentration; $C_{s\text{-}to\text{-}r}$ is the sphere-to-rod transition concentration; $C_{r\text{-}to\text{-}d}$ is the rod-to-disk transition concentration. μ_{sphere}, μ_{rod}, and μ_{disk} are the chemical potentials of spherical, rod-like, and disk-like micelles, respectively

From equation (5-38), when

$$R_c > \sqrt[3]{\frac{\kappa}{\lambda\pi}} \tag{5-39}$$

disk-like micelles will close up to form vesicles. The energy for bending was provided by high-energy rim. It was concluded that the vesicles appear in the solution at sufficiently high concentrations. As shown later in our SANS study, vesicles were indeed found in trans $C_4AzoOC_6E_2$ solutions at concentrations higher than those that could be studied by light scattering.

5.2.5.2 Analysis of Light Scattering Results

The photoresponsive surfactant $C_4AzoOC_6E_2$ possesses several structural features distinct from regular surfactants. The most relevant is the azobenzene group in the tail. Because of the two benzene rings and associated large π-orbitals, the intermolecular interaction between azobenzenes is highly orientation dependent through π-π interactions[7]. Detailed quantum mechanical studies show that the π-π interaction is strongest when two azobenzene groups are oriented in parallel, and weakest when azobenzenes are perpendicular to each other. The relative orientation between two azobenzene groups can be characterized by the angle β between their normals. When the angle β is zero, the two azobenzene groups are parallel to each other, and have the strongest interaction. When the angle β is 90°, the two azobenzene groups are perpendicular to each other, and the π-π interaction is the weakest.

The existence of π-π interactions introduces many unusual properties to trans $C_4AzoOC_6E_2$ micelles, since they can cause significant differences in packing geometry. In the spherical micelle, each surfactant molecule is actually confined in a cone–like volume, the β angle between two azobenzenes is large, and therefore the interaction is weak. When in the cylindrical micelle, β is smaller, and the intermolecular interaction is stronger. However, in the disc–like micelle, β is almost zero, and the π-π interactions are close to their maximum. Thus, in $C_4AzoOC_6E_2$, following the packing geometry in the order of the sphere, the cylinder, and the disc, the free energy was lowered not only by the hydrophobic effect but also by the increased magnitude of the attractive π-π

interactions. As a consequence, the growth factors α_c in (5-23) and α_d in (5-33) are much larger than in surfactants without azobenzene groups. The larger "growth factor" indicates that azobenzene-containing surfactants have a stronger preference to form cylindrical and disc-like micelles. Under these circumstances, it is reasonable to assume that equation (5-31) is satisfied. This conclusion is consistent with experimental observations on the self-assembly behavior of $C_4AzoOC_6E_2$, in which cylindrical micelles were found even at concentrations just above the CMC. The second consequence of the large growth factor is the strong tendency towards micellar growth, also consistent with experimental observations. As shown in Figure 5-8 and Figure 5-9, the length of the cylindrical micelle increased dramatically with concentration, as indicated by both the fractal dimension and the hydrodynamic radius of the aggregates. In the concentration range that studied by light scattering, the disk-like micelles were not observed. However, at higher concentrations, the vesicle-like aggregates were found from SANS, which are actually the "close up" version of disk-like micelles. It is consistent with our analysis.

In summary, because of the orientation-dependent π-π interactions in azobenzene systems, the strength of the interaction between $C_4AzoOC_6E_2$ molecules continuously increases when packed in the spherical, cylindrical, and disc micelles, respectively. It leads to large growth factors α_c and α_d in $C_4AzoOC_6E_2$ micelles, which favor the formation of small curvature micelles such as cylinders and discs, and induces the strong tendency for micellar growth.

5.3 Small Angle Neutron Scattering (SANS) Study

Neutrons are a good probe to investigate self-assembled structures with atomic resolution[8]. In addition to the high spatial resolution, the "contrast variation" technique makes SANS a valuable and versatile approach for probing their structures[8]. The large difference in "scattering capability" between hydrogen and deuterium can be used to select any specific moiety in the surfactant to be highlighted by deuteration, which means that only the deuterated part is visible under neutron illumination. Through selective deuteration of different moieties, a comprehensive structural characteristization can be

attained with high resolution. A disadvantage of SANS experiments, however, is that, in comparison with photons, the scattering of neutrons is very weak. Therefore, to collect sufficient neutron counts to acquire reliable signal/noise ratios within a reasonable period, there must be sufficient aggregates in the sample. Therefore, SANS is only applicable for the study of concentrated samples.

In this section, we present a detailed SANS study on self-assembling behavior in $C_4AzoOC_6E_2$ under both UV and visible illumination. It was found that there are significant differences in SANS spectra between trans and cis forms. Complementary to the SANS study, images of self-assembling aggregates, which were taken using cryo-TEM ("replica" and "vitrified ") are shown to support our analysis of SANS spectra.

5.3.1 Theory of SANS

Consider an incident neutron beam $\psi_i(z,t) = \frac{1}{\sqrt{V}} e^{i(k_i z - \omega_i t)}$, which is scattered by N nuclei. According to quantum theory of scattering, the scattered neutron wave at a large distance from the scatterers has the form,

$$\psi_s(r,t) = f(\theta, k_i) \frac{e^{i(k_i r - \omega_i t)}}{r} \tag{5-40}$$

where r is the distance from the origin to the detector situated at a scattering angle θ, and $f(\theta,k_i)$ is the scattering amplitude.

If the neutron is scattered by one nucleus having a scattering length b_j located at R_j, the scattered wave is,

$$\psi^j{}_s(r,t) = -b_j e^{ik_i \cdot R_i} \frac{e^{ik_s|r-R_j| - i\omega_i t}}{|r-R_j|} \approx -b_j e^{iQ \cdot R_j} \frac{e^{i(k_i r - \omega_i t)}}{r} \tag{5-41}$$

where $\boldsymbol{Q} = \boldsymbol{k_i} - |k_i|\boldsymbol{r}$ is the scattering vector ($\boldsymbol{r}$ is the unit vector in the radial direction); b_j is the scattering length that characterizes the strength of interaction between neutron and nucleus.

For scattering by N nuclei,

$$\psi_s(r,t) = \sum_j -b_j e^{iQ.R_j} \frac{e^{i(k_i r - \omega_i t)}}{r} \tag{5-42}$$

from which $f(\theta, k_i) = \sum_j -b_j e^{iQ.R_j}$.

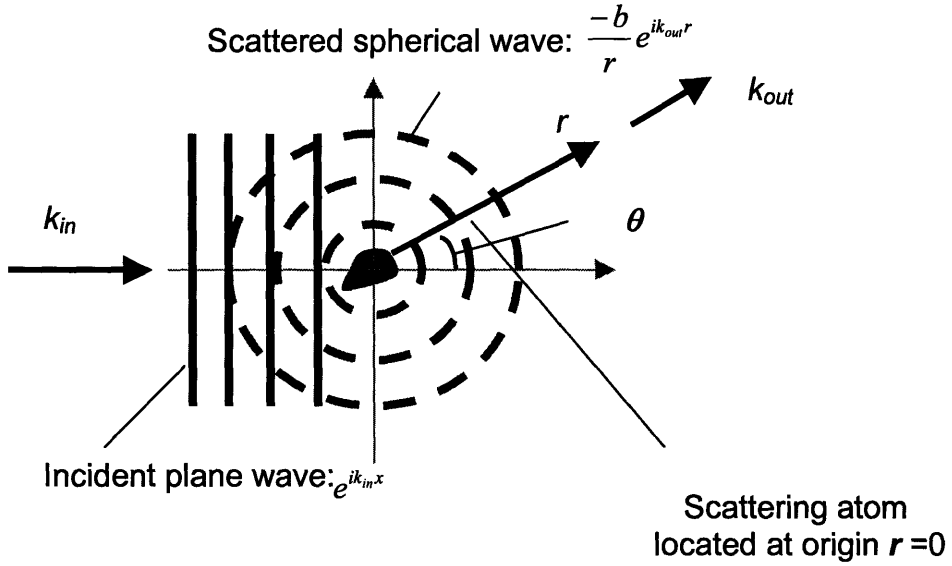

Figure 5-15 Schematic set up of neutron scattering experiment. k_{in} and k_{out} are the wave vectors of incident wave and scattered wave, respectively. θ is the scattering angle.

The differential cross section per unit solid angle is defined as

$$\frac{d\sigma}{d\Omega} = \frac{k_f |\psi_s|^2 r^2}{k_i |\psi_i|^2} = f^*(Q) f(Q) \tag{5-43}$$

in which k_f is the amplitude of scattered wave vector, and k_i is amplitude of incident wave vector.

After substituting (5-42) into (5-43)[8],

$$\frac{d\sigma}{d\Omega} = \sum_i \sum_j b_i b_j e^{iQ\cdot(R_i - R_j)} \tag{5-44}$$

For the system at equilibrium, the measured intensity is actually the ensemble average of (5-44), i.e.,

$$\frac{d\sigma}{d\Omega} = \left\langle \sum_i \sum_j \overline{b_i b_j} e^{iQ\cdot(R_i - R_j)} \right\rangle \tag{5-45}$$

The above ensemble average consists of two parts: first, an average over the distribution of nuclei over various spin and isotopic states; second, over the distribution of particle positions in the system.

Under the assumption that the distribution over the spin and isotopic states is uncorrelated, the first average is,

$$\overline{b_i b_j} = b_{inc}^2 \delta_{ij} + b_{coh}^2 \tag{5-46}$$

in which $b^2{}_{inc} = \overline{b^2} - \bar{b}^2$ and $b_{coh} = \bar{b}$.

Therefore, the scattering intensity can be divided into two parts,

$$\frac{d\sigma}{d\Omega} = N b_{inc}^2 + b_{coh}^2 \left\langle |f(Q)|^2 \right\rangle \tag{5-47}$$

in which only the second term on the right-hand side includes the structural information.

For a solution of large particles, the coherent scattering intensity can be factored into[5]

$$\frac{d\Sigma_{coh}}{d\Omega}(Q) = nP(Q)S(Q) \tag{5-48}$$

where $\frac{d\Sigma_{coh}}{d\Omega}$ is the differential scattering cross section per unit solid angle per unit volume, and n is the number density of particles. $P(Q) = |F(Q)|^2$ is the form factor with $F(Q) = \int_{particle} d^3 r e^{iQ.r}[\rho_i(r) - \rho_s]$, where $\rho_i(r)$ is the scattering length density distribution within the particle, and ρ_s is the scattering length density of solvent. $S(Q)$ is the structure factor, $S(Q) = \frac{1}{N_p}\sum_i \sum_j \left\langle e^{iQ.(R_i - R_j)} \right\rangle$. In dilute solutions, $S(Q)$ is essentially 1.

5.3.2 SANS Results and Discussion

Neutron scattering intensities in $C_4AzoOC_6E_2$ were measured on the NG3 30 m SANS line at the National Institute of Standards and Technology (NIST) in Gaithersburg, MD. An unpolarized neutron beam with a wavelengths 6 Å (wavelength spread $\Delta\lambda/\lambda \sim 0.11$) was used in all experiments. The sample with D_2O as solvent was loaded in quartz cells with path length 5 mm. The scattering experiments were conducted at two sample-to-detector distances, 1.33 and 7 m, with a lateral detector offset of 0.25 m. The Q range covered in the experiment was $0.005 < Q < 0.4$ Å^{-1}. The scattering intensity on the detector was circularly averaged for each scattering angle because the sample was observed to be isotropic. Scattering from the empty cell was subtracted, assuming that it was the same as the measured scattering from an identical empty cell. The absolute scattering intensity was obtained by using the standards and software supplied by NIST. Trans samples were measured under ambient light environment. For cis samples, the solution was first illuminated under UV light (Oriel 6283) for 2 hours to assure all trans was converted to the cis form, then the sample was loaded into the sample holder in the tank, in which a small UV lamp was mounted to provide necessary UV illumination during experiments. During the measurements, the tank was covered by its lid to prevent intrusion of ambient light.

Typical SANS spectra of both trans and cis samples are shown in Figure 5-16. It is evident that there are significant differences in the scattering profiles for the two

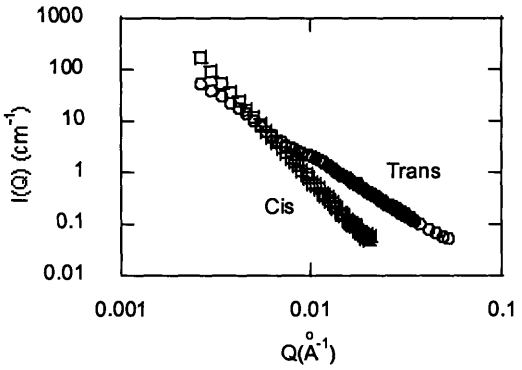

Figure 5-16 The SANS spectrum of surfactant $C_4AzoOC_4E_2$ at 0.7 mM

isomers. Scattering intensities by trans sample were larger than cis at high Q, while at low Q they were lower. These significant differences in SANS intensities suggest that the self-assembling behavior may be quite different for the two isomers.

5.3.2.1 Model Fitting

Quantitative structural information can be extracted from the SANS spectra through the fitting of appropriate models to the data. In this section, we present the results of model fitting on SANS spectra for both trans and cis samples.

SANS intensities in trans samples were found to be well described by the polydispersed core-shell model, in which the core has a well-defined distribution in sizes and the thickness of the shell is fixed. In the fitting, by setting the core SLD ρ_c equal to that of the solvent and the shell SLD ρ_s equal to that of the surfactants, the aggregates were effectively assumed to be vesicles.

In general, for a single core-shell structure with core radius r_c and shell thickness Δ, whose SLD distribution can be approximated by

$$\rho(r) = \begin{cases} \rho_c, & r \le r_c \\ \rho_s, & r_c < r \le r_c + \Delta \end{cases}$$

the form factor is [9],

$$P(x) = |F(x)|^2 = \left| \frac{4\pi}{Q^3}(\rho_s - \rho_c)\{\gamma j(x + \delta x) - j(x)\} \right|^2 \quad (5\text{-}49)$$

in which x is the dimensionless variable Qr_c, $\delta = \Delta/r_c$, $\gamma = (\rho_m - \rho_s)/(\rho_c - \rho_s)$, and the function $j(x) = sinx - xcosx$. In our model, only the shell scattered neutrons and therefore $\gamma = 1$.

The polydispersity in core size was described by the Schultz distribution, in which the normalized distribution function is defined as [10],

$$G(r_c) = \frac{r_c^z}{\Gamma(z+1)}\left(\frac{z+1}{\bar{r}_c}\right)^{z+1} \exp\left[-\frac{r_c}{\bar{r}_c}(z+1)\right] \quad (5\text{-}50)$$

where $\bar{r}_c$ is the mean core radius, and $z = (1-s^2)/s^2$ with $s = \frac{\sigma}{\bar{r}_c}$ (σ^2 is the variance of the distribution).

The Schultz distribution skews towards large sizes for finite z, and asymptotically approaches the Gauss distribution with increasing z; in the limit $z \to \infty$, it tends to the delta function.

The form factor in the system must be averaged over the size distribution, i.e.,

$$\bar{P}(Qr_c) = \int_0^\infty G(r_c)P(Qr_c)dr_c \quad (5\text{-}51)$$

Finally, the explicit size-averaged form factor for Schulz-distributed core-shell spheres is[9],

$$\bar{P}(x) = \frac{16\pi^2}{q^6}(\rho_s - \rho_c)^2\left\{c_1 + c_2\bar{x} + c_3\bar{x}^2\left(\frac{z+2}{z+1}\right) + B(\bar{x})^{(z+1)/2}(c_4\cos[(z+1)D(\bar{x})]\right.$$

$$\left. + c_7\sin[(z+1)D(\bar{x})]) + \bar{x}B(\bar{x})^{(z+2)/2}(c_5\cos[(z+2)D(\bar{x})] + c_8\sin[(z+2)D(\bar{x})]\right)$$

$$+\left(\frac{z+2}{z+1}\right)\bar{x}^{2}B(\bar{x})^{(z+3)/2}\left(c_6\cos[(z+3)D(\bar{x})]+c_9\sin[(z+3)D(\bar{x})]\right)\Big\} \qquad (5\text{-}52)$$

where the functions $B(\bar{x})$ and $D(\bar{x})$ are defined as

$B(\bar{x})=\dfrac{(z+1)^2}{(z+1)^2+4\bar{x}^2}$, and $D(\bar{x})=\tan^{-1}\left(\dfrac{2\bar{x}}{z+1}\right)$, respectively, with $\bar{x}=q\bar{r}_c$. The coefficients c_i are given by,

$$c_1=\frac{1}{2}-\gamma(\cos y+y\sin y)+\frac{\gamma^2}{2}(1+y^2)$$

$$c_2=\gamma y(\gamma-\cos y)$$

$$c_3=\frac{\gamma^2+1}{2}-\gamma\cos y$$

$$c_4=\gamma^2(y\cos y-\sin y)^2-c_1 \qquad (5\text{-}53)$$

$$c_5=2\gamma\sin y[1-\gamma(y\sin y+\cos y)]+c_2$$

$$c_6=c_3-\gamma^2\sin^2 y$$

$$c_7=\gamma\sin y-\frac{\gamma^2}{2}(1+y^2)\sin 2y-c_5$$

$$c_8=c_4-\frac{1}{2}+\gamma\cos y-\frac{\gamma^2}{2}(1+y^2)\cos 2y$$

$$c_9=\gamma\sin y(1-\gamma\cos y)$$

in which $y=q\Delta$.

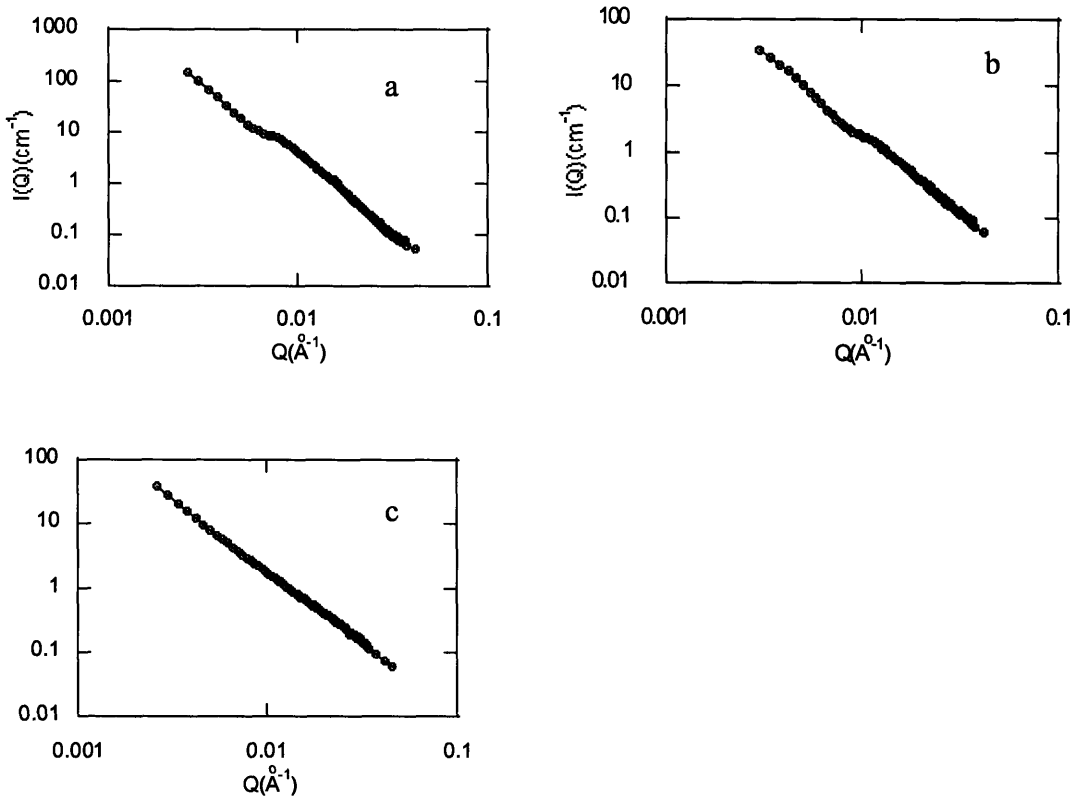

Figure 5-17 The model fitting of SANS intensities in trans samples. The open symbols represent the experimental data. The solid lines represent the fitting curves. (a). $C_4AzoOC_4E_2$, 0.7 mM. (b) $C_4AzoC_4E_2$, 1.2 mM. (c) $C_4AzoOC_6E_2$, 0.6 mM.

The highest sample concentration used was of the order of 1 mM, at which the interactions between micelles were negligible as indicated by the fact that no correlation peak was found in either SANS spectrum. As a result, the structure factor was assumed to be unity for all trans samples. Thus, the theoretical scattering intensity was taken to be

$$\frac{d\Sigma_{coh}}{d\Omega}(Q) = n\overline{P}(Qr_c) \tag{5-54}$$

where $\overline{P}(Qr_c)$ is given by (5-45) and (5-46).

The SANS spectra in trans samples were fitted by equation (5-54) combined with (5-52) and (5-53). In the fitting, the core SLD ρ_c was set equal to ρ_m. The fitted curves and

measured SANS spectra are shown in Figure 5-17. The fitted parameters are summarized in Table 5-1.

As shown in Table 5-1, trans photoresponsive surfactants form vesicle-like aggregates. The molecular lengths of the trans forms of both $C_4AzoOC_4E_2$ and $C_4AzoOC_6E_2$ are about 2.8 ~ 2.9 nm, from which we can infer that $C_4AzoOC_4E_2$ forms vesicles with shells consisting of four layers, while $C_4AzoOC_6E_2$ forms normal bilayer vesicles, as shown in Figure 5-18.

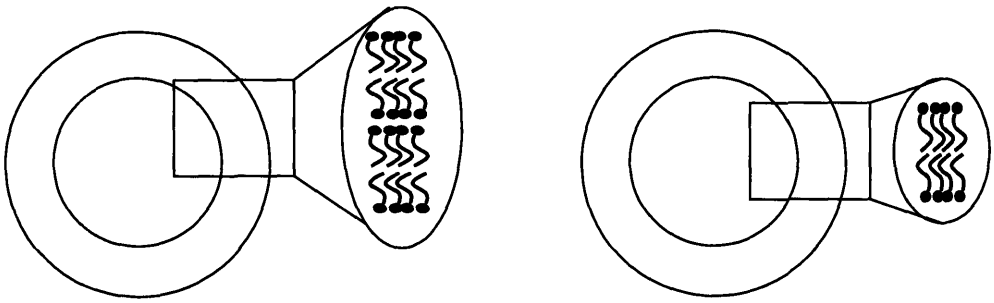

(a) (b)

Figure 5-18 Schematic self-assembly structures in trans $C_4AzoOC_4E_2$ (a) and $C_4AzoOC_6E_2$ (b).

In contrast, the SANS spectra for the cis isomer could not be described by the core-shell model. Rather, these spectra were fitted well by the Debye-Anderson-Bromberg (DAB) model[8], which characterizes the scattering density function in random

Table 5-1 Fitting parameters in trans samples

Surfactant	$C_4AzoOC_4E_2$		$C_4AzoOC_6E_2$
Concentration (mM)	0.7	1.2	0.6
Average vesicular radius (nm)	38.41	43.5	28.08
Shell thickness (nm)	11.24	12.5	5.85
Polydispersity	0.43	0.37	0.74

two phase systems, in which two phases with different SLDs randomly penetrate each other and spread over the whole sample. In the DAB model, the scattering intensity, which is proportional to the density-density correlation, is given by[8],

$$I(Q) = \frac{A}{(1+(Qa)^2)^2} \tag{5-55}$$

where a is the correlation length, and the scale factor A is given by[8],

$$A = 8\pi a^3(\rho_1 - \rho_2)^2\phi_1\phi_2 \tag{5-56}$$

in which ρ_1 and ρ_2 are the SLDs of phase 1 and 2, respectively, and ϕ_1 and ϕ_2 are the respective phase volumes.

All the cis samples could be fit simultaneously by the DAB model with the same A and a parameters, after appropriate normalization of the scattering intensity, in which the scattering intensity was divided by the concentration of self-assembled surfactant *C-CMC* (*C* is the surfactant concentration in the sample, *CMC* is the critical micellar concentration). One typical fitting result is shown in Figure 5-19.

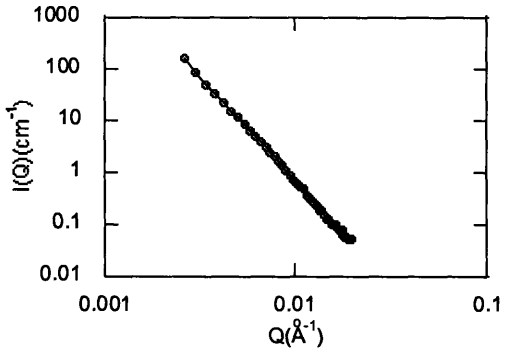

Figure 5-19 Fitting of SANS spectrum in cis $C_4AzoOC4E_2$ 0.7 mM. The open symbols represent the experimental data. The solid line represents the fitting curve. After normalization with surfactant concentration, SANS spectra of all cis samples collapse into a single one. Here, only the spectrum of the 0.7 mM solution is shown as a example, as all others are essentially the same

These results are consistent with those of some surfactant solutions that are known to exhibit random two phase structures under certain conditions, particularly, aqueous solutions of nonionic surfactants, in which the bicontinuous phases show the features of random two phase system. In bicontinous phases, surfactants self assemble into a single large bilayer, or multiple layers, that extend over the whole system, and separate the water phase into two disconnected parts, each of which also extends over the sample. Such surfactant layers are the solely visible objects in neutron scattering, are randomly oriented and positioned in space, and possess all the characteristics of a random geometry. This randomness in the surfactant layer has been captured well by the Debye-Anderson-Bromberg.

Based on this analysis, we can tentatively conclude that cis photoresponsive surfactants form bicontinuous phases under the experimental conditions considered here

5.4 Cryo-TEM Study on Self-assembly in Photoresponsive Surfactant Systems

Although SANS has several outstanding features for probing the structure of surfactant aggregates at the microscopic level, such as a large transfer momenta and contrast variation capabilities, it has one inherent shortcoming that prevents determinations of micro structure to be made unambiguously, common to all scattering technologies, the so-called "phase problem". In the scattering experiment, only intensity information is recorded, and the phase information is lost. As a consequence, the structure cannot be determined uniquely solely from scattering experiments, and complementary information is needed from other experiments. In this research, additional information was provided by directly visualizing the aggregates through cryo-TEM techniques.

5.4.1 Sample Preparation

In this study, two types of cryo-TEM techniques were utilized to visualize surfactant aggregates, replica and vitrified cryo-TEM, respectively. Trans samples were

prepared under ambient light, while cis samples were first illuminated for 1 hour under UV light, and then prepared in the dark.

The replica cryo-TEM samples were prepared through the QFDE (quick freeze-deep etch) method. First, a 1.5 μL drop of surfactant solution was deposited on the top of a metal plate, and the drop was then frozen by inserting the metal plate rapidly into propane quickly, which was cooled to about −186 °C by liquid nitrogen. Second, the frozen drop was transferred quickly to a sealed chamber, where it was evaporated for 5 minutes under a vacuum of 10^{-7} torr. In the third step, the frozen drop was coated first by a thin platinum film of thickness 2 ~ 3 nm; and then by a 20-30 nm carbon film. Finally, the frozen drop was removed from the chamber and kept at room temperature for a few minutes. After the ice had melted, the metal plate was plunged into water and the replica film floated to the water surface. The film was then placed on the grid and readied for TEM observation. The prepared samples were examined using a Philips EM410 Electron Microscope at the Whitehead Institute.

The vitrified cryo-TEM samples were prepared in a controlled environment vitrification system (CEVS). Thin films of samples were formed by placing a 3-5 μL drop of the liquid on a holey polymer support film which had been coated with carbon and mounted on the surface of a standard TEM grid or a bare 400 mesh copper grid. The drop was then carefully blotted with filter paper until a liquid layer of approximately 50-500 nm in thickness remained across the holes in the support film. About 3-4 sec after the liquid film was formed (to allow the system to relax after any shear introduced by the blotting process), it was vitrified by rapidly plunging the holey grid through a synchronous shutter at the bottom of the chamber into liquid ethane (cooled by liquid nitrogen) at its freezing point. The vitrified specimens were mounted on a cryotransfer stage (Oxford Instruments CT3500J) and examined at 100 kV in the conventional TEM mode of an analytical electron microscope (JOEL 1200EX) equipped with a twin-blade anticontaminator. The specimen temperature was maintained below -165 °C during imaging. The cryo-TEM experiments were performed by Paul Johnson of the University of Rhode Island.

5.4.2 Results

Typical TEM images for the trans and cis surfactant solutions are shown in Figure 5-20.

In the trans $C_4AzoOC_6E_2$ 0.6 mM sample, many spherical objects with sizes ranging from 50 ~ 70 nm were observed in the replica cryo-TEM picture (Figure 5-20 (a)), indicating that these surfactants self-assembled into spherical aggregates. Furthermore, in the vitrified cryo-TEM picture of the same system (Figure 5-20 (b)), vesicle-like structures were clearly evident. However, because of the limited resolution, it

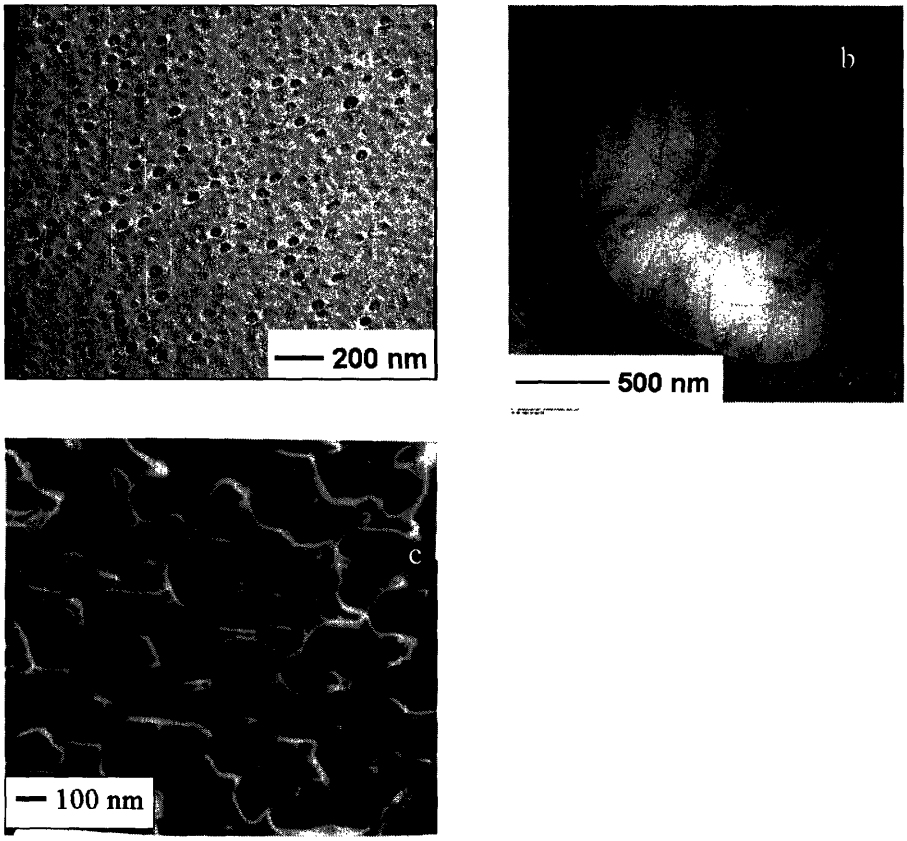

Figure 5-20 Cryo-TEM images of photoresponsive surfactant aggregates. (a) Replica, trans $C_4AzoOC_6E_2$ 0.6 mM. (b) Vitrified, trans $C_4AzoOC_6E_2$ 0.6 mM (c) Replica, cis $C_4AzoOC_6E_2$ 0.6 mM

is hard to estimate exact vesicle thickness from the TEM picture. But it is very likely bilayer as seen from Figure 5-20 (b). The cryo-TEM images proved that trans

$C_4AzoOC_6E_2$ self-assembled into vesicles. This conclusion was consistent with the results of the SANS analysis.

In the cryo-TEM picture of the cis $C_4AzoOC_6E_2$ solution structure (Figure 5-20 (c)), there appeared to be many domains of random shape and various sizes. Each domain was enclosed by a wall consisting of surfactants. This structure was consistent with that of the bicontinous phase. Moreover, the average domain size was found to be around 200 nm, which was close to the correlation length extracted from the SANS spectra.

Clearly, in both cases (trans and cis) the cryo-TEM results are consistent with the results from the SANS analysis and support the conclusion that the trans and cis forms of these surfactants have distinctly different aggregate morphologies.

5.5 Theoretical Analysis on Self-Assembly in Photoresponsive Surfactant System

From the SANS and cryo-TEM studies, it was found that trans form of photoresponsive surfactants self-assemble into vesicles, while their cis form shows the characteristics of bicontinuous phases. In this section, we will attempt to explain this interesting structural transition theoretically. In the first part, we introduce the elastic theory of surfactant films, and enunciate the various surfactant phases predicted by it. Next, a microscopic theory to calculate bending rigidity from molecular parameters is introduced. From this theory, we can estimate the sign of the bending and Gaussian rigidities in both the trans and cis isomers by simple geometrical considerations. Through combining conclusions from these two theories, we arrive at an explanation of the observed structural transition.

5.5.1 Elastic Theory of Surfactant Membrane

The behavior of surfactant membranes can be described well by simple elastic theory [11]. The idea is that, in most surfactant membrane systems, the surface tension is almost zero, and hence, the bending is the dominant property controlling the behavior of

membranes. According to the elastic theory, the free energy density of a monolayer can be described simply by[11],

$$f = \frac{1}{2}\kappa_m(\sigma_1 + \sigma_2 - \sigma_0)^2 + \overline{\kappa_m}\sigma_1\sigma_2 \tag{5-57}$$

in which κ_m and $\overline{\kappa_m}$ are the bending and Gaussian rigidities, respectively; σ_1 and σ_2 are the two principle curvatures; and σ_0, the spontaneous curvature of the monolayer, is a function of the chemical composition and molecular architecture of its constituent surfactants.

In a bilayer, both the bending and the Gaussian rigidities can be calculated from those of the monolayer[11],

$$\begin{aligned} \kappa &= 2\kappa_m \\ \overline{\kappa} &= 2(\overline{\kappa_m} - \delta\sigma_0\kappa_m) \end{aligned} \tag{5-58}$$

in which δ is the thickness of the bilayer. Because the chemical composition is the same in each monolayer, the bilayer spontaneous curvature is essentially zero, and thus the free energy density for the bilayer is represented by

$$f = \frac{1}{2}\kappa(\sigma_1 + \sigma_2)^2 + \overline{\kappa}\sigma_1\sigma_2 \tag{5-59}$$

From this free energy, we can calculate the phase diagram of a surfactant solution in terms of κ and $\overline{\kappa}$, as done below.

Equation (5-57) can be rewritten in the more convenient form[12],

$$f = \frac{1}{2}[(\kappa + \frac{1}{2}\overline{\kappa})(\sigma_1 + \sigma_2)^2 - \frac{1}{2}\overline{\kappa}(\sigma_1 - \sigma_2)^2] \tag{5-60}$$

For $\kappa + \overline{\kappa}/2 > 0$ and $\overline{\kappa} < 0$, the equilibrium state is the lamellar phase in which both $\sigma_1+\sigma_2$ and $\sigma_1-\sigma_2$ are zero. If $\kappa + \overline{\kappa}/2 < 0$ and $\overline{\kappa} < 0$, the free energy decreases without limit for $|\sigma_1+\sigma_2|$ large and $|\sigma_1 - \sigma_2|$ zero. Above the CMC, the largest attainable

curvature in spherical micellar surfactant aggregates is *1/R* where *R* is the radius of the spherical micelles with the order of surfactant length. Therefore, it is concluded that the spherical micellar phase is the stable phase under these conditions. Similarly, if $\kappa + \bar{\kappa}/2 > 0$ and $\bar{\kappa} > 0$, the free energy decreases without limit for $\sigma_1 + \sigma_2 = 0$ and $|\sigma_1 - \sigma_2|$ large. This corresponds to a minimal surface, in which the average curvature $(\sigma_1 + \sigma_2)/2$ is zero everywhere. In reality, there is always some repulsive interaction originating from either steric interactions or entropy, stabilizing the system at some finite σ. Under such circumstances, the equilibrium system is the bicontinous phase. Finally, for $\kappa + \bar{\kappa}/2 < 0$ and $\bar{\kappa} > 0$, the bending rigidity κ is negative, which makes no sense for any real physical system. The above results are summarized in the surfactant solution phase diagram shown in Figure 5-21.

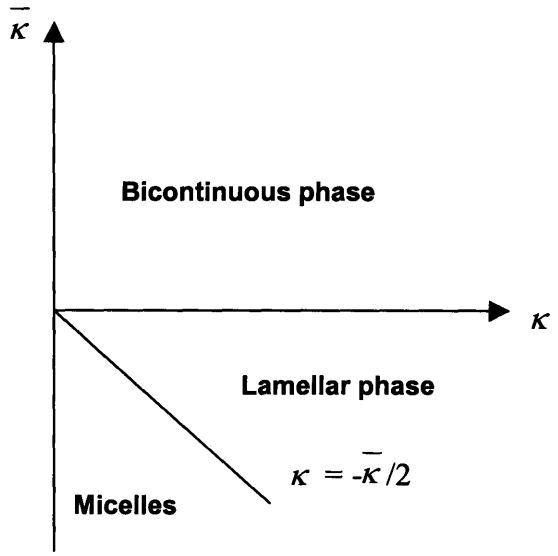

Figure 5-21 The phase diagram of surfactant solutions from the Helfrich elastic theory. $\bar{\kappa}$ is the Gaussian rigidity and κ is the bending rigidity.

The region of this phase diagram most relevant to the self-assembly behavior of our photoresponsive surfactant is the transition from a lamellar to a bicontinous phase, that is, where the Gaussian rigidity changes sign from negative to positive, and there is transition from a lamellar to a bicontinous phase. If the Gaussian rigidity of the cis isomer is positive while that of the trans is negative, then our experimental results can be explained

in terms of elasticity theory. However, in order to apply the elasticity theory, we must estimate the sign of the Gaussian rigidity from the surfactant architecture; this is the task of the next subsection.

5.5.2 Petrov-Derzhanski-Mitov Model

The Petrov-Derzhanski-Mitov (PDM) model is a microscopic model relating the bending and Gaussian rigidities to the surfactant molecular parameters[13]. According to the PDM model, the free energy per molecule in a monolayer is[13]

$$f_m = \frac{k_H}{2}\left(\frac{A_H}{H}-1\right)^2 + \frac{k_C}{2}\left(\frac{A_C}{C}-1\right)^2 \tag{5-61}$$

in which k_H and k_C are the elastic constants of the interaction between heads and between tails, respectively. A_H and A_C are the cross sectional areas of respective head and tail groups, while H and C are the corresponding cross sectional areas in the absence of interactions. The cross sectional areas of the head and tail groups can be calculated from the curvature and monolayer thickness, $\delta/2$[13]:

$$A_H = A[1+\delta_H(\sigma_1+\sigma_2)+\delta_H^2\sigma_1\sigma_2] \tag{5-62}$$

$$A_C = A[1+\delta_C(\sigma_1+\sigma_2)+\delta_C^2\sigma_1\sigma_2]$$

where A is the mean area per molecule measured at the neutral plane, in which the surfactants do not experience any strain; δ_H and δ_C is the distance from neutral surface to head and tail group, respectively.

Substituting equation (5-62) into (5-61), both bending and Gaussian rigidity can be obtained by comparing with corresponding coefficients in equation (5-63),

$$\kappa = \left(\frac{k_H}{H^2}\delta_H^2 + \frac{k_C}{C^2}\delta_C^2\right)A_0 \tag{5-63}$$

and

$$\bar{\kappa} = \frac{k_H k_C}{H^2 C^2} \frac{H - C}{\frac{k_H}{H^2} + \frac{k_C}{C^2}} (\delta_C^2 - \delta_H^2) \tag{5-64}$$

where $A_0 = \frac{k_H H^{-1} + k_C C^{-1}}{k_H H^{-2} + k_C C^{-2}}$ is the equilibrium area of planar monolayer.

In the symmetrical bilayer, in which the chemical ingredients in two monolayers are identical, the neutral surface locates exactly between two monolayers. Under such circumstance, the distance from neutral surface to head and tail group δ_H and δ_C, respectively, can be expressed by

$$\delta_H = \frac{d}{2} \quad \text{and} \quad \delta_C = \frac{d}{2} - \delta \tag{5-65}$$

in which d is the bilayer thickness; δ is the relative distance between the head and the tail of surfactant.

Substituting equation (5-65) into (5-63) and (5-64), the bending and Gaussian rigidities can be represented by

$$\kappa = \frac{d^2}{2} \left(\frac{k_H}{H^2} + \frac{k_C}{C^2} (1 - \frac{2\delta}{d})^2 \right) \frac{\frac{k_H}{H} + \frac{k_C}{C}}{\frac{k_H}{H^2} + \frac{k_C}{C^2}} \tag{5-66}$$

and

$$\bar{\kappa} = -2\delta(d - \delta) \frac{k_H k_C}{H^2 C^2} \frac{H - C}{\frac{k_H}{H^2} + \frac{k_C}{C^2}} \tag{5-67}$$

respectively. Therefore, the bending and Gaussian rigidities are functions of surfactant molecular architecture, which is characterized by the cross sectional areas of the head (H) and tail (C) groups in the PDM model. The bending rigidity κ is always positive, consistent with the stability requirement for the bilayer system. However, the Gaussian rigidity $\bar{\kappa}$ can change sign with changes in surfactant shape. More specifically, for a surfactant whose head cross sectional area is larger than that of the tail, $\bar{\kappa}$ is negative. In contrast, for surfactants with a larger tail group, $H < C$, $\bar{\kappa}$ is positive. When the phase diagram in Figure 5-20 is taken into account, it can be concluded that, when $H > C$, surfactants self- assemble into a lamellar or, equivalently, a vesicle phase; while for $H < C$, surfactants form a bicontinuous phase.

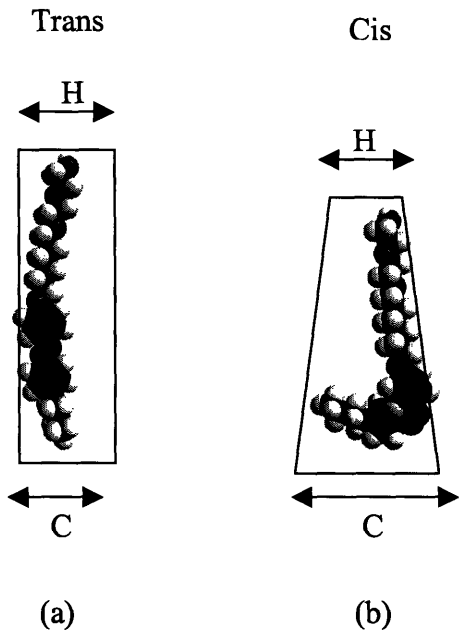

Figure 5-22 The molecular architecture of $C_4AzoOC_6E_2$ in the trans (a) and cis (b) forms. The equilibrium molecular architectures were computed by Gauss 94 with 3-21 basis set. In order to stress the structural characteristics, each molecule has been highlighted by a frame of similar shape.

The particular advantage of the PDM model is that we can predict the sign of the Gaussian rigidity, and therefore predict the surfactant phase behavior using only simple geometrical arguments based on surfactant architecture. As shown in Figure 5-22, in the

trans form, the cross sectional area of the head, *H,* is similar to that of the tail, *C*; while in the cis form, the head group area is significant less than that of the tail group. Therefore, according to the above analysis, the trans surfactants prefer to form lamellar or vesicle phases, while cis surfactants self-assemble into bicontinuous phases. This conclusion is consistent with results from the cryo-TEM and SANS studies.

5.6 Summary

In this chapter, we presented a detailed study of the self-assembly properties of photoresponsive surfactants in bulk solution under different illumination conditions. The structure of the self-assembled aggregates was probed by static and dynamic light scattering, SANS, and cryo-TEM.

The self-assembly of trans $C_4AzoOC_6E_2$ was investigated by light scattering over the low concentration range (0.0015 to 0.17 mM). $C_4AzoOC_6E_2$ exhibited a strong tendency for "micellar growth", such that even at concentrations just above the CMC, it formed cylindrical micelles. With increases in concentration, the cylindrical micelles became longer, and appeared to form worm-like chains or micelles. The worm-like micelle can be considered as consisting of a chain of rigid rods of a given persistence length. The spatial distribution of these rigid rods can be characterized by the fractal dimension of the aggregates. From scattering intensities vs Q curves in static light scattering, the persistence length can be extracted using the high Q-range data, while the fractal dimension can be estimated from low-Q results. It was found that, over concentrations studied, persistence lengths were almost constant, while fractal dimensions increased with concentration, and finally reached the maximum value of 2, which corresponds to the fractal dimension of a Gaussian coil. With increased concentrations, the cylindrical micelles became longer and longer, and finally acquired sufficient flexibility to form Gaussian coils; the persistence length did not chane under increasing concentration. When concentration increased further, branched Gaussian coils were formed.

The self-assembled bulk solution structures of $C_4AzoOC_6E_2$ and $C_4AzoOC_4E_2$ at high concentrations were investigated by SANS under both UV and visible light

illumination. It was found that the trans surfactants self-assembled into vesicles with either a bilayer ($C_4AzoOC_6E_2$) or a quadri-layer ($C_4AzoOC_4E_2$) structure. In contrast, the cis surfactants formed bicontinuous phases. The SANS results were verified by Cryo-TEM studies, in which the surfactant aggregates can be visualized directly with little disturbance to the system.

Combining the Helfrich elasticity theory with the Petrov-Derzhanski-Mitov (PDM) model validated the transition from vesicle to bicontinuous phase after UV illumination. According to these theories, because of the differences in molecular architecture between the trans and cis isomers, the trans surfactant possesses negative Gaussian rigidity, while the cis form possesses positive Gaussian rigidity. As a consequence, trans surfactants tend to self-assemble into vesicles while cis surfactants form a bicontinuous phase. Thus, experimental results can be explained well by theory.

5.7 Bibliography

1. Hiemenz, P. C. & Rajagopalan, R. *Principles of Colloid and Surface Chemistry* (Marcel Dekker, Inc., New York, 1997).

2. Shang, T. G., Smith, K. A. & Hatton, T. A. Photoresponsive Surfactants Exhibiting Unusually Large, Reversible Surface Tension Changes under Varying Illumination Conditions. *Langmuir* **19**, 10764-10773 (2003).

3. Chen, S. H. & Kotlarchyk, M. *Interaction of Photons and Neutrons with Matter: An Introduction* (World Scientific, Singapore, 1997).

4. Schmitz, K. S. *An Introduction to Dynamic Light Scattering by Macromolecules* (Academic Press, Boston, 1990).

5. Higgins, J. S. & Benoît, H. C. *Polymers and Neutron Scattering / and* (Clarendon Press, Oxford, 1994).

6. Puvvada, S. & Blankschtein, D. Thermodynamics Description of Micellization, Phase-behavior, and Phase-Separation of Aqueous-Solution of Surfactant Mixtures. *J.Phys.Chem.* **96**, 5567-5579 (1992).

7. Steed, J. W. & Atwood, J. L. *Supramolecular Chemistry* (Wiley, New York:, 2000).

8. Roe, R. J. *Methods of X-ray and Neutron Scattering in Polymer Science* (Oxford University Press, New York, 2000).

9. Bartlett, P. & Ottewill, R. H. A Neutron Scattering Study of the Structure of a Bimodal Colloidal Crystal. *J. Chem. Phys.* **96**, 3306-3318 (1992).

10. Hayter, J. B. in *Physics of Amphiphiles: Micelles, Vesicles, and Microemulsions* (eds. Degiorgio, V. & Corti, M.) (North-Holland, Amsterdam, 1985).

11. Helfrich, W. Elastic properties of Lipid Bilayers - Theory and Possible Experiments. *Z. Naturforsch C* **28**, 693-703 (1973).

12. Kleman, M. & Lavrentovich, O. D. *Soft Matter Physics: An Introduction* (Springer-Verlag, New York, 2003).

13. Petrov, A. G. *The Lyotropic State of Matter : Molecular Physics and Living Matter Physics* (Gordon and Breach Science Publishers, Amsterdam, The Netherlands, 1999).

Chapter 6

Conclusions

6.1 Summary of Research

We have developed and synthesized a new class of nonionic photoresponsive surfactants incorporating the photoresponsive azobenzene group in the tail, which can switch between the trans and the cis conformations in response to different radiation conditions. In this way, the molecular conformation of these photoresponsive surfactants can be controlled by light. The distinct structural feature of our surfactants is the insertion of a middle polar group in the tail, which is connected to the head group by an alkyl chain termed the spacer. In this research, four photoresponsive surfactants with different spacer lengths (2, 4, 6, and 8 methylene groups), were synthesized. Their properties, such as equilibrium surface tension, self–assembly in solution, and the structure of adsorption layer at the air-water interface, have been investigated under both UV and visible illumination.

It was found experimentally that these new photoresponsive surfactants demonstrate many interesting properties. As revealed by experimental and theoretical analyses, these properties originated from three key structural units—the azobenzene group, the spacer, and the middle polar group. The highly orientational π- π interactions between azobenzene groups are strongest when two azobenzene groups are in parallel, and weakest when they are perpendicular to each other. These interactions, which also depend on whether the azobenzene group is in the trans or cis conformation, affect the interfacial and bulk solution properties significantly. The middle polar group, an ether oxygen, can form hydrogen bonds with water molecules, and makes the tail somewhat hydrophilic. The spacer, which connects the middle polar group and the ethylene oxide groups, provides the necessary flexibility for an "adaptive conformational change" in the surfactant (The term "adaptive conformational change" introduced here is to distinguish from the trans-cis conformation change in azobenzene, which was induced by the external radiation and termed the "externally induced conformational change".). In the

adaptive conformation change, surfactants adopt the new conformation spontaneously in response to variations in molecular architecture and surrounding environments.

In the adsorbed layer, these three structural features manifest themselves by the formation of a "loop conformation". It was found from simple surface tension measurements and more elaborate neutron reflection analysis that there new photoresponsive surfactants can take on a loop conformation in which the spacer between the polar head and the middle polar group forms a loop anchored at both ends in the interfacial plane, or lies within the interface. The loop conformation is actually the result of complex interactions between the head and tail groups, both with each other and with the water sub-phase. The adoption of a loop conformation depends strongly on the length of the spacer. The C_2 spacer and the ether oxygen combined constitute a third ethylene oxide moiety, forming a large polar E_3 head group (as opposed to the E_2 head group of the other surfactants) and thus this surfactant has the more conventional structure of a single polar head group attached to a hydrophobic tail moiety, and both the trans and cis conformations extend away from the interface and have similar surface excess concentrations. The surface areas per molecule of about 21 $Å^2$ for the two forms of this surfactant show that both conformations are tightly packed within the interface. The C_4 and C_6 spacers, in contrast, are sufficiently long that they are capable of forming loops if energy considerations favor this configuration. The trans surfactant appears to adopt an orientation normal to the interface, however, probably stabilized by π-π interactions. This assertion is supported by the observation that the trans forms of the $C_4AzoOC_4E_2$ and $C_4AzoOC_6E_2$ surfactants have surface excess concentrations and surface areas per molecule similar to those of the $C4AzoOC_2E_2$ surfactants. Moreover, the interaction enthalpies for these cases are high, indicating that such interactions must be occurring between the surfactants within the adsorbed layer. As the spacer length increases, the interactions are reduced owing to a greater degree of configurational freedom with longer alkyl chains. The reduction in the stabilizing π-π interactions when the azobenzene group adopts the cis conformation, on the other hand, coupled with its strong dipole moment, favors a configuration where the azobenzene group is partially in the interfacial plane. The areas occupied per molecule for these surfactants in the cis state (~36 $Å^2$) are higher

by about 15 $Å^2$ than those for the $C_4AzoOC_2E_2$ surfactant, a difference that is consistent with the molecular models of the surfactants. This loss of interactions owing to looser packing of molecules in the interface is reflected in the lack of interaction enthalpies for these surfactants in these configurations. Under such circumstances, the cis form of $C_4AzoOC_4E_2$ and $C_4AzoOC_6E_2$ take the loop conformation at the interface, and have the larger molecular area and the higher surface tension than their trans form. Based on the above analysis, we can say that, in surfactant $C_4AzoOC_4E_2$ and $C_4AzoOC_6E_2$, an adaptive conformation change — from vertical to loop conformation, is induced by the trans –to-cis azobenzene conformation change. Finally, for the $C_4AzoOC_8E_2$ surfactant, the spacer is sufficiently long that it can adopt a loop configuration with a greater number of degrees of freedom, relieving some of the entropic penalty associated with the anchoring of both ends of the spacer at the interface and avoiding unfavorable hydrophobic interactions between the spacer methylene groups and water, even as it allows for the azobenzene group to lie within the interfacial zone. Under these circumstances, even the trans form of the azobenzene group may be favored thermodynamically to lie in the interface. Consequently, the area occupied by the trans form of the surfactant would be expected to be larger than that of the cis form, as indeed it is.

The interfacial conformation of the surfactant completely determines its saturated surface tension. In $C_4AzoC_2E_2$, both its trans and cis forms adopt the vertical conformation, therefore, $C_4AzoC_2E_2$ shows similar molecular areas and saturated surface tensions before and after UV illumination. In $C_4AzoC_4E_2$ and $C_4AzoC_6E_2$, their trans isomers take the vertical conformation while their cis forms adopt the loop conformation at the interface. As a consequence, the saturated surface tensions of trans isomers are significantly higher than those of the cis. On the contrary, in $C_4AzoC_8E_2$, because of its long spacer, both of its trans and cis forms take the loop conformation. The rigid azobenzene group makes the molecular area of the linear trans form much larger than that of the bent cis form, and consequently the saturated surface tension for the trans form was even higher than for the cis, which is consistent with the experimentally observed trends.

The azobenzene group and related π–π interactions seem to exert significant effects on the self-assembly behavior of these photoresponsive surfactants. The

orientation dependent π–π interaction makes these surfactants favorably self-assemble into low curvature aggregates such as cylinders and discs, because in these low curvature aggregates, the azobenzene group can be packed in the more parallel fashion and lower the overall free energy through strongly attractive interactions. Therefore, free energies of different packing geometries are quite different. As a consequence, the growth factor α, which quantitatively characterizes the free energy gap between different packing geometries, is very large. A large growth factor α implies strong surfactant growth, and was actually observed in our photoresponsive surfactants. From light scattering analysis, it was found that these photoresponsive surfactants self-assembled into cylindrical micelles even at concentrations just above the CMC, and their size increased significantly with concentration. At intermediate concentrations, with long but finite contour length, these cylindrical micelles behaved as worm-like chains with persistence length of 26 nm (trans form of $C_4AzoOC_6E_2$). Finally, at a sufficiently high concentration, the contour length of these cylindrical micelles was so long that they acquired considerable flexibility. Under such circumstances, worm–like chains fold into random coils. With further increases in concentration, the cylindrical micelle begins to transform to the disc micelle, because the bilayer packing is more favorable energetically. At sufficient high concentrations, the disk micelle can close up to form a spherical vesicle in order to decrease its high energy rim. As revealed by SANS, vesicle-like structures were indeed found in $C_4AzoOC_6E_2$ solutions at concentrations larger than 0.6 mM. The observed self-assembly sequence in $C_4AzoOC_6E_2$ was consistent with the large growth factor α, which originates from the π–π interaction between azobenzene groups.

The most distinguishing feature in these photoresponsive surfactants is perhaps that their self-assembly structures can vary significantly in response to different illumination conditions. As revealed by both SANS and cryo-TEM studies, trans $C_4AzoOC_6E_2$ self-assembled into vesicles at high concentration, while its cis isomer forms a bicontinuous phase. This variation in phase behavior actually implies a sign change in Gaussian rigidity, because surfactants with positive Gaussian rigidity prefer the bicontinuous phase, while surfactants with negative Gaussian rigidity tend to self-assemble into vesicles. According to the PDM model, the Gaussian rigidity is completely

determined by the surfactant molecular architecture. For those surfactants whose head group area is larger than that of the tail, such as the trans isomer, the Gaussian rigidity is negative, while for surfactants with larger tail group areas, such as the cis form, the Gaussian rigidity is positive. This theoretical model provides a physical interpretation of the observed experimental phenomena well. Using these photoresponsive surfactants, by simply illuminating the sample with radiation of different wavelengths, we can control their Gaussain rigidity, and consequently their phase behavior at will.

In summary, because of the nontrivial structure of these new photoresponsive surfactants, they demonstrate many special properties. Under certain conditions, they can form the loop conformation at the interface, and induce large changes in surface tension under different illumination conditions. These surfactants possess large growth factors, and undergo micellar growth processes. Under different illumination conditions, in response to the trans-to-cis conformation change, the Gaussain rigidity changes sign, and as a result, the surfactant phase can switch from the vesicular phase (trans) to the bicontinous phase (cis).

6.2 Future Directions

As stressed above, the special properties of this new class of photoresponsive surfactants originate from their particular structural features. In the future, it may highly desirable to develop other photoresponsive surfactants that exhibit excellent performance in both interfacial and bulk properties.

One of the possible directions is to replace the basic structural units in our photoresponsive surfactants with different chemical constituents. The middle polar group ether oxygen can be replaced with an amine group, for instance, which also forms hydrogen bonds with water molecules, and is expected to behave similar to the ether oxygen. Similarly, the length of the spacer can be changed to assess its role in determining interfacial conformation more closely. Finally, the azobenzene group can be replaced by other light active groups, such as spiropyrans. Indeed, there are many ways to manipulate the chemical make-up within each structural unit and to make various combinations to produce surfactants with different physical and chemical properties.

Secondly, because of the wavelength limitation of the Argon-ion laser used in our light scattering apparatus, the self-assembly behavior of the trans isomer only was studied. However, with a HeNe laser (whose wavelength is about 540 nm), it should be possible to probe the self assembly behavior of cis isomers, which are expected to behave differently owing to their different molecular architecture.

Thirdly, the more detailed self-assembly structure of trans and cis isomers can be acquired by SANS through selective deuteration. By selective deuteration, different moieties such as azobenzene and spacer can be highlighted. Their distributions in self-assembly aggregates can be measured individually, and their roles in self-assembly can be determined ambiguously. Therefore, the comprehensive structural information on surfactant aggregates can be acquired. It is suggested that we use deuterated surfactants in SANS structural studies.

Finally, the dynamic surface tension is another issue. In many practical applications, the surface tension may need to be controlled rapidly. Therefore, an understanding of the surface tension dynamics becomes necessary in the design of reliable and quick-response systems. From our previous measurements of surface tensions, it was found that surface tension changes very slowly at concentrations close to the CMC (characteristic time $\approx$ 72000 second), and we attribute these slow dynamics to the extremely low concentration in the system ($\sim$ 1 μM). The effect of both concentration and temperature on dynamic surface tension needs to be studied, as well as the dynamic response of the surface tension when switching between different illumination conditions.